1506
UNIVERSITÀ
DEGLI STUDI
DI URBINO
CARLO BO

UNIVERSITÀ DEGLI STUDI DI URBINO CARLO BO

Dipartimento di Scienze Pure e Applicate
Corso di Dottorato in Scienze di Base e Applicazioni
Curriculum di Scienza della Complessità
XXXII CICLO

Tesi di Dottorato

GALACTIC COSMIC-RAY RECURRENT AND TRANSIENT SHORT-TERM VARIATIONS: ADVANCED DATA ANALYSIS AND MODELING

Relatore:
Prof.ssa Catia Grimani

Candidato:
Simone Benella

Correlatori:
Dott.ssa Monica Laurenza
Prof. Giuseppe Consolini

Settore Scientifico Disciplinare: FIS/01

Anno Accademico 2018 - 2019

Alla mia famiglia.

Publications

Grimani, C., Telloni, D., **Benella, S.**, Cesarini, A., Fabi, M., & Villani, M. (2019). Study of Galactic Cosmic-Ray Flux Modulation by Interplanetary Plasma Structures for the Evaluation of Space Instrument Performance and Space Weather Science Investigations. Atmosphere, 10(12), 749.

Benella, S., Grimani, C., Fabi, M., Finetti, N., & Villani, M. (2019). Recurrent and non-recurrent galactic cosmic-ray flux short-term variations observed with LISA Pathfinder. In 36th International Cosmic Ray Conference (ICRC2019) (Vol. 36).

Benella, S., Grimani, C., Laurenza, M., & Consolini, G. (2019). Grad-Shafranov reconstruction of a magnetic cloud: Effects of the magnetic-field topology on the galactic cosmic-ray intensity. Nuovo Cimento C Geophysics Space Physics C, 42.

Grimani, C., Telloni, D., Villani, M., Finetti, N., Laurenza, M., **Benella, S.**, & Fabi, M. (2019). Galactic cosmic-ray flux short-term variations and associated interplanetary structures with LISA Pathfinder. Nuovo Cim., 42, 42.

Armano, M., Audley, H., Baird, J., **Benella, S.**, Binetruy, P., Born, M., ... & Cruise, A. M. (2019). Forbush decreases and < 2 day GCR flux non-recurrent variations studied with LISA pathfinder. The Astrophysical Journal, 874(2), 167.

Armano, M., Audley, H., Baird, J., Bassan, M., **Benella, S.**, Binetruy, P., ... & Cruise, A. M. (2018). Characteristics and energy dependence of recurrent galactic cosmic-ray flux depressions and of a forbush decrease with LISA Pathfinder. The Astrophysical Journal, 854(2), 113.

Benella, S., Consolini, G., Giannattasio, F., Chang, T., & Echim, M. (2017). Avalanching Systems with Longer Range Connectivity: Occurrence of a Crossover Phenomenon and Multifractal Finite Size Scaling. Entropy, 19(8), 383.

Grimani, C., **Benella, S.**, Fabi, M., Finetti, N., Telloni, D., & LISA Pathfinder Collaboration. (2017, May). GCR flux 9-day variations with LISA Pathfinder. In Journal of Physics: Conference Series (Vol. 840, No. 1, p. 012037). IOP Publishing.

Acknowledgments

I would like to express my gratitude to my supervisors Professor Catia Grimani and Dr. Monica Laurenza. They guided me, for the first time in my career, in the magic world of cosmic rays sharing with me their precious knowledge. I will never thank them enough for their availability and for all the opportunities that they gave me during my PhD course. I wish to acknowledge my third supervisor Professor Giuseppe Consolini that introduced me to the physics of complex systems being an inestimable guide during the years 2014-2020.

Special thanks go to Professor Rami Vainio and Dr. Alexandr Afanasiev of the Department of Physics and Astronomy of the University of Turku (Finland) for extensive discussions and valuable suggestions which greatly contributed to the improvement of this thesis work. They hosted me for a visiting period, supporting my work with enthusiasm and helping me to widen my research from various perspectives.

I would like to render my warmest thanks to Professor Qiang Hu at the Center for Space Plasma and Aeronomic Research at the University of Huntsville in Alabama (UAH, AL, USA) for his precious help and for having shared with me his knowledge and his computer codes. I thank him very much especially for his availability and kindness.

I would like to express my gratitude to the director of my PhD curriculum, Professor Vincenzo Fano for sharing with me his deep passion and knowledge on fundamental of physics. This thesis has been written during my stay at the Department of Pure and Applied Sciences at the University of Urbino and I would like to thank the directors of my PhD course, Professor Mauro Sergio Micheloni first and Professor Alessandro Bogliolo at present time, for providing excellent working conditions and financial support for my research traveling.

I would like to thank the National Institute for Nuclear Physics in Florence and the Institute for Spatial Astrophysics and Planetology in Rome for the financial support for traveling abroad to attend international conferences, summer schools and visiting periods.

I express my gratitude to Michele Fabi of the University of Urbino for technical support and for great time together, especially for the pizza time! I would like also to thank Dr. Mattia Villani of my research group and Dr. Andrea Cesarini for his precious work on the LISA Pathfinder platform magnetic field data and unforgettable moments spent together. I would like to thank all the people at the Institute for Spatial Astrophysics and Planetology in Rome, in particular my office mate Virgilio Quattrociocchi that shared with me two amazing summer schools and Tommaso Alberti for all the interesting and constructive discussions. I would like also to thank all the colleagues at UAH, where I spent two months, in particular Bishwas Shresta for being an excellent physicist and a great friend.

I would like to thank my "Chérie", Maria Chiara for being part of my life, for encouraging me and loving me everyday and, last but not least, I wish to express my gratitude to my family, my brother Luca, my mother Mara and my father Piero for their important support during my life and scientific career: I acknowledge to them the achievement of this objective.

Simone Benella

Contents

List of Figures

List of Tables

Acronyms

ACE Advanced Composition Explorer

BR Bartels rotation

CME Coronal mass ejection

CHSS Corotating high-speed stream

CIR Corotating interaction region

EMD Empirical mode decomposition

FD Forbush decrease

GCR Galactic cosmic rays

GS Grad-Shafranov

GSE Geocentric solar ecliptic

GSMF Global solar magnetic field

HCS Heliospheric current sheet

HHT Hilbert-Huang transform

HSA Hilbert spectral analysis

HT De Hoffmann-Teller

ICME Interplanetary coronal mass ejection

IMF Interplanetary Magnetic Field

ISS International space station

LIS Local interstellar

LPF LISA Pathfinder

MB Magnetic barrier

MC Magnetic Cloud

MFE Magnetic field enhancement

MHD Magnetohydrodynamics

MVAB Minimum variance analysis of the magnetic vector

NM Neutron monitor

PD Particle detector

PDF Probability distribution function

S/C Spacecraft

SEP Solar energetic particle

TM Test mass

TP Test particle

Introduction

Galactic Cosmic Rays (GCRs) were discovered by Victor Hess in 1912 (Hess, 1912) with aloft balloons carrying ionization chambers. Ground-based detectors (e.g. ionization chambers, Geiger counters, muon detectors and neutron monitors; NMs) were installed since then around the globe (see Stoker, 2009). Among them, NMs have played an important role for having provided more than 60 years of continuous observations on integrated GCR flux above cutoff rigidities of 0.1-10 GV (Smart and Shea, 2009). NMs, however, cannot measure the primary component of GCRs because these high-energy particles interact in the Earth atmosphere and produce secondary particles. Only during the 1960s, detectors placed on board spacecraft (S/C) allowed for direct observations down to tens of MeV energies. Nowadays, the term GCRs refers to cosmic rays that are thought to be originated within our Galaxy and even beyond. The GCR propagation process from the interstellar medium in the heliosphere towards Earth is described throughout this work and a sketch in provided by Figure 1. The Sun is an active star and emits a continuous radial flow of supersonic plasma (solar wind) carrying a magnetic field in the interplanetary space that remains rooted on the photosphere of the Sun. As the Sun rotates, the magnetic field forms an Archimedean spiral that fills the whole region in which the Sun manifests its influence: the heliosphere. Outside the heliosphere, the interstellar medium is populated by GCRs presenting a time-independent isotropic flux. The Voyager 1 and 2 S/C traversed the termination shock of the heliosphere at 94 AU (Stone et al., 2005) and 84 AU (Richardson et al., 2008), respectively, and Voyager 1 crossed the heliopause at 121 AU (Gurnett et al., 2013), allowing for the first direct measurements of GCRs beyond the region dominated by the solar wind (Stone et al., 2013). The overall effect of particle propagation through the heliosphere is known as solar modulation (Potgieter, 2013). The GCR modulation varies with the solar activity that presents a quasi-periodic 11-year cycle. A clear anti-correlation between the GCR

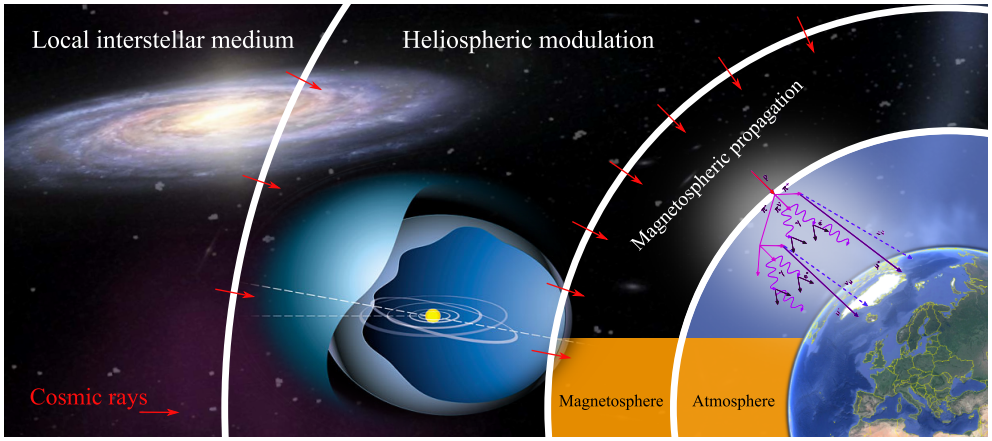

Figure 1 Sketch of the cosmic-ray propagation from the interstellar medium through heliosphere, magnetosphere and interaction with the Earth atmosphere.

intensity in the inner heliosphere and the solar activity is observed. A 22-year periodicity is also observed in the GCR flux trend due to the reversal of the solar magnetic field polarity (Hathaway, 2015). Solar activity and solar polarity induce long-term GCR flux variations (see Chapter 3).

Due to Sun rotation with a periodicity of about 27 days near the equator (synodic period), long-living structures in the upper layers of the Sun, e.g. coronal holes mainly during the descending part of the solar cycle, generate solar wind disturbances that cause quasi-periodic modulations of the GCR flux on shorter time scales (from hours to a month). These short-term GCR flux variations can be either recurrent or transients depending on the characteristics of solar wind disturbances that originate them.

This thesis work is devoted to the study of recurrent and transient GCR flux variations observed with a particle detector (PD) on board the European Space Agency (ESA) LISA Pathfinder (LPF) mission. The LPF S/C orbited around the L1 Lagrangian point between 2016 and 2017. ESA found as necessary to fly a pathfinder mission aiming to test the instrumentation that will be placed on board the first interferometer for low-frequency gravitational wave detection in space LISA (Laser Interferometer Space Antenna; Amaro-Seoane et al., 2017). In order to control any source of noise on the test masses that play the role of mirrors of the interferometer, diagnostics detectors were placed on board the LPF S/C for temperature, incident radiation and magnetic field monitoring. Incident radiation observations, in particular, were carried out with a PD

consisting of two silicon wafers placed in a telescopic arrangement with a geometrical factor of 18 cm^2 sr for particle single-count measurements. Proton and helium nuclei (constituting roughly 98% of the GCR bulk in the inner heliosphere) were sampled at 0.067 Hz above 70 MeV n^{-1}. Hourly-averaged data allowed for the study of long-term and short-term GCR flux variations with a statistical uncertainty of 1%.

Since LPF was in orbit for one year and a half during the descending phase of the solar cycle N. 24 in a positive polarity period, a corresponding increase in the mean GCR count-rate during the mission elapsed time was observed. A study of the complete LPF dataset allowed to investigate the role of interplanetary processes in modulating GCRs. Periodicities related to the Sun rotation and their association with solar wind disturbances are discussed. A detailed study of transient GCR flux short-term variations is also presented. The most intense transient processes of solar origin are represented by the interplanetary counterparts of coronal mass ejections (ICMEs), explosive phenomena during which the Sun releases huge amount of plasma material that is convected in the heliosphere. The typical signature on GCR observations of an ICME transit is a sudden intensity decrease and a gradual recovery, called Forbush decrease (FD). Three FDs were observed during the LPF mission elapsed time.

The second part of this work focuses on the characterization of a FD observed on board LPF on August 2, 2016. A dedicated numerical simulation aiming to reproduce observations was carried out. A novel approach is proposed in order to take into account the influence of coherent magnetic field structures on GCR flux variations. A subset of ICMEs carries closed magnetic structures rooted at the Sun and convected out by the solar wind, called magnetic clouds (MCs). Their quasi-3-D magnetic field topology is retrieved using the Grad-Shafranov (GS) reconstruction, an advanced data analysis technique aiming to recover a magnetic flux-rope structure starting from single S/C data. The GS reconstruction outcome is used here in combination with a dedicated particle propagation code. Many attempts in studying formation and time evolution of MC-driven FDs were recently proposed by using various analytical magnetic field models. The realistic MC configuration provided by the GS reconstruction represents a step-forward with respect to previous models. To our knowledge, this work constitute the first attempt to merge the GS reconstruction with a dedicated Monte Carlo test-particle simulation for reproducing the GCR flux modulation ascribable to a MC transit.

Chapter 1

The LISA Pathfinder mission

An overview of the characteristics of the ESA LPF mission is presented in this chapter. LPF was aimed for the technology testing of the instrumentation that will be placed on board the future LISA interferometer for low-frequency gravitational wave detection in space. In particular, the instruments devoted to the interplanetary medium monitoring, PDs and magnetometers, are described in detail.

1.1 Mission overview

The detection of gravitational waves at frequencies smaller than 1 Hz with laser interferometry presents challenges which can be solved only by placing instruments in space. The LISA mission led by ESA is a space-based version of the ground-based LIGO and VIRGO interferometers (Abbott et al., 2016). LISA is designed to establish a multi-link space laser interferometer with an arm length of 2.5 million km that separates three satellites in a triangular arrangement. Each satellite will host two cubic test masses (TMs) of of 46.000 ± 0.005 mm side that must, nominally, remain in free fall. These TMs play the role of mirrors of the interferometer and laser beams monitor their distance between different S/C along the experiment sensitive axis. The gravitational wave signal can be detected with a proper combination of the measured laser phase shifts. LISA is designed to be sensitive to perturbations of the spacetime at a level of about 1 part in 10^{20} in $h/\sqrt{\text{Hz}}$ at frequencies from 0.1 to 100 mHz. Many technological challenges raised by the LISA design could not be tested on ground and consequently, ESA found as necessary to fly LPF, a dedicated technological precursor mission for LISA. The LPF mission allowed to reproduce one of the LISA arms with a length of just

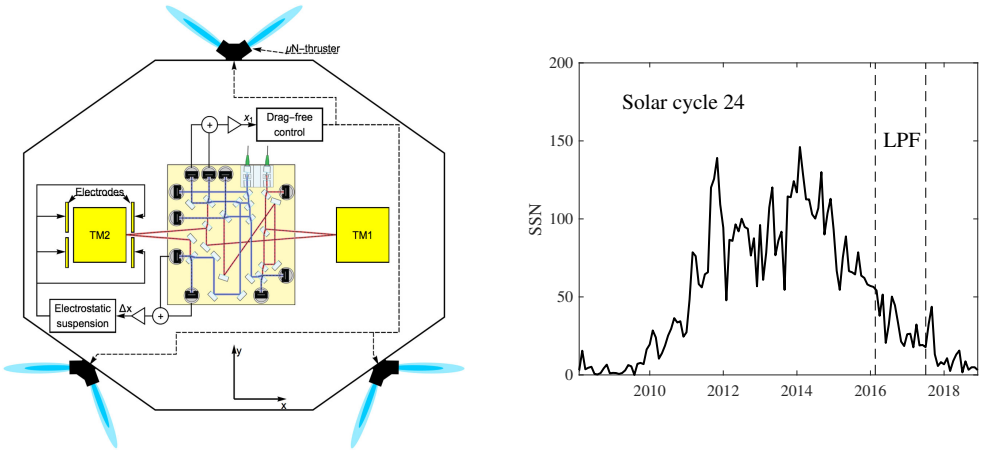

Figure 1.1 Left: sketch of the LPF satellite. The figure shows the two TMs (TM1 and TM2) and two independent interferometers allowing for positioning the TMs with respect to the satellite and among them along the experiment sensitive axis. Electrodes for TM actuation and electrostatic positioning are also shown (Armano et al., 2016). Right: monthly-averaged sunspot number during the solar cycle N. 24. Vertical dashed lines indicate the LPF mission elapsed time.

376.00±0.05 mm within a single S/C. The TMs weight 1.928±0.001 kg and are composed of a high-purity gold-platinum alloy (see Figure 1.1; left panel). Both TMs are contained within an electrode housing which acts as an electrostatic shield in addition to be a six degrees-of-freedom sensor and an electrostatic force actuator. Charge accumulated in the TMs due to cosmic rays and high-energy solar particles is removed by a UV light discharging system. LPF allowed for the testing of different subsystems that will be placed on board LISA even though did not present any gravitational-wave detection capabilities. LPF hosted the ESA LISA Technology Package (Vitale et al., 2005, LTP) and the National Aeronautics and Space Administration (NASA) Disturbance Reduction System (DRS) with colloidal thrusters (Armano et al., 2015). The LPF S/C was launched with a Vega rocket from the Kourou base in French Guiana on December 3, 2015. The satellite reached its final six-month orbit around the first Lagrangian point L1, at 1.5 million km from Earth in the Earth-Sun direction, at the end of January 2016. The S/C elliptical orbit was inclined by about 45° to the ecliptic (see Figure 1.2). The minor and major axes of the orbit were approximately 0.5 million km and 0.8 million km, respectively. LPF remained into orbit during the decreasing part of the solar cycle N. 24 when the averaged monthly

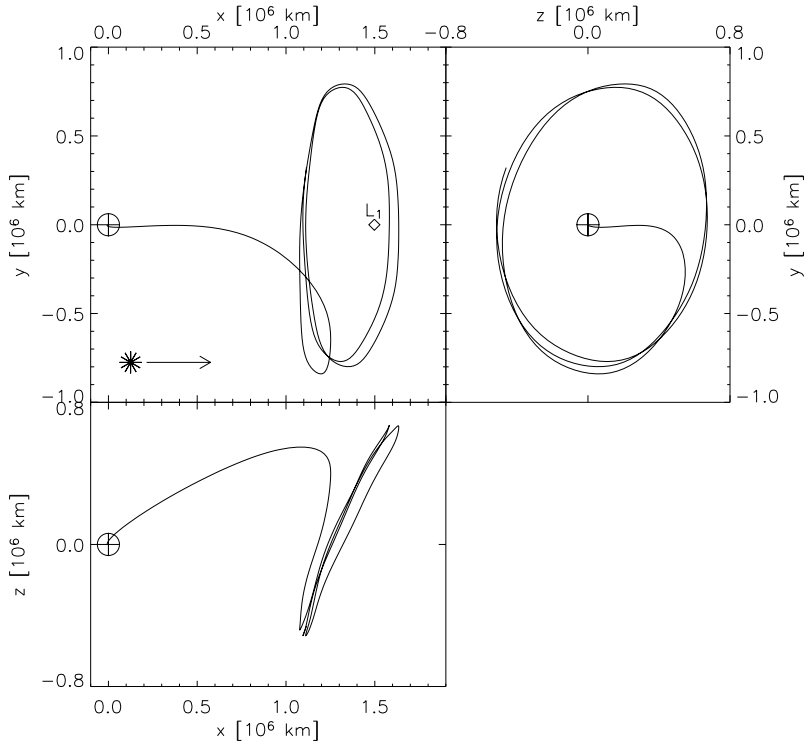

Figure 1.2 LPF orbit in a synodic (corotating) frame having the Earth as the origin. The x-axis points along the direction towards the Sun and the x-y plane lies on the ecliptic. The z-axis is chosen to form a right-handed coordinate system (Landgraf et al., 2005)

sunspot number decreased from 57 through 18 (Figure 1.1; right panel).

1.2 The LISA Pathfinder particle detector

Cosmic and solar particles with energies larger than 100 MeV n^{-1} penetrated approximately 13 g cm^{-2} of S/C and instrument materials and charged the TMs. The TM charging process was expected to constitute one of the main sources of noise for LISA-like space interferometers (Shaul et al., 2006; Armano et al., 2017). A PD placed on board LPF allowed for *in situ* monitoring of protons and helium nuclei (Figure 1.3). This PD was mounted behind the S/C solar panels with its viewing axis oriented along the Earth-Sun direction. It consisted of two $\sim$ 300 μm thick silicon wafers of 1.40 $\times$ 1.05 cm^2 area, placed in a telescopic arrangement at a

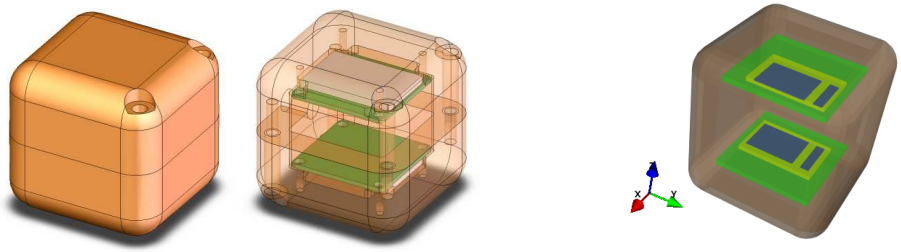

Figure 1.3 Sketch of the PD shielding copper-box and silicon wafers. On the right is reported the PD model used for the GEANT4 simulation (Mateos et al., 2010). Simulations of the PD performance were also carried out with Fluka (Grimani and Vocca, 2005; Grimani et al., 2009).

distance of 2 cm. A shielding copper box of 6.4 mm thickness surrounded the silicon wafers in order to stop ions with energies smaller than 70 MeV n^{-1}. This conservative choice was made in order to not underestimate the overall incident particle flux charging the TMs. The counting of particles traversing each single silicon layer (single counts) were returned to the telemetry every 15 s. The energy deposits in the rear detector of particles traversing both silicon wafers in less than 525 ns (coincidence mode) were stored on the on board computer in histograms of 1024 energy linear bins from 0 MeV to 5 MeV and returned to the telemetry every 600 s. The PD geometrical factor for particle energies > 100 MeV n^{-1} was of 9 cm^2 sr for each silicon wafer for single counts and about one-tenth of this value for particles in coincidence mode. The maximum allowed detector count rate was 6500 counts s^{-1} in the single count configuration. In coincidence mode 5000 energy deposits per second was the saturation limit corresponding to an event proton fluence of 10^8 protons cm^{-2} at energies > 100 MeV. The spurious test-mass acceleration noise due to the charging process was estimated before the mission launch with Monte Carlo simulations on the basis of GCR and solar energetic particle (SEP) flux predictions at the time the mission was supposed to be sent into orbit. Charging process studies were carried out with both Geant4 (Wass et al., 2005) and Fluka (Grimani et al., 2015).

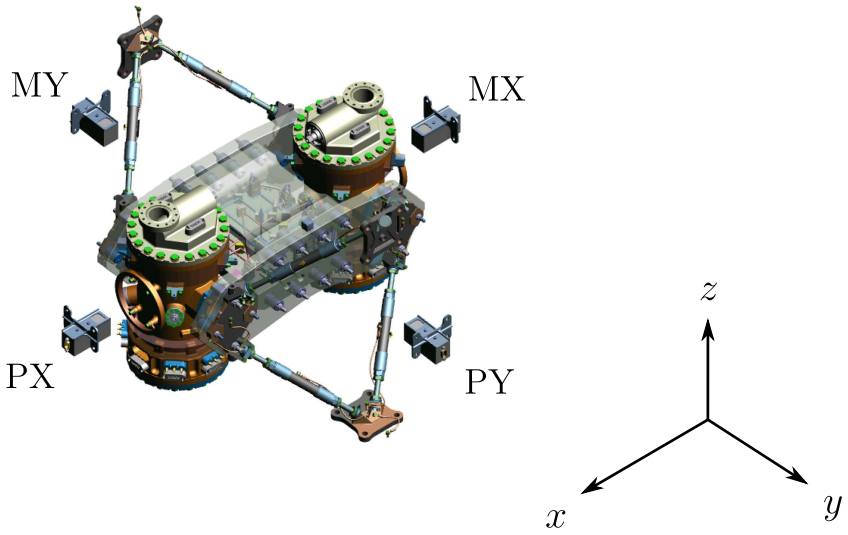

Figure 1.4 A schematic view of the LTP with indicated magnetometers location (MX, MY, PX, PY) within the LPF S/C with respect to the TM electrode housing (adapted from Diaz-Aguilo et al., 2011).

1.3 The LPF magnetometers

Measurements of magnetic field intensity and fluctuations within the vacuum enclosure were not allowed. In order to monitor the magnetic disturbances on board the satellite, four magnetometers (MX, MY, PX and PY) were placed in the LTP at a distance of about 19 cm from the TMs in a cross-shaped configuration. Billingsley TFM100G4-S fluxgate tri-axial magnetometers were placed on LPF. Since the LTP was placed at the center of the S/C platform, the magnetometer sensing axes were aligned with the interferometer reference frame as shown in Figure 1.4. Each magnetometer was composed of three different magnetic sensors aligned along the x, y and z directions. They consisted of an inner drive (primary) coil with a high permeability magnetic core material surrounded by a sensing (secondary) coil. The magnetometers could be operated in the temperature range from $-55°$ to $80°$ with a sensitivity of 60 μV nT^{-1} and a flat frequency response from DC up to 3.5 kHz. Magnetic field data were gathered at rate of 1 Hz.

Chapter 2

Galactic cosmic rays

Main features of cosmic-ray particles are presented in this chapter. Cosmic rays are produced in galactic and, most likely, extra-galactic astrophysical sources. The overall cosmic-ray flux observed in the inner heliosphere appears modulated by the particle propagation process in the solar cavity with respect to the interstellar counterpart. In the vicinity of the Earth, cosmic rays are further deflected by the geomagnetic field and interact with the atmosphere thus producing secondary particles. Space-based detectors for direct cosmic-ray observations and ground-based neutron monitors (NMs) are described here.

2.1 Composition and spectrum

The expression *cosmic rays* was introduced for the first time by R. Millikan in 1926 (Millikan and Cameron, 1926) and indicates the extraterrestrial ionizing radiation discovered by V. Hess (Hess, 1912) a few years before. Hess carried out a series of pioneering balloon flights in order to measure the ionizing radiation while approaching an altitude of about 5 km above the Earth surface. By assuming an Earth origin for this radiation, Hess was expecting to observe a decreasing intensity with increasing altitude. Conversely, the radiation intensity was increasing at high altitudes suggesting that an extraterrestrial radiation was responsible for these observations. At the beginning of 1900, the only known penetrating radiation could be ascribable to incident photons. Only several years later it was discovered that cosmic rays consist essentially of nuclei (99%) with a minor fraction of electrons (1%), positrons (0.1%) and antiprotons (0.01%). *Primary* cosmic rays are those accelerated by astrophysical sources, while those produced by the interactions of primary cosmic rays

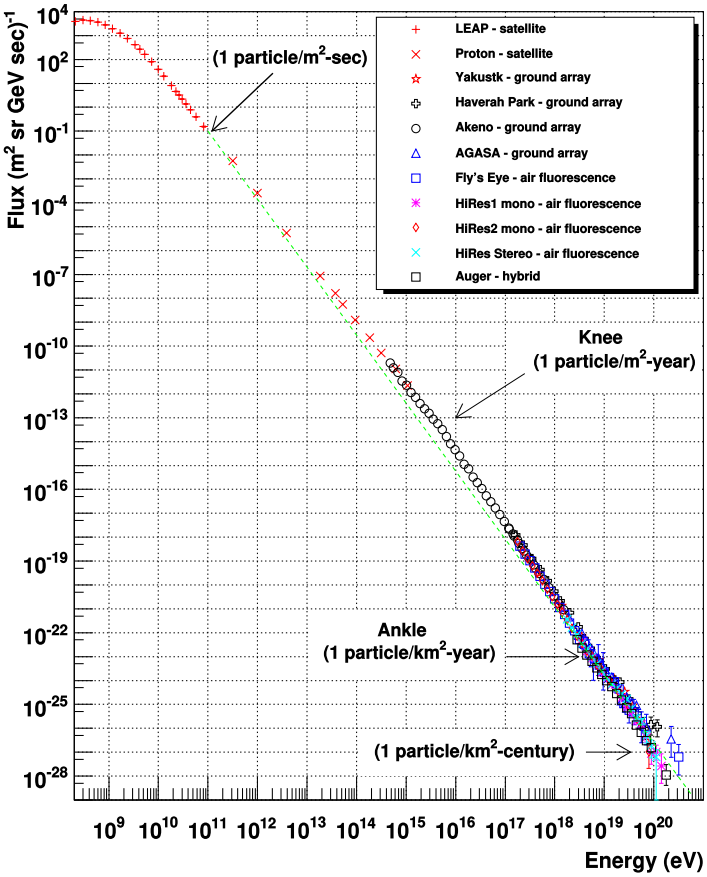

Figure 2.1 GCR energy spectra measurements from various experiments, from http://www.physics.utah.edu/~whanlon/spectrum.html.

in the interstellar medium are called *secondaries*. Among the secondaries, lithium, beryllium, helium-3, boron and nuclei of the iron-group result more abundant in cosmic rays than in the solar system. Nowadays, the term cosmic rays refers generically to particles that are not produced by the Sun with energies ranging between 10^6 eV and $10^{20.2}$ eV according to present observations (Castellina, 2019). Cosmic rays up to energies of 10^{15} eV are supposed to have a galactic origin. The Larmor radius of cosmic rays in the interstellar medium ranges from 10^5 km at the lowest energies through 10^{12} km near 10^{15} eV. Due to the Galaxy dimensions, any information about source location is lost as a result of the particle propagation process.

The cosmic-ray energy differential flux, $J(E)$ measured in m^{-2} sr^{-1} s^{-1} GeV^{-1}, allows for the study of the energy distribution of cosmic rays

as follows

$$J(E) = \frac{dN}{dA\, d\Omega\, dt\, dE}$$

where dN is the number of events observed in the energy range dE with an ideal detector having a geometrical factor $dA\, d\Omega$ during an interval of time dt. Figure 2.1 shows a compilation of proton data obtained with different experiments between 10^8 eV and $> 10^{20}$ eV. Between $\sim 10^9$ eV and $\sim 10^{15}$ eV the GCR energy spectrum presents a single power law trend with a spectral index of -2.7. At about 10^{15} eV, the spectrum becomes softer: this region is called the *knee* of the spectrum. It is generally assumed that this change of slope is due to the leaking process of cosmic rays out of the Galaxy even if a decrease of the efficiency of galactic accelerators cannot be excluded. Recent observations carried out by the Auger collaboration (Castellina, 2019) indicate that at 8×10^{18} eV the cosmic-ray composition changes from light to heavy and that a change of spectrum slope (*ankle* of the spectrum) is present. These evidences seem to suggest that at these energies the origin of cosmic rays changes from galactic to extra-galactic.

2.2 The heliosphere

The heliosphere is the region of space surrounding the Sun inflated by the solar wind. Despite its name, this region appears highly elongated due to the motion of the solar system through the interstellar medium. The heliosphere is bounded by the termination shock at ~ 100 AU from the Sun, where the solar wind makes a transition from a relatively cool supersonic flow to a hot subsonic flow. The subsonic region between the termination shock and the heliopause (i.e. the outer region between the heliosphere and the local interstellar medium) is called heliosheath (see Figure 2.2). The solar wind is a supersonic plasma flowing out of the Sun at velocities of 250-800 km s^{-1} consisting of electrons, protons and alpha particles with energies ranging between 0.5 and 10 keV. At the origin of the solar wind formation there is the high temperature of the solar corona, the upper layer of the solar atmosphere, of approximately 2×10^6 K that drives the plasma outward overcoming the action of the solar gravity (Kivelson, 1995). An interplanetary magnetic field (IMF) is embedded in the solar wind and is convected by this latter one in the radial direction throughout the heliosphere. However, due to the Sun rotation, the IMF is dragged into an Archimedean spiral configuration, known as Parker spiral (Parker, 1958). Given a plasma element on the

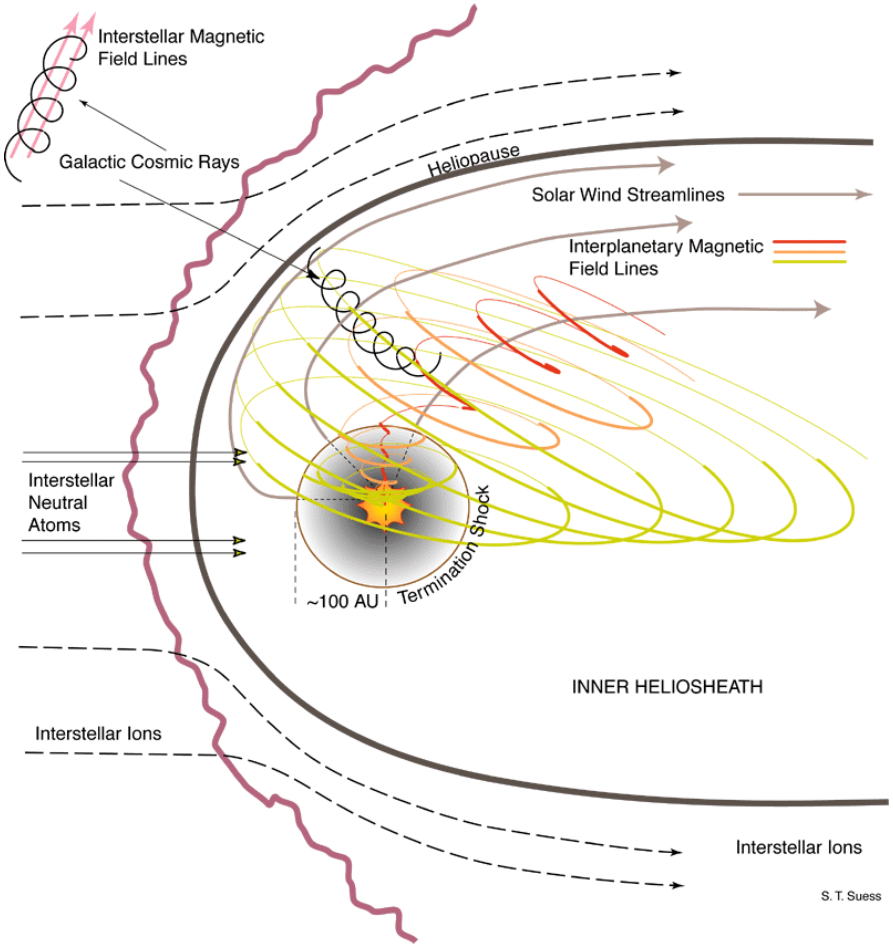

Figure 2.2 Sketch of the heliosphere with surrounding heliosheath and local interstellar medium. Magnetic field lines and solar wind streamlines originated from the Sun extend over the termination shock (at $\sim$ 100 AU from the Sun) and are bounded by the heliopause. The trajectories of GCRs entering the heliosphere are also shown (adapted from https://commons.wikimedia.org/wiki).

Sun placed at longitude ϕ_0, at distance r_0 at a given time $t = 0$ as initial conditions, its position r on the equatorial plane at time t is given by

$$r(t) = r_0 + V(\phi(t) - \phi_0)/\Omega_\odot$$

with

$$r(t) = r_0 + Vt$$

and

$$\phi(t) = -\Omega_\odot t + \phi_0,$$

where V is the radial solar wind speed and $\Omega_\odot$ is the Sun angular velocity. The angle θ formed between the radial direction and the magnetic field $\boldsymbol{B}$ is given by $\tan\theta = r\Omega_\odot/V$. As an example, if the solar wind speed is set at 400 km s^{-1}, the angle θ at Earth distance from the Sun, $r_\oplus = 1$ AU, is of about 45°.

In the Parker's model, the magnetic field vector is described by the equation

$$\boldsymbol{B} = B_r\hat{\boldsymbol{e}}_r + B_\phi\hat{\boldsymbol{e}}_\phi$$

where $\hat{\boldsymbol{e}}_r$ and $\hat{\boldsymbol{e}}_\phi$ are polar coordinate system unit vectors. In the equatorial plane the IMF components are given by

$$B_r = B_0\left(\frac{r_\oplus}{r}\right)^2$$

$$B_\phi = -B_r\frac{r\Omega_\odot}{V} = -B_0\frac{r_\oplus^2\Omega_\odot}{rV}$$

where B_0 represents the IMF intensity at 1 AU. In a coordinate frame rotating with the Sun, it can be shown that $V_\phi/V_r = -r\Omega_\odot/V = B_\phi/B_r$, where V_r and V_ϕ are the radial and tangential components of the solar wind velocity $\boldsymbol{V}$. The magnetic field lines are directed outward (positive) or inward (negative) from the Sun depending on the magnetic polarity of the photospheric footpoint of the field lines. The IMF positive-negative domains are separated by a high electric current called heliospheric current sheet (HCS). The HCS represents an extension of the Sun equator throughout the heliosphere. A model of the HCS, shaped as a *ballerina skirt*, is shown in Figure 2.3. This current layer is not aligned with the equatorial plane, but tilted by a few tens of degrees mainly at solar maximum. The HCS is a strongly dynamical system disturbed by the passage of interplanetary structures.

The heliosphere is also populated by high-energy particles of galactic and solar origin. SEPs are accelerated by solar disturbances up to GeV

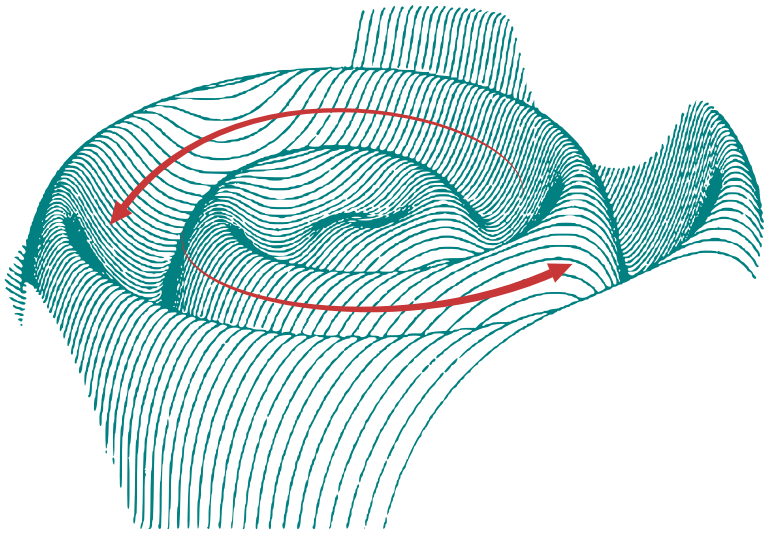

Figure 2.3 Sketch of the HCS configuration (adapted from Jokipii and Thomas, 1981).

energies. They may originate from solar-flare sites or may be accelerated by shocks associated with the propagation of coronal mass ejections (CMEs). CMEs are explosive processes in which a huge amount of material is released from the solar corona. The effects of the propagation process through the heliosphere on the observed GCR flux are described in the next chapter.

2.3 GCR observations in space

Direct measurements of cosmic rays are carried out with balloon, satellite and International Space Station (ISS) experiments at the top or well above the Earth atmosphere. The interactions of cosmic-rays with the Earth atmosphere generate particle showers that, for very high energy primaries, can be also observed at ground-level. The majority of direct cosmic-ray observations is concentrated below the *knee* region since at energies $> 10^{15}$ eV the low particle flux (one particle m^{-2} yr^{-1}) makes feasible only indirect observations with very large ground-based detectors. Early investigations on cosmic-ray physics were carried out with stratospheric balloons. The maximum height that stratospheric balloons can reach is of about 40 km. At this altitude a residual atmosphere of about 5 g cm^{-2} is found. In order to separate rare negative particles

from the bulk of positive GCRs, Alvarez and his students, R. L. Golden and A. Buffington, adopted for the first time the use of a magnetic spectrometer (Rossi, 1964). Magnetic spectrometers allowed R. L. Golden (Golden et al., 1979) and E. Bogomolov (Bogomolov et al., 1979) to discover antiprotons in cosmic rays in the late 1970s. Since then, the New Mexico balloon-borne magnet facility was flown several times. In particular between the 1980s and 1990s the experiments MASS89, MASS91, TS93, CAPRICE94 and CAPRICE98 allowed for a series of positron and antiproton observations at different energy ranges. Although very interesting scientific results were obtained with balloons, small geometrical factor and short duration of flights imposed severe limitations to the statistical precision of measurements and energy range of observations. It is also worthwhile to recall that positrons and antiprotons of atmospheric origin produced in few g cm^{-2} of residual matter had to be removed from balloon observations. Only long-duration balloon flights, performed mainly from Antarctica by the American-Japanese BESS collaboration, allowed for proton and helium observations precise enough to study both long- and short-term GCR variations.

Space experiments are also affected by mass and power limitation constraints. However, large mission elapsed time compensates small apparatus geometrical factors. The CRIS detector on board the NASA Advanced Composition Explorer (ACE; Stone et al., 1998) allowed for collecting data since its launch in 1997 thus contributing to the study of the cosmic-ray composition in the energy range 100-500 MeV n^{-1}. Observations in this energy range can only made in space since the atmosphere absorbs particles below 500 MeV and the geomagnetic cutoff shields the Earth well above 10 GeV at the equator. During the last decade, fundamental results in cosmic-ray physics were obtained with three magnetic-spectrometer experiments: BESS-POLAR (Thakur et al., 2011), a balloon-borne experiment flown from Antarctica, PAMELA (Adriani et al., 2011) and AMS-02 (Aguilar et al., 2002), the first placed on a Russian satellite and the second on the ISS. Despite the primary scientific objectives of these experiments focused on the measurements of antiparticles for detecting possible signature in cosmic rays of particles produced in exotic sources, major contributions were also given to solar and interplanetary physics of cosmic rays and near-Earth astroparticle physics.

In this thesis work it will be shown that also simple PDs (with geometrical factors of the order of several cm^2 sr) providing a continuous monitoring of the overall GCR flux in the interplanetary medium allow for obtaining precious clues on cosmic-ray interplanetary physics.

2.4 The geomagnetic field

The motion of charged particles near Earth is strongly affected by the global geomagnetic field. This last one consists of two different magnetic structures: the Earth inner magnetic field and the magnetosphere. The Earth inner magnetic field has a magnetic dipole shape with the axis tilted by an angle of about 10° with respect to the Earth rotation axis (at present time). The magnetic axis position varies slowly with time and its time dependence is usually parameterized by a sequence of static configurations. The geomagnetic dipole is usually modeled in spherical harmonics according to the Gauss method with the Schmidt normalization. In geographic coordinates (r, θ, ϕ) the geomagnetic potential is expressed by

$$V(r,\theta,\phi) = Re \sum_{n=0}^{\infty} \sum_{m=0}^{n} \left(\frac{Re}{r}\right)^{n+1} P_n^m(\cos\theta)\{g_n^m \cos(m\phi) + h_n^m \sin(m\phi)\},$$

where $Re = 6371.2$ km is the mean Earth radius, P_n^m are the Schmidt normalized associated Legendre functions of degree n and of order m and g_n^m, h_n^m are the Gauss coefficients set on the basis of magnetic measurements carried out at ground level (Chapman and Bartels, 1940). These coefficients are updated every five years by the International Association of Geomagnetism and Aeronomy (IAGA). The set of Gauss coefficients of the geomagnetic potential represents the International Geomagnetic Reference Field[1] (IGRF).

The magnetosphere indicates the external magnetic field. The magnetospheric configuration is strongly asymmetric in response to the interaction with the solar wind. The magnetopause is located at a distance of 10-12 Re along the Earth-Sun direction from the Earth center during quiescent solar wind conditions, while the magnetotail extends beyond 100 Re in the nightside direction. Many models of the magnetosphere were developed during the last decades (Walker, 1979). All the models include the tilt angle of the internal magnetic dipole as an input parameter. With the advent of the space era it became possible to extend the models from low to high altitudes, eventually including the entire magnetosphere. However, the modeling of the magnetic field in that region

[1]IGRF coefficients are available at the web site: https://www.ngdc.noaa.gov/IAGA/vmod/igrf.html

is much more difficult because the outer region of the magnetosphere is a very dynamical system on short time scales. The extension of the magnetosphere is determined by the balance between solar wind plasma and magnetospheric pressures and its size and shape strongly depend on the interaction with the solar wind. Indeed, the characteristics of the magnetosphere are set by the solar wind speed, the plasma density and IMF strength and direction. In particular, the interaction between the magnetosphere and the IMF becomes strongly effective when the latter is antiparallel to the Earth magnetic field on the front boundary of the magnetosphere. In this case, the geomagnetic and the IMF lines connect and the solar wind mass, energy, and electric field penetrate the magnetosphere. This process is at the origin of geomagnetic disturbances like storms and substorms.

The global geomagnetic field and its interactions with the solar wind have an important effect on the cosmic-ray propagation towards the Earth as the complex magnetic field configuration modifies the particle path. In particular, the shielding effect of the global geomagnetic field vanishes in the polar regions while has its maximum in the near-equatorial ones. By defining the rigidity R as the particle momentum per unit charge:

$$R = r_L\, Bc = \frac{pc}{Ze},$$

where r_L is the Larmor radius, B is the magnetic field, c is the speed of light, p is the particle momentum and Ze is the particle charge, it is possible to describe the particle propagation in the magnetosphere through a *cutoff rigidity*, as a function of the geographic coordinates for particles reaching the top of the atmosphere. For a given geographic point on the Earth, only particles with rigidities above the cutoff can penetrate the magnetosphere for a given direction. The rigidity is measured in GV. Since the geomagnetic field is a dynamical system interacting with the solar wind, the effective cutoff rigidity for GCRs propagating towards the Earth is modified by geomagnetic disturbances. As an example, in Figure 2.4 are reported two effective cutoff rigidity maps corresponding to an unperturbed geomagnetic field condition (top panel) and during a geomagnetic disturbance (bottom panel) for particle vertical arrival directions. It can be observed that the cutoff rigidity decreases with increasing magnetic disturbance intensity thus allowing cosmic ray particles in the interval of rigidities shielded during quiet periods, to penetrate the geomagnetic field.

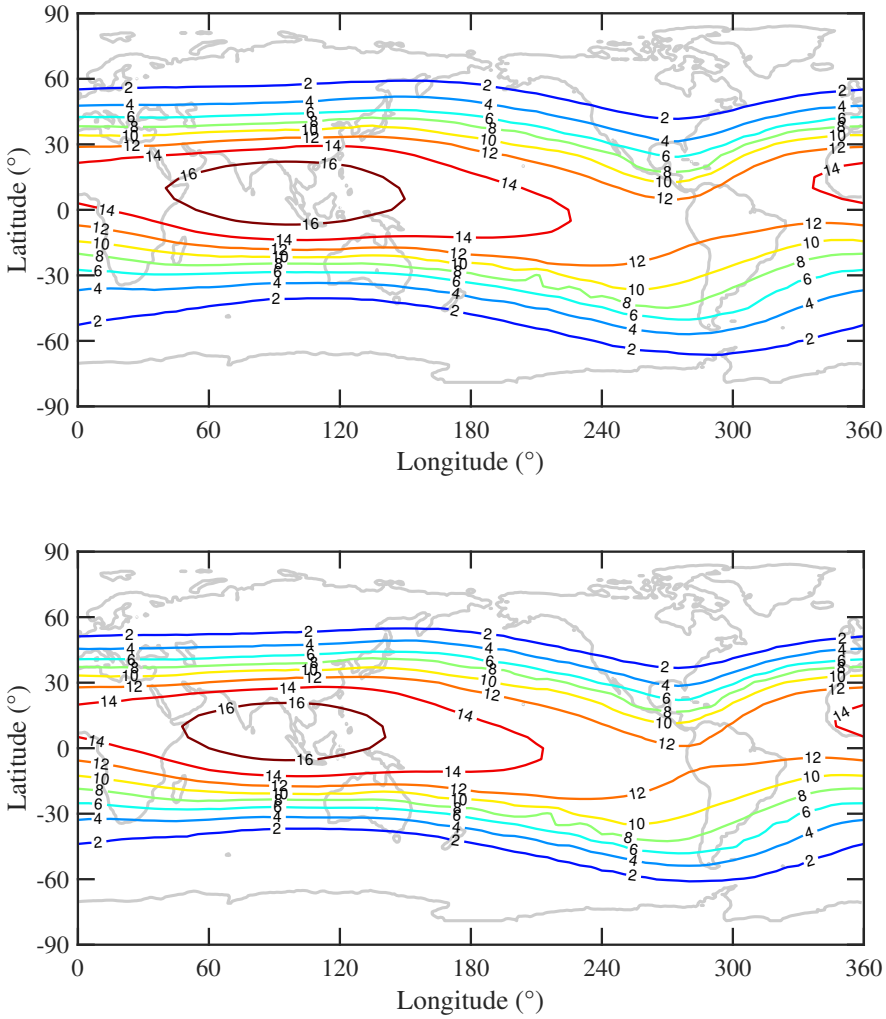

Figure 2.4 Effective cutoff rigidity map for quiet conditions (top panel) and during a geomagnetic disturbance (bottom panel). Rigidity values are given in GV.

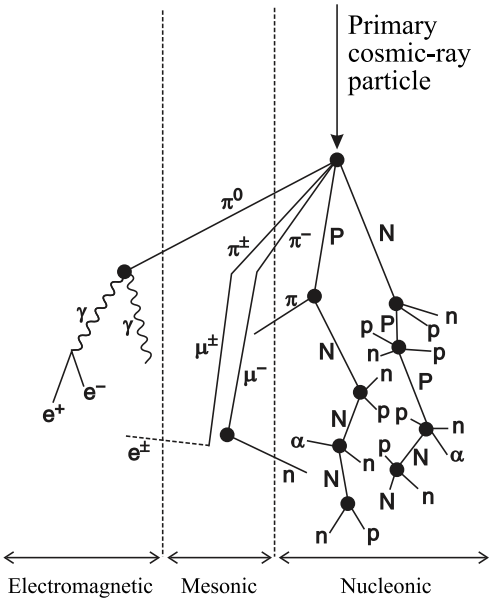

Figure 2.5 Scheme of the cosmic-ray cascading in the atmosphere. Symbols used are: n, neutron, p, proton (capital letters indicate particles produced in nuclear processes), α, alpha particle, $e^{\pm}$, electron and positron, γ, gamma rays, π, pion, μ, muon (adapted from Dunai, 2010).

2.5 The atmosphere

Particles surviving the geomagnetic shielding propagate through approximately 1030 g cm^{-2} of atmosphere. For hadrons, the altitude of the first interaction corresponds to the low stratosphere below which the atmospheric column density increases exponentially. Cosmic rays undergo nuclear spallation and cause fragmentation of atmospheric nuclei. Sputtered nucleons and pions begin cascading in the atmosphere. While neutral pions π^0 decays are at the origin of electromagnetic showers, charged pions $\pi^{\pm}$ decay into muons $\mu^{\pm}$ and muon neutrinos while muons decay in $e^{\pm}$ and muon and electron neutrinos. The cosmic-ray cascade consists of three main components:

- the electromagnetic or "soft" component is formed by gamma-rays, electrons and positrons resulting from the decay of π^0 and $\mu^{\pm}$;
- the mesonic or "hard" component, that is formed by charged pions and their decay products. Muons are mainly formed in the

stratosphere and have a half-life of 2.2 μs in the rest frame. This would be much less than about 40 μs needed for traversing the atmosphere, however the relativistic time dilation allows muons to be the main component of charged particles at Earth level being particles weakly interacting and losing their energy mainly through ionization in the atmosphere;

- the nucleonic component at ground level consists for 98% in composition of secondary neutrons since these particles do not undergo ionization energy losses during propagation in the atmosphere.

The minimum energy that a cosmic-ray particle must present at the top of the atmosphere in order to propagate through the ground is about 500 MeV n^{-1}: this energy is also indicated as *atmospheric cutoff*. A scheme of the cosmic-ray cascade in the atmosphere is shown in Figure 2.5.

2.6 GCR observations at ground-level

In the 1950s detectors dedicated to the study of the Earth-level cosmic-ray nucleonic component, the NMs, were conceived and built for the first time (Simpson et al., 1953). Since then, several instruments placed at different geographic latitudes, have provided a continuous monitoring of the GCR flux at ground-level. Therefore NMs complement cosmic-ray investigations of space-based cosmic-ray detectors. The NM network represents an excellent resource to study primary cosmic-ray flux variations associated with the 11-year solar cycle modulation and with the occurrence of interplanetary disturbances. The NM network in combination with the global geomagnetic field represents a giant spectrometer enabling the determination of GCR spectral variations in the near-Earth environment. Moreover, the simultaneous detection of cosmic-ray particles with the global NM network provides useful information about the anisotropy of the cosmic-ray flux at the Earth as the viewing direction of each NM station depends on its geographic position, on the geomagnetic configuration, on the particle rigidity and on the particle direction of incidence. In order to study the variation of the primary cosmic-ray flux in the near-Earth environment from NM measurements, the relationship between the NM count rate and the primary cosmic-ray flux must be known. In particular, the transport in the atmosphere, the modeling of energetic particle interactions with atmospheric gas particles, and the NM detection efficiency are essential information to make a reliable estimate of the cosmic-ray flux at the top of the atmosphere. Secondary

atmospheric particle production and detection of nucleons by NMs are combined in the *NM yield function* that can be used to determine the cosmic-ray flux at the top of the atmosphere starting from NM measurements. Two methods are used to determine the NM yield function: the parameterization of various observations as a function of the geographic latitude, the most commonly used is the Dorman function (Dorman and Yanke, 1981) and the Monte Carlo simulations of cosmic-ray transport through the atmosphere and NM detection efficiency.

Each NM station is characterized by the local cutoff rigidity and an effective energy. Above the effective energy NMs allow for a direct measurement of GCR flux since the NM count rate is proportional to the integral flux at the top of the atmosphere. Effective energies range from 11-12 GeV for polar NMs through > 30 GeV for equatorial stations (Gil et al., 2017).

Chapter 3

Galactic cosmic ray flux variability

The GCR intensity changes continuously in the heliosphere in response to solar wind and IMF variations. This process is known as modulation of the GCR flux. GCR flux variations are classified according to their characteristic time scales:

- long-term variations: GCR flux variations occurring over periods of time longer than one year resulting mainly correlated with the 11-year solar activity cycle and the 22-year GSMF polarity reversal. It is worthwhile to recall that the solar polarity is called positive (negative) when the solar magnetic field lines are directed outward (inward) from (to) the Sun North Pole.

- Short-term variations: GCR flux variations lasting less than one month in response to interplanetary processes such as corotating interaction regions (CIRs), originated by the interaction between slow and fast solar wind streams, ICMEs, HCS crossings and others.

In this chapter the effects of long- and short-term GCR flux variations are discussed along with their association with solar activity and interplanetary processes.

3.1 GCR flux long-term variations

Fluxes of GCRs propagating from the interstellar medium to the point of observation in the heliosphere are modulated by particle interactions with the interplanetary solar wind and magnetic field. Local interstellar (LIS)

spectra of GCRs are considered input data for the models that allow for reproducing the trend of observations as a function of position, energy and time in the heliosphere. The modeling of the GCR propagation process was firstly introduced by Parker (1965) with the particle transport equation. After defining the particle distribution in space, $f(\boldsymbol{r}, R, t)$, as a function of position $\boldsymbol{r}$, rigidity R and time t, Parker modeled the energetic particle transport in the solar wind by assuming that the irregularities of the magnetic field would have scattered cosmic-ray particles in a random-walk-like transport. On the basis of the Fokker-Plank approach, the Parker equation appears as follows

$$\frac{\partial f}{\partial t} = -(\boldsymbol{v} + \langle \boldsymbol{u}_d \rangle) \cdot \nabla f + \nabla \cdot (\boldsymbol{\kappa}^S \cdot \nabla f) + \frac{1}{3}(\nabla \cdot \boldsymbol{v}) \frac{\partial f}{\partial \ln R}, \tag{3.1}$$

where $\boldsymbol{v}$ is the solar wind velocity, $\langle \boldsymbol{u}_d \rangle$ is the average particle drift velocity and $\boldsymbol{\kappa}$ is the diffusion tensor. The diffusion tensor can be splitted in two parts: the symmetric part $\boldsymbol{\kappa}^S$, related to the particle diffusion and the antisymmetric part $\boldsymbol{\kappa}^A$, describing the gradient and curvature drifts. The vector

$$\langle u_{d,i} \rangle = \frac{\partial \kappa^A_{ij}}{\partial x_j}$$

is the pitch-angle-averaged guiding-center drift velocity (Jokipii et al., 1977). With respect to the drift process, positively charged particles propagate mainly sunward in the ecliptic along the HCS during negative solar polarity periods and from the Sun's North Pole towards the HCS during positive polarity epochs. The opposite holds for negatively charged particles. Particles propagating along the HCS lose more energy than those coming from the poles. The right-hand side of equation (3.1) contains: 1) the convection term related to the solar wind velocity $\boldsymbol{v}$ and the average particle drift velocity $\langle \boldsymbol{u}_d \rangle$, induced by gradients and curvature of the IMF 2) the diffusion term with the associated symmetric diffusion tensor and 3) the particle adiabatic energy loss term. The same equation was derived more rigorously by Gleeson and Axford (1967). These authors considered also a solution of the transport equation, in the force-field approximation, which, since then, was widely used in the literature (Gleeson and Axford, 1968, hereafter G&A68). For a comprehensive discussion on the force-field approach see also Caballero-Lopez and Moraal (2004). In G&A68 the equation (3.1) can be reduced to a simple convection-diffusion equation under the following hypotheses:

a) there is a steady particle distribution: $\partial f / \partial t = 0$;

b) the adiabatic energy loss term is neglected;

c) no drift process is considered.

The Parker equation thus reduces to

$$\frac{\partial f}{\partial r} + \frac{vR}{3\kappa}\frac{\partial f}{\partial R} = 0$$

where κ is the diffusion coefficient. By assuming that κ depends only on the particle rigidity and the heliocentric distance, the same can be splitted in the form $\kappa(r, R) = \beta\kappa_1(r)\kappa_2(R)$. This assumption was justified by experimental observations carried out between 1 AU and 1.6 AU during the period December 1963-June 1965, (O'gallagher and Simpson, 1967). A modulation parameter $\phi(r)$ is then defined as follows

$$\phi(r) = \int_r^{r_b} \frac{v(r')}{3\kappa_1} dr' \tag{3.2}$$

where r_b is the distance of the outer boundary of the modulation region from the Sun. According to G&A68, the GCR differential energy spectrum at 1AU in the force-field approximation is given by

$$J_{1AU}(E) = J_{LIS}(E + \Phi)\frac{(E^2 - E_0^2)}{(E + \Phi)^2 - E_0^2} \tag{3.3}$$

in units of particles m^{-2} sr^{-1} s^{-1} MeV^{-1}, where E_0 is the particle rest mass, E is the total energy and Φ is the force-field energy loss. For particles with rigidities larger than 100 MV, the effect of the solar activity is completely defined in terms of the solar modulation parameter

$$\Phi = \frac{Ze}{A}\phi,$$

where Z and A are charge and mass number of the GCR particle, respectively. In the case of protons the mass to charge ratio is one and the solar modulation parameter has the same value of Φ. As an example, by assuming the LIS proton spectrum reported in Usoskin et al. (2017):

$$J_{LIS} = 2.7 \times 10^3 \frac{E^{1.12}}{\beta^2}\left(\frac{E + 0.67}{1.67}\right)^{-3.93} \tag{3.4}$$

where $\beta = v/c$ represents the particle velocity and $\phi = 500$ MV, the obtained modulated proton flux is reported in figure 3.1 and compared to

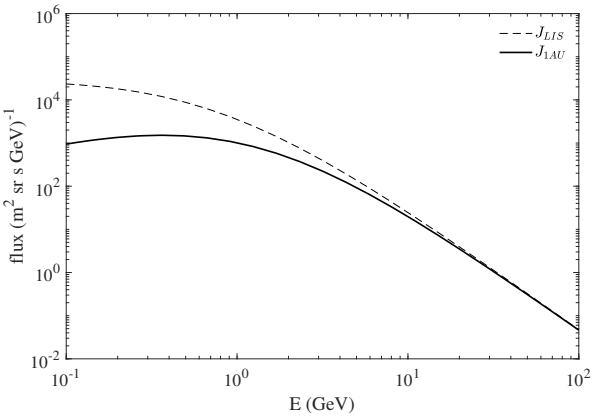

Figure 3.1 Example of GCR proton flux parameterization at 1AU. The dashed line represents the LIS proton spectrum defined in equation (3.4), while the solid line is the modulated spectrum on the basis of equation (3.3) where a solar modulation parameter $\phi = 500$ MV is considered.

the LIS spectrum. The energy spectra, $J(E)$, obtained with the G&A68 model can be interpolated with the function appearing in equation (3.5), which is well representative of the GCR observation trend in the inner heliosphere between a few tens of MeV and hundreds of GeV within experimental errors (Papini et al., 1996)

$$J(E) = A(E+b)^{-\alpha}E^{\beta} \qquad \text{particles (m}^2\text{ sr s GeV n}^{-1})^{-1}, \qquad (3.5)$$

where E is the particle kinetic energy per nucleon and A, b, α, and β are coefficients inferred from individual sets of data. The advantage of adopting this parametrization with respect to the simple use of the outcomes of the G&A68 model relies on the possibility to vary the parameter b in order to disentangle the role of the solar modulation from the solar polarity and from GCR flux short-term variations, when short-term variations superpose to the average effect of the long-term modulation. In order to study the effectiveness of the G&A68 model, predictions were compared to data gathered by the BESS experiment during different periods of solar activity and solar polarity (Shikaze et al., 2007; Grimani, 2007a,b) as shown in Figure 3.2 (left panel). In this figure it can be noticed that measurements span over approximately one order of magnitude at 100 MeV n^{-1} from solar minimum through solar maximum (see for instance Papini et al., 1996). The model reproduces the observed data trend (middle continuous curves) during positive polarity periods

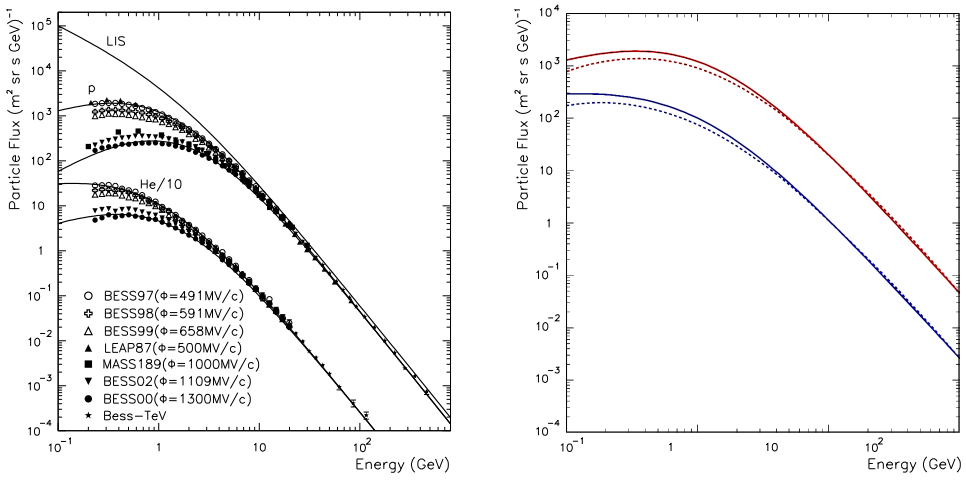

Figure 3.2 Left: GCR proton and helium energy spectra measurements and parameterizations. The solar modulation parameter ϕ estimated for each set of measurements is reported in the legend. Observations were gathered during different solar activity and both positive (open symbols) and negative (solid symbols) polarity periods. The top curve corresponds to the LIS spectrum by Shikaze et al. (2007). The continuous middle and bottom curves correspond to $\phi = 490$ MV and $\phi = 1300$ MV respectively, from (Grimani, 2007b). Right: GCR proton (red curves) and helium (blue curves) fluxes. Top continuous curves correspond to observations gathered at solar minimum during positive polarity periods. Bottom dashed lines represent the maximum effect of the drift process during negative polarity periods (Boella et al., 2001).

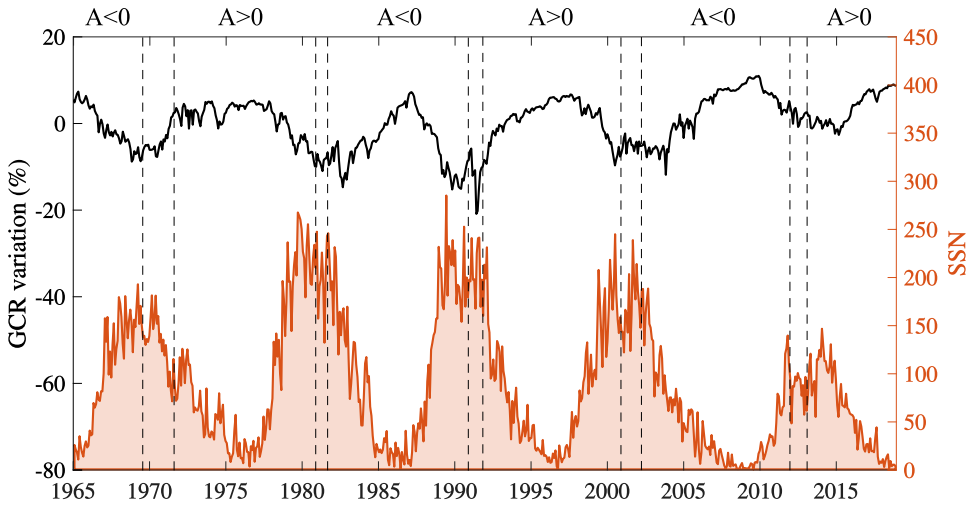

Figure 3.3 Oulu NM GCR count-rate variations (black line) compared to the observed sunspot number (red line). Positive ($A > 0$) and negative ($A < 0$) polarity periods are indicated on the top of the figure. Vertical dashed lines delimit periods of not well-defined GSMF polarity according to Laurenza et al. (2014) and `http://www.solen.info/solar/polarfields/polar.html`.

when the indicated LIS proton spectrum in considered, while during negative polarity periods the low-energy and high-energy data trend cannot well be reproduced at once (see in particular the BESS00 data and the bottom continuous lines in Figure 3.2). This evidence reveals that the drift process contributed to modulate the observed proton and helium fluxes. In Boella et al. (2001) and Gil and Alania (2016) it was shown that in space the maximum modulation of positive particle fluxes during negative polarity periods ranges from 40% at 100 MeV n^{-1} through a few percent at 4 GeV n^{-1} with respect to measurements carried out during opposite polarity epochs (see right panel of Figure 3.2). At solar maximum, the drift process is found to play a minor role. A signature of the polarity of the GSMF is also impressed in NM data.Webber and Lockwood (1988) have shown, by using NM data from 1952 through the end of 1987, that GCR observations gathered during different polarity epochs present alternate "flat-topped" and "peaked" patterns as it can be observed in Figure 3.3. NM GCR observations present a "flat-topped" trend during positive polarity periods and a "peaked" pattern during negative polarity epochs. These features were found to be in agreement with the expected effect of curvature and gradient drifts of cosmic-ray

protons in the heliosphere (Jokipii et al., 1977; Kota and Jokipii, 1983; Ferreira and Potgieter, 2004; Potgieter, 2013; Laurenza et al., 2014).

3.2 GCR flux short-term variations

The Sun is a massive sphere of plasma and gas rotating at different velocities depending on the heliolatitudes. The equator and near equatorial regions rotate with a period of about 25-26 days: representing the Sun sideral rotation period. For an observer at the Earth this periodicity equals to about 27-28 days due to the orbital motion of the Earth. This is called the Sun synodic period of rotation. At the poles the Sun rotates with a period of about 36 days. The distribution of active regions and coronal holes on the Sun generates a solar wind asymmetric velocity distribution with respect to heliolongitude and heliolatitude. Solar wind disturbances originated by coronal holes and active regions are at the origin of recurrent and transient GCR flux short-term variations observed in both space- and ground-based detectors. GCR short-term variations have typical durations ranging from hours to days and show, in space, intensities of tens of percent at most, while at the Earth remain, in the majority of cases, below a few percent. Transient variations, called FDs, were studied for the first time by Forbush (1937) and Hess and Demmelmair (1937) with the use of ionization chambers and were observed later with both NMs and space-based detectors.

3.2.1 Recurrent GCR flux short-term variations

Sun coronal holes are regions of low density and temperature in the solar corona and represent a well-established sources of recurrent high-speed solar wind streams. Coronal-hole related disturbances are long-living (up to ∼12 months in the years preceding the solar activity minimum), corotating and quasi-stationary plasma structures with solar-wind velocities ranging between about 300 and 900 km s^{-1} at 1 AU. The polarity of the IMF appears to be nearly constant during the disturbance (Storini, 1990). The interaction of a high-speed solar wind stream with the background slow solar wind produces a compressed, heated plasma region with enhanced magnetic field intensity. The magnetic field carried by the slow solar wind is more curved due to the lower speed, while the field associated with fast stream is less bent. The boundary region where the fast stream hits the slow wind is called *stream interface* and is characterized by high solar wind speed and proton temperature accompanied by a

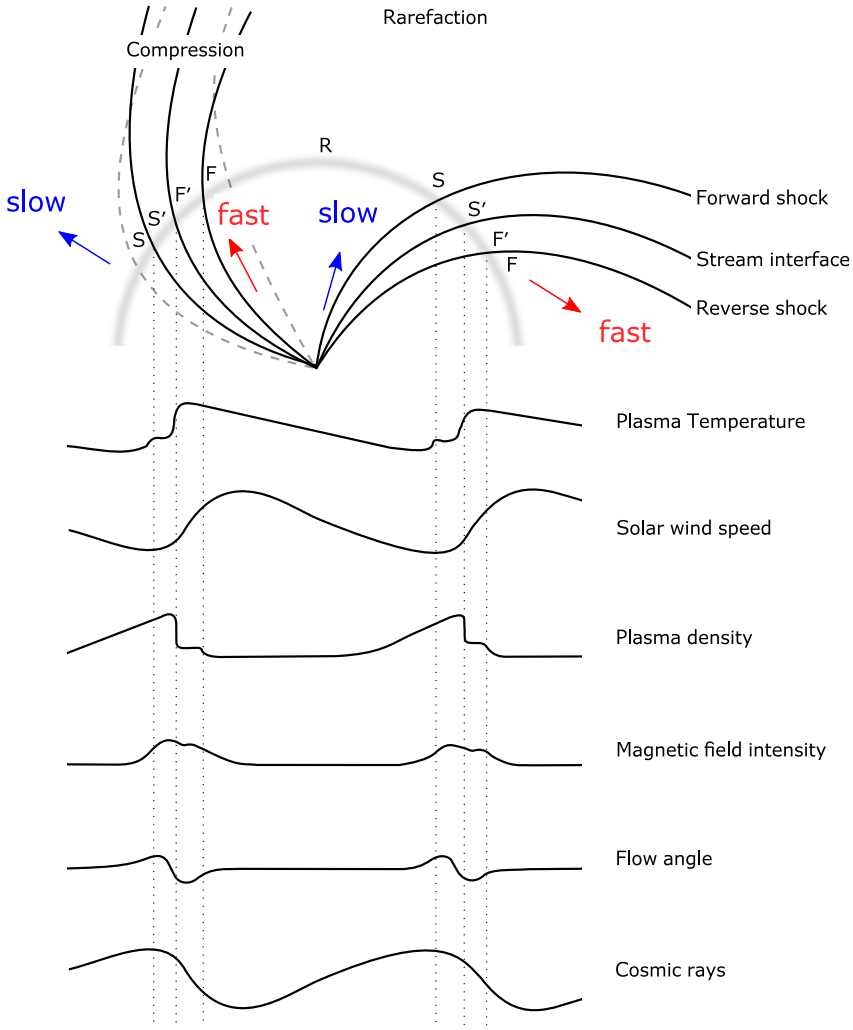

Figure 3.4 Sketch of two high-speed streams corotating with the Sun, showing the formation of CIRs. Dashed lines represent flow streamlines in the slow and fast solar wind. Below typical changes in solar wind parameters at 1 AU corresponding to the indicated regions are listed. Corresponding GCR flux variations are also shown at the bottom of the figure. The regions indicated on the top of the figure are S: ambient, slow solar wind; S': compressed, accelerated, slow solar wind; F': compressed, decelerated, fast-stream plasma, and F: ambient, undisturbed, fast-stream plasma. Forward and reverse shocks are also shown. (Richardson, 2004).

decreasing plasma density profile. The CIR stream interface is generally bounded by a *forward shock* and a *reverse shock*, as shown in the sketch in Figure 3.4. Coronal holes at the origin of high-speed solar wind streams recurrently appear during subsequent solar rotations and impress their signature in the GCR flux resulting in a quasi-periodic modulation. The leading edge of high-speed streams is associated with the onset of the GCR count rate decrease, while the maximum depression amplitude is generally observed when the solar wind speed reaches its maximum value (Richardson et al., 1996). These GCR flux depressions are characterized by gradual decreases occurring during 3-5 days and recoveries lasting 5-7 days.

3.2.2 Transient GCR flux short-term variations

Other areas of the Sun are at the origin of phenomena that affect the interplanetary medium characteristics. Active regions, typically characterized by strong magnetic fields and sunspots (although not all active regions show sunspots) are often associated with explosive phenomena such as solar flares and CMEs. CMEs are plasma eruptions occurring in the solar atmosphere involving previously closed field regions that are suddenly expelled in the interplanetary medium. The Sun material ejected during CME processes is carried by the solar wind throughout the heliosphere originating their interplanetary counterparts (i.e. ICMEs). In general, a region of compressed plasma and turbulent magnetic field (sheath region) is formed at the front edge of an ICME and an interplanetary shock is usually detected at its arrival. A sketch of the ICME structure is reported in Figure 3.5.

Transient variations are characterized by GCR intensity drops of 1-2 days and gradual recoveries of several days associated with the passage of transient solar wind disturbances, e.g. ICMEs, magnetic barriers (MBs) that generate compressed plasma regions, HCS crossings, etc. The most intense GCR flux transient variations are associated with the transit of ICMEs. In the following we will refer as to FDs only to indicate these kind of depressions. FDs show different shapes and sizes from event to event. According to Cane (2000), their properties can be related to the characteristics of the associated CMEs at the Sun and could be divided into three types: ICME with preceding shock, ICME-only, and shock-only. A typical two-step FD, characterized by two visible steps in the count rate decrease, is originated by ICMEs with a shock ahead. The first decrease occurs in the turbulent sheath region and the second one during the ICME transit (see Figure 3.5). The shock is generated at the leading

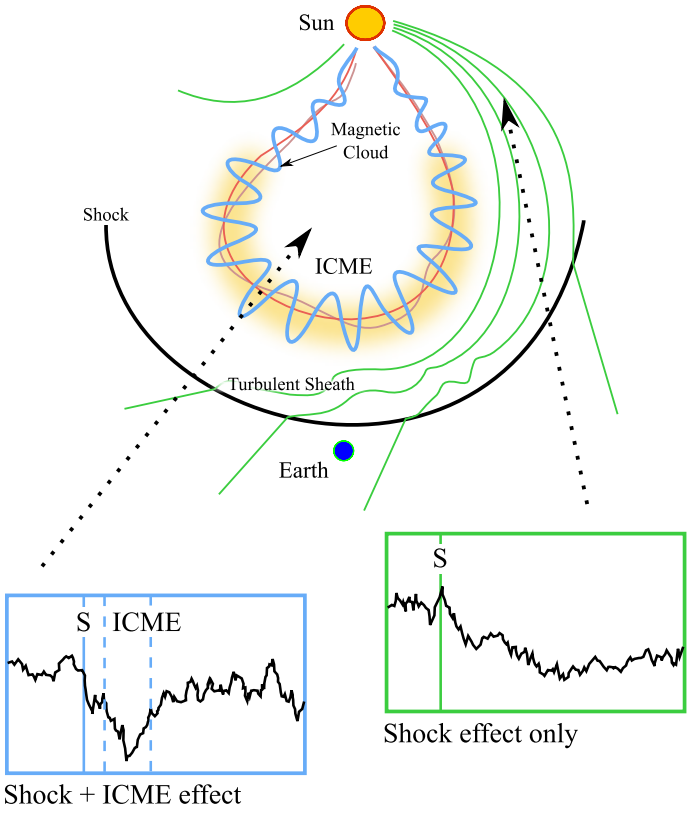

Figure 3.5 Sketch of a large-scale structure of an ICME with shock and turbulent sheath ahead. Two S/C paths through the structure are indicated as an example. The resultant cosmic ray profile depends on the part of the structure explored by the S/C. The time of shock transit S is indicated by a vertical solid line and the start and end times of ICME passage are indicated by vertical dashed lines. Only if the ICME is intercepted the two-step FD can be observed (Richardson and Cane, 2011).

edge of the ICME when it propagates at supersonic speed. For slow ICMEs, ejecta only are present and their passage causes short-duration, one-step FDs. The ICME source region at the Sun sets the direction of

propagation of the ICME, i.e. determines whether the ICME will reach the observer, will pass it by, or will hit the observer with its flank. In the case that an ICME hits an observer goes through the shock passage will be detected. Generally, this happens for CMEs originating outside 50° of the Sun's central meridian. Only very energetic CMEs create shocks strong enough to observe the shock-only effect. These events are often accompanied by intense SEP fluxes.

3.2.3 Forbush decreases and magnetic clouds

The term "magnetic cloud" was introduced by Burlaga and coworkers to indicate structures in the solar wind that present an enhanced magnetic field intensity with a wide smooth rotation of its components accompanied by low values of plasma temperature and plasma-beta (Burlaga et al., 1981). MCs belong to a subset of ICMEs and their configuration consists of a closed plasma structures with field lines helically wrapped around a central axis. The shock/sheath region at the front of the ICME is at the origin of FDs observed in GCRs both in space and Earth, although no rigidity cutoff and the absence of diurnal anisotropies in the space-based measurements allow to better study the fine structure of FDs with respect to NMs. The most important effect of ICME passages in generating major FDs is ascribable to the turbulent-sheath region usually accompanied by an energetic shock. Intense shocks associated with fast ICME propagation in the heliosphere, may overcome the ejecta effect in modulating the GCR flux. When the velocity of propagation of ICMEs is similar to that of the background solar wind velocity, the shock/sheath transit effects on GCR flux does not show any evident signature with respect to the ejecta. The ejecta-driven FDs are generally smaller than the shock/sheath-driven ones. Therefore, if no interplanetary shock is found leading an ICME and a weak magnetic field turbulence is observed in the sheath region, the FD evolution depends on the magnetic topology associated with the inner ICME/MC configuration. In these cases, since the evolution of the GCR flux does not strongly depends on the nature of *in situ* magnetic field and solar wind signatures, it is important to consider the large-scale topology of the MC field lines in modulating the cosmic-ray particle flux without restricting observations to the magnetic fields that are measured along a particular trajectory of a S/C through the ICME (Cane and Richardson, 2003).

The relation between MCs and FDs from both theoretical and numerical points of view have been investigated during last decades using space- and ground-based observations. The theory at the base of these

processes lies on the charged particle motion and the particle transport in magnetic fields. In particular, in this chapter it is pointed out that the GCR transport in the heliosphere, in terms of convection and diffusion processes, is an adequate model to interpret large-scale physical phenomena such as the solar modulation over the 11-year solar cycle during positive polarity periods, but the same approach can be used on spatial and temporal scales typical of large solar wind disturbances (e.g. ICMEs). One of the general assumptions at the basis of theoretical and numerical models to study the FD formation is that empty, closed magnetic structures, simulating the passage of ICMEs and/or MCs, are slowly filled through particle diffusion. In this case, physical quantities, e.g. particle distribution and FD amplitude, are computed by solving the particle transport equation in the diffusion approximation (Cane et al., 1995). This approach provides precious clues on this topic, but many evidences reveal that cosmic-ray diffusion only cannot always explain observations (Richardson and Cane, 2011). In addition to cross-field diffusion, cosmic-ray adiabatic cooling due to ICME expansion is investigated in Munakata et al. (2006), where the best-fit between the theoretical solution and the FD profile measured by a ground-based muon detector network allows to estimate the perpendicular diffusion coefficient. Dumbović et al. (2018) presented an analytical diffusion-expansion model for FDs where the ICME is modeled as an axial magnetic flux-tube expanding from the Sun. In this model cosmic rays penetrate the ICME via perpendicular diffusion and results are in agreement with Cane et al. (1995). Other analytical models based on the diffusion-expansion approach are presented in Arunbabu et al. (2013) and Raghav et al. (2014). In general, results of diffusion-expansion models allow to use the measured FD amplitude to fit the model outcome and thus estimate the perpendicular diffusion coefficient. The TP approach is also used in the literature in order to investigate properties of high-energy particle propagation. For instance, Krittinatham and Ruffolo (2009) have considered GCR transport through an expanding MC structure without including any diffusion process by studying particle propagation in the guiding-center approximation. They point out that for particle propagation through MC closed field lines the particle drift is effective. Recent works emphasize the importance of MC configurations for the study of the FD formation and detection (Petukhova et al., 2017, and references therein). For instance, Petukhova et al. (2019) calculate the time profile of the cosmic-ray distribution function in addition to cosmic-ray anisotropies in a toroidal MC model. In this case the particle distribution is calculated starting from the full-trajectory integration. They show that the MC orientation with

respect to the position of ground-based cosmic-ray detectors strongly influence observations. A technique for the estimate of the MC orientation on the basis of cosmic-ray observations is presented by Kuwabara et al. (2009).

Chapter 4

LISA Pathfinder data analysis

In this chapter the analysis of the PD data for the study of recurrent and transient GCR flux variations observed on board LPF in 2016-2017 is presented. The characteristics of GCR variations are illustrated along with their association with interplanetary disturbances. Moreover, a periodicity analysis is carried out by using the Hilbert-Huang transform (HHT), showing that recurrent modulations, associated with the solar rotation period and higher harmonics, are present. The detected periodicities are interpreted in terms of the interplanetary disturbances affecting GCRs.

4.1 Data treatment and selection criteria

Cosmic-ray data were gathered with the LPF PD at a frequency of 0.067 Hz (see Chapter 1). Only single counts are considered in this work. PD data availability ranges from February 18, 2016 through July 3, 2017 with four data gaps on September 23-25, 2016, on February 16-20, 2017, on April 13-15, 2017 and on April 17-18, 2017. Data gaps are filled with a linear interpolation. Known spurious spiky signals were induced at given intervals of time in the electronics of the PD for testing, therefore a de-peaking procedure was applied after raw data downloading. The PD performance was studied with Monte Carlo simulations and a dedicated beam test before the mission was sent into orbit (Mateos et al., 2012). The lack of redundant cosmic-ray measurements on board LPF led us to verify if any loss of efficiency could have affected the GCR measurements during the mission elapsed time. To this purpose, the mean GCR count rate versus solar activity, in terms of the solar modulation parameter ϕ (see equation 3.2), was studied (see Figure 4.1) for the whole mission duration. Each data point in Figure 4.1 represents the average

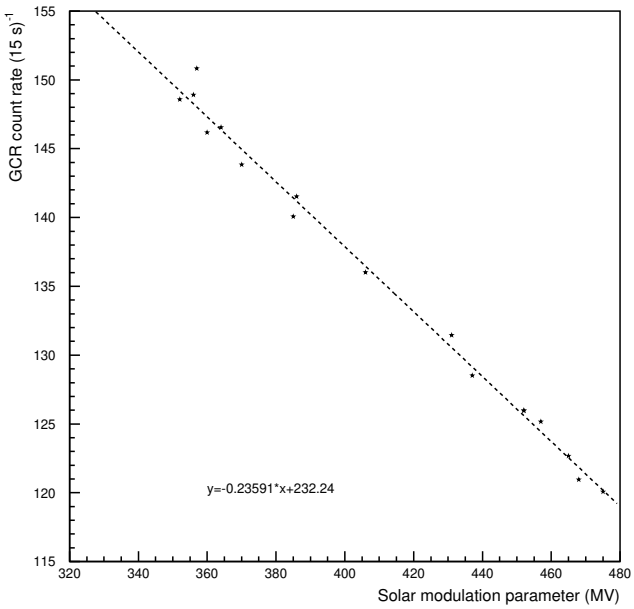

Figure 4.1 LPF PD GCR single count rate averaged over each BR during the LPF mission versus the solar modulation parameter. High (low) values of the solar modulation parameter correspond to mission beginning (end).

cosmic-ray count rate observed during individual Bartels rotation (BR). It is worthwhile to recall that the BR number corresponds to the number of 27-day rotation of the Sun since February 8, 1832. During the time LPF remained in orbit, the solar modulation parameter varied from 550 MV through 320 MV. A linear dependence between the cosmic-ray count rate and the solar modulation parameter can be observed in Figure 4.1 during the whole data acquisition period. In case the PD would have shown an efficiency loss, a sudden drop in the cosmic-ray count rate trend would have been observed. Conversely, only a minor scattering of data for each BR is observed with respect to the linear trend. This feature can be ascribed to the presence of short-term variations due to solar wind disturbances, generating short-term cosmic-ray count rate variations superimposed on the long-term modulation associated with the 11-year solar activity cycle.

Fifteen-second data are hourly averaged in order to limit the statistical uncertainty to 1% on single data point. The complete LPF PD

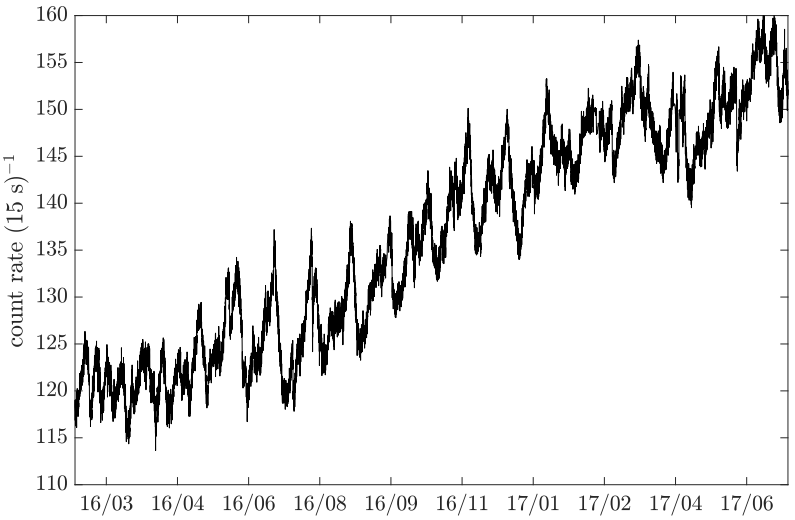

Figure 4.2 Hourly-averaged 15 s LPF PD count rate between February 18, 2016 and July 3, 2017.

time series is shown in Figure 4.2. A visual data inspection of the whole LPF dataset reveals an increasing trend from the beginning through the end of the mission, correlated with the decreasing solar activity, and the presence of quasi-periodic variations. Criteria used for the identification of GCR flux short-term variations were the following: 1) GCR flux depressions with duration > 2 day and 2) amplitude $> 2\%$ were considered. Small increases and depressions with duration < 2 day and amplitudes $< 2\%$ are at the limit of statistical significance and therefore were disregarded. Forty-five depressions were observed for the whole dataset. Six symmetric variations were found with V or U shapes. Thirty-nine depressions were observed to be asymmetric. The period during which the PD count rate remained at minimum values between decrease and recovery phases is indicated as *plateau*. Average characteristics of the GCR flux short-term variations observed with LPF are reported in Table 4.1.

In addition, a visual inspection of the whole dataset revealed the presence of several substructures in the count rate trend spanning over typical time scales < 2 day. A dedicated analysis was carried out to investigate the characteristics of these variations. GCR flux depressions and peaks of duration > 0.75 day (18 hr) with intensities $> 2\%$ were studied. Variations larger than 2% in intensity are considered in order to set the statistical significance of the selection criterion to 2σ, given the 1% of statistical uncertainty on PD hourly averaged single count data. Twenty-three < 2 day depressions were observed. The comparison

Table 4.1. Average characteristics of GCR flux recurrent variations observed with LPF.

	Duration (Days)	(%)
Decrease	2.8 ± 2.0	
Plateau	1.3 ± 1.2	
Recovery	5.1 ± 3.8	
Total duration	9.2 ± 5.0	
Intensity		5.1 ± 2.5

of data gathered during subsequent BRs allows for the detection of the presence of recurrent and transient patterns in the variation of the GCR count rate. This will be performed in the following sections, along with their association with interplanetary perturbations at their origin.

4.2 Recurrent GCR variations on LPF

In order to study the interplanetary disturbances that generated individual GCR flux recurrent variations, the LPF PD observations during subsequent BRs were compared between each other and to IMF and solar wind plasma parameters in the Geocentric solar ecliptic (GSE) reference frame. The GSE coordinate system has the origin at the Earth center, the x-axis points towards the Sun, the z-axis is perpendicular to the ecliptic plane and the y-axis completes the orthogonal triad. In order to reduce the long-term modulation effect on the GCR flux short-term variation analysis, percentage variations are computed with respect to the average count rate over each BR. In the top panel of Figure 4.3, cosmic-ray flux variations measured by LPF during the BR 2491 (from March 4, 2016 through March 31, 2016) present four recurrent depressions starting on March 5, 12, 23, and 29, respectively, which are also observed in the successive BRs 2492 and 2493. The small dips on March 11-12 and 19-20 along with the small increase on March 16-17 are transient < 2 day variations, as they are not present in the following BR 2492. The solar wind plasma speed is displayed in the second panel of Figure 4.3. The IMF x-component in the GSE reference frame is shown in the third panel, with the HCS crossing line overlaid, and the IMF intensity in the fourth panel. Solar wind and magnetic field data are taken from instruments on board the ACE mission at L1. The GCR flux

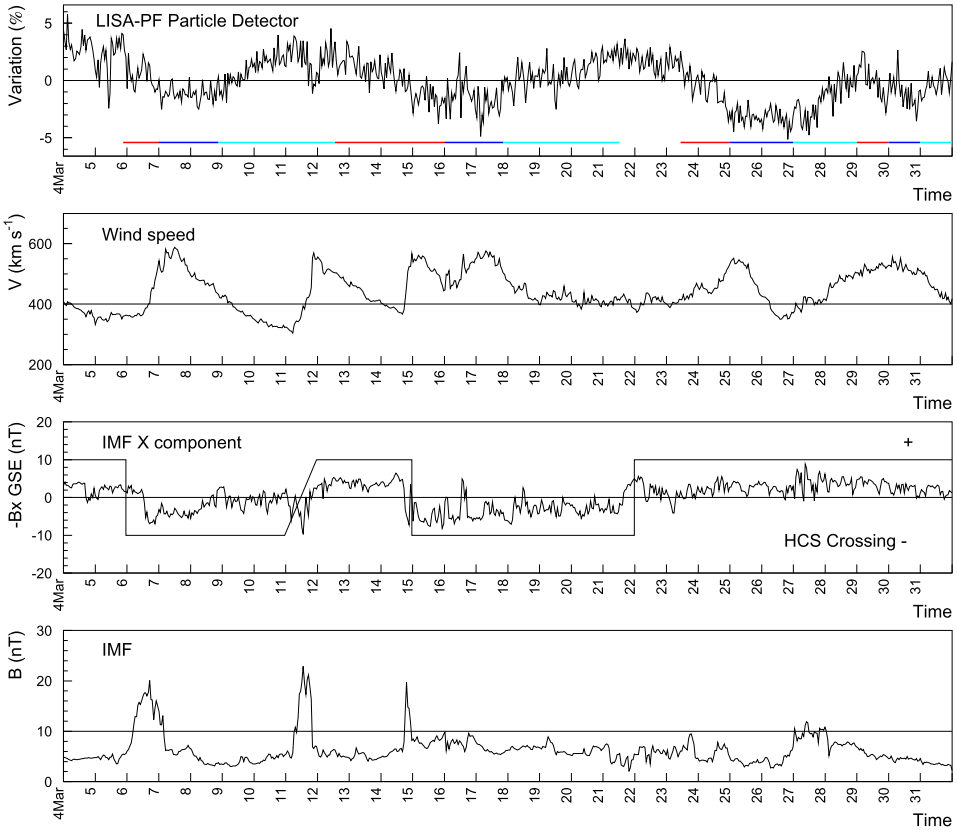

Figure 4.3 LPF PD count rate variations during the BR 2491 (March 4-31, 2016) (first panel). Solar wind speed (second panel), IMF negative x-component in a GSE coordinate system, $-B_x$ (third panel), and IMF intensity (fourth panel) contemporaneous measurements are also shown. In the third panel the continuous line indicates HCS crossings and the sector daily polarity (positive and negative polarities were set respectively to $+10$ and -10 arbitrarily in the plot). Periods of time during which the solar wind speed V, and the magnetic field B, intensity remain below and above 400 km s^{-1} and 10 nT, respectively, are shown in the second and fourth panels. Decrease, plateau, and recovery periods of each GCR depression are represented by red, blue, and cyan lines, respectively, in the first panel (Armano et al., 2018).

depressions appear associated with those periods of time during which the solar wind plasma speed $V > 400$ km s^{-1} and/or the IMF intensity $B > 10$ nT (second and fourth panels in Figure 4.3). A plateau is observed during both U- shaped symmetric and asymmetric depressions

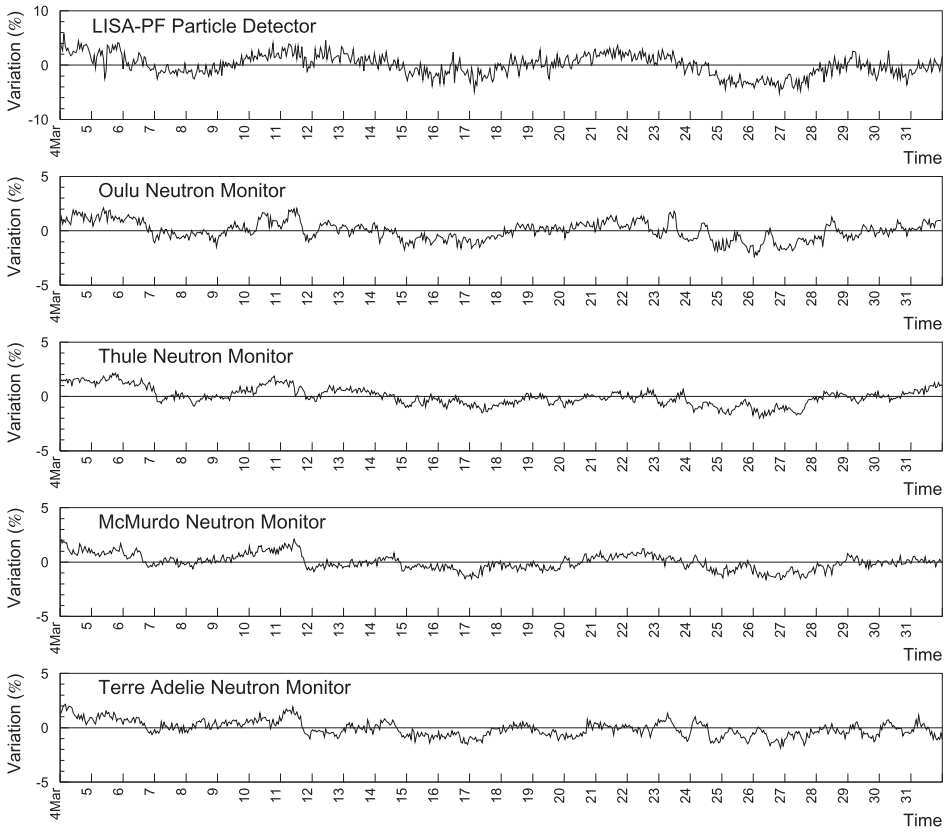

Figure 4.4 Comparison of LPF PD count rate variations with contemporaneous, analogous measurements of polar neutron monitors during the BR 2491 (March 4-31, 2016; Armano et al., 2018).

and appears correlated with the period of time the solar wind velocity remains above 400 km s^{-1}. A typical asymmetric recurrent depression is that appearing in the top panel of Figure 4.3 starting on March 5, 2016 with 2 day decrease, $\sim$ 1.5 day plateau and 3.5 day recovery periods. In the same figure, a symmetric, U- shaped depression starts on March 23 with decrease, plateau and recovery phases lasting about two days each. Decrease, plateau, and recovery phases for each depression during the BR 2491 are shown in colors in the top panel of Figure 4.3.

In order to investigate the energy dependence of these recurrent GCR flux variations, LPF observations are compared to contemporaneous similar measurements gathered by NMs placed at different geographic latitudes on the Earth. As an example, in Figure 4.4 LPF data for the BR 2491 are compared to Oulu, Thule, Mc Murdo and Terre Adelie NMs.

Table 4.2. NM stations, locations and characteristics.

Station	Location	Vertical cutoff rigidity (GV)	Effective energy (GeV)
Thule	North Pole	0.3	11-12
Terre Adelie	South Pole	0.0	11-12
Mc Murdo	South Pole	0.3	11-12
Oulu	Finland	0.8	12
Rome	Italy	6.3	17
Mexico	Mexico	8.2	20

NM data are hourly averaged and the percentage variations are computed with respect to the average count rate value observed over the same BR. Locations, vertical cutoff rigidities, and effective energies for all NM stations considered in this work are reported in Table 4.2. This comparison indicates that while the GCR percentage variations observed with LPF above 70 MeV n^{-1} are on average of 5%. The same goes down to about 3% above effective energies of 11-12 GeV in near-polar stations and to $\leqslant 2\%$ at higher effective energies at increasing latitudes (e.g. Rome not shown in the figure).

GCR flux recurrent variations identified over the LPF data taking period appear to be associated with the passage of high-speed solar wind streams and/or CIRs in L1. A complete list of recurrent GCR flux variations and associated interplanetary disturbances is reported in Table 4.3.

In order to quantify the quasi-periodic oscillations related to the occurrence of recurrent variations a periodicity analysis was carried out. Since the LPF PD count rate appears to be non-stationary in time, the analysis is carried out by using an advanced technique as follows.

4.2.1 The Hilbert-Huang transform

The HHT is a data analysis technique aimed to provide an alternative view of the usual time-frequency-energy paradigm dealing with non-stationarity and non-linearity (Huang, 2014). For instance, the Fourier analysis like the fast Fourier transform is widely used in the data analysis assuming that the dataset is linear and stationary, but this is not valid in general. Conversely, the Wavelet transform is effective in analyzing non-stationary datasets, but it is also fair poor when non-linearity is introduced. In most real systems data are most likely to be both

Table 4.3. Occurrence and characteristics of the GCR flux recurrent depressions observed during the LPF mission.

Date	Onset Time	Decrease Days	Plateau Days	Recovery Days	Amp. %	IP disturbance
Feb 26, 2016	16.00 UT	2.5	1.0	3.2	7.0	CHSS
Mar 5, 2016	21.00 UT	2.0	1.0	3.5	4.9	ICME+CHSS
Mar 12, 2016	00.00 UT	3.5	2.0	3.5	5.3	CHSS
Mar 23, 2016	11.00 UT	2.0	2.0	2.0	6.0	CHSS
Mar 29, 2016	03.00 UT	1.0	1.0	4.0	3.4	CHSS
Apr 20, 2016	12.00 UT	3.0	2.0	4.5	7.1	CHSS
May 1, 2016	11.00 UT	1.5	1.0	2.0	2.8	CHSS
May 6, 2016	00.00 UT	2.8	0.0	6.5	4.7	CHSS
May 15, 2016	12.00 UT	4.0	1.0	1.0	7.2	CIR
May 29, 2016	13.00UT	1.5	0.0	5.0	3.0	CHSS
Jun 5, 2016	04.00 UT	1.0	1.0	4.0	5.1	CIR
Jun 12, 2016	07.00 UT	3.5	0.0	10.0	8.4	CHSS
Jul 7, 2016	00.00 UT	6.0	1.0	3.0	11.9	CIR
Aug 5, 2016	21.00 UT	5.0	4.0	15.0	6.8	CHSS
Aug 29, 2016	21.00 UT	6.0	2.0	19.0	8.6	CIR
Sep 26, 2016	12.00 UT	3.0	2.0	8.0	6.9	CIR
Oct 11, 2016	15.00 UT	2.0	0.0	2.0	5.0	HCS+ICME
Oct 16, 2016	15.00 UT	1.0	0.0	5.5	2.8	CHSS
Oct 23, 2016	00.00 UT	6.0	2.0	8.0	7.5	CHSS
Nov 12, 2016	00.00 UT	1.0	3.0	4.0	1.6	CIR
Nov 20, 2016	16.00 UT	5.0	3.5	5.0	8.1	HCS+CHSS
Dec 7, 2016	12.00 UT	2.0	3.5	4.5	2.8	CIR
Dec 17, 2016	19.00 UT	8.5	1.0	4.5	10.9	CHSS
Jan 5, 2017	03.00 UT	1.0	2.0	6.5	3.0	CIR
Jan 14, 2017	15.00 UT	5.0	2.0	2.0	6.3	HCS + CHSS
Jan 25, 2017	11.00 UT	2.5	0.0	3.0	3.4	HCS + CHSS
Jan 30, 2017	16.00 UT	3.0	0.0	10.5	4.4	CIR
Feb 16, 2017	23.00 UT	1.0	1.0	2.5	3.1	CIR
Feb 23, 2017	10.00 UT	1.0	0.0	3.0	1.8	CIR
Mar 1, 2017	05.00 UT	2.0	0.0	5.5	3.9	CIR
Mar 21, 2017	00.00 UT	2.0	1.0	2.0	4.4	CIR
Mar 27, 2017	00.00 UT	8.0	3.5	5.5	6.9	CIR
Apr 18, 2017	09.00 UT	1.5	0.5	1.0	3.4	CIR
Apr 21, 2017	11.00 UT	3.0	2.0	4.5	7.8	CIR
May 15, 2017	08.00 UT	1.5	1.0	2.0	3.8	CIR
May 19, 2017	10.00 UT	1.5	1.0	5.5	2.5	HCS+CHSS
Jun 12, 2017	16.00 UT	6.0	2.0	2.5	3.4	CHSS
Jun 24, 2017	14.00 UT	4.0	1.0	2.0	5.3	CIR

Note. — Interplanetary structures associated with the depressions are indicated (CIR: corotating interaction region; CHSS: corotating high-speed solar wind streams; HCS: crossing of the heliospheric current sheet).

non-linear and non-stationary. The HHT is an empirically based data-analysis method with an adaptive basis of expansion that can produce a meaningful representation of the physical properties of a general dataset. The first step of the HHT consists on the definition of the basis for the decomposition and the algorithm used to achieve this task is the empirical mode decomposition (EMD). The second step of the HHT is the Hilbert spectral analysis (HSA) that allows to compute the Hilbert spectrum using the time-dependent amplitudes and frequencies contained in the dataset components obtained through the EMD. A brief theoretical introduction of the HHT and its application to the LPF dataset are provided in this section.

Empirical mode decomposition

The EMD is a useful method to study non-linear and non-stationary datasets. This technique allows to separate complex datasets into a finite, and often small, number of components called *intrinsic mode functions*. The intrinsic mode functions derived from the data represent the complete and almost orthogonal basis of the expansion. Since the basis is built from an iterative/data-driven algorithm, no *a priori* analytic expression is given. Therefore, the decomposition is based on the local characteristic time scale of the data and it can be used to investigate non-linear and non-stationary processes. An intrinsic mode function must satisfy two conditions: 1) in the whole dataset, the number of maxima and minima and the number of zero crossings must be either equal or differ by one at most; 2) at any point, the mean value of the envelopes defined by local maxima and local minima is zero (Huang et al., 1998). The first condition avoids unwanted oscillations due to asymmetric wave-forms by forcing oscillations to be quasi-symmetric around zero. The second condition is a necessary approximation to avoid the definition of a local averaging time scale. Indeed, a more rigorous way to define the intrinsic mode function should comprehend the requirement of zero local mean, instead of the zero mean of the envelopes. For non-stationary datasets, the definition of the local mean implies to determine a local time scale that must be assigned in each individual case.

The EMD describes all the signal oscillations at a very local level and is based on the following assumptions:

1. the signal has at least two extrema (one maximum and one minimum),

2. the characteristic time scale is defined by the time lapse between

the extrema.

For a given signal $X(t)$, using the definition of intrinsic mode function the EMD algorithm works as summarized in the following:

1) all extrema of the signal $X(t)$ are identified,

2) a cubic spline interpolation between the minima (maxima) to build the envelop $e_{\min}$ ($e_{\max}$) is performed,

3) the mean $m_1 = (e_{\min} + e_{\max})/2$ is computed,

4) the high-frequency part $h_1 = X(t) - m_1$ is calculated,

5) steps 1) - 4) are iterated with $X(t) = m_1$, until m_1 does not present any further oscillation.

Since m_1 is the mean of the maximum and minimum envelopes, the difference between the signal and m_1, i.e. h_1, should be an intrinsic mode function. In order to avoid artificial effects induced by the algorithm, a refinement is needed and then the sifting procedure is performed. The sifting procedure consists in the iteration of steps 1) to 4) on the signal h_1 until it can be considered as zero-mean according to some stopping criterion (see Section 4.2.1 for details). This procedure allows to eliminate riding waves and to make the wave-profiles more symmetric. In general, the sifting procedure has to be repeated several times. In the second sifting procedure, h_1 is treated as the signal, indicating the mean over the maxima and minima envelops as m_{11}, from step 4) is set

$$h_1 - m_{11} = h_{11}.$$

This procedure is repeated until all the local maxima are positive, all the local minima are negative and the resultant signal is approximately symmetric with respect to zero. Assuming that after k iterations the stopping criterion is fulfilled, at the end of the sifting procedure is obtained

$$h_{1(k-1)} - m_{1k} = h_{1k} = c_1,$$

where the function c_1 is the first intrinsic mode function associated with the signal $X(t)$. The function c_1 contains the highest frequency component of the initial signal and by defining the residue $r_1 = X(t) - c_1$, the first component c_1 is now separated from the rest of the dataset. Since the residue r_1 still contains information of longer period components, it is treated as a new signal and the sifting procedure described above is

applied again. Repeating the same procedure on all the subsequent n residues, the result is

$$r_1 - c_2 = r_2, \ldots, r_{n-1} - c_n = r_n.$$

The number of extrema decreases from one residue to the next, and the whole decomposition is guaranteed to stop with a finite number of modes. At the end, the residue r_n is a function that does not complete any oscillation in the considered time interval (i.e. is a monotonic function or a function with only one maximum and one minimum) and represents the trend of the original signal.

EMD stopping criteria

The extraction of an intrinsic mode function is complete only after the application of the sifting procedure. This procedure must satisfy two conditions: 1) the number of extrema and the number of zero-crossings must differ at most by one, 2) the mean between the $e_{\min}$ and $e_{\max}$ envelopes must be close to zero according to some criterion. The evaluation of how small is the envelope mean must be done in comparison with the amplitude of each individual mode. For instance, the choice of a too low threshold for terminating the sifting procedure leads to drawbacks as the over-decomposition with the result that too many iterations are performed and many modes are separated, although they have approximately the same mean period. Conversely, by setting too high thresholds, modes at different time scales could not be properly separated.

The first stopping criterion introduced in Huang et al. (1998) lies on the evaluation of the standard deviation between each pair of subsequent sifting iterations defined as follows

$$SD = \sum_{t=0}^{T} \left[\frac{|h_{i(k-1)}(t) - h_{ik}(t)|^2}{h^2_{i(k-1)}(t)} \right]$$

where i denotes the intrinsic mode function index, T is the length of the time series and k the number of sifting iterations. The threshold suggested in their work is 0.2 or 0.3, below which the envelopes are considered to have approximately a zero-mean and the sifting procedure is stopped. Conversely, the stopping criterion used in the following is based on two thresholds, θ_1 and θ_2 and was firstly suggested by Rilling et al. (2003). This criterion aims to guarantee overall small fluctuations

in the mean between the two envelopes by taking into account also local large excursions of the signal. Two new functions are defined and evaluated: the mode amplitude, $a(t) = (e_{\max}(t) - e_{\min}(t))/2$, and the evaluation function, $\sigma(t) = |m(t)/a(t)|$. The sifting procedure is iterated until $\sigma(t) < \theta_1$ for an assigned fraction $(1 - \alpha)$ of the total dataset time interval and $\sigma(t) < \theta_2$ for the remaining fraction. The default values to set this stopping criterion are $\alpha = 0.05$, $\theta_1 = 0.05$ and $\theta_2 = 10\theta_1$.

Statistical significance of the intrinsic mode functions

In order to establish a criterion to estimate the statistical significance of intrinsic mode functions, a detailed study on the Gaussian white noise was proposed by Wu and Huang (2004) using the EMD technique. For the lack of an *a priori* analytical expression for the intrinsic mode functions, the study was carried out empirically. Performing the EMD analysis on a Gaussian white noise signal, the relation between the energy E_i associated with intrinsic mode functions and their mean periods $\bar{\tau}_i$ is found to be

$$\ln E_i + \ln \bar{\tau}_i = \text{const.}$$

The quantification of the energy spread function is also known from the study of the probability distribution function (PDF) of each individual intrinsic mode function that can be expressed as

$$\ln E_i = -\ln \bar{\tau}_i \pm k\sqrt{\frac{2}{N}} \exp\left(\frac{\ln \bar{\tau}_i}{2}\right) \tag{4.1}$$

where N is the number of data points of the considered signal and k is a constant determined by percentiles of a standard normal distribution (e.g. k equals -2.326, -0.675, 0.0, 0.675 and 2.326 for the 1st, 25th, 50th, 75th and 99th percentiles, respectively). A comparison between the intrinsic mode function energy as a function of the mean period after the application of the EMD on a general signal, compared to that of Gaussian white noise, allows to recognize and separate the noise component from the genuine signal.

Hilbert spectral analysis

The usual paradigm of data analysis is based on the definition of several components with constant frequencies and amplitudes representing the basis of the decomposition. A more general way to express and investigate the non-stationarity and non-linearity present in real datasets is

to define the instantaneous frequency and the instantaneous amplitude. For a function $x(t)$, representing a real dataset, the Hilbert transform $y(t)$ is defined as:

$$y(t) = \frac{1}{\pi} P \int_{-\infty}^{+\infty} \frac{x(\tau)}{t-\tau} d\tau, \tag{4.2}$$

where P is the Cauchy principal value of the integral that contains a singularity on the real domain. With the Hilbert transform $y(t)$ of the function $x(t)$, we can introduce the analytic function $z(t)$ that contains the function $x(t)$ as real part and the function $y(t)$ as imaginary part

$$z(t) = x(t) + iy(t) = a(t)e^{i\theta(t)}. \tag{4.3}$$

The function $a(t)$ represents the instantaneous amplitude and $\theta(t)$ the instantaneous phase. These functions are related to the $x(t)$ and $y(t)$ initial functions by the straightforward relations

$$a(t) = (x^2 + y^2)^{1/2} \qquad \theta(t) = \tan^{-1} \frac{y}{x}. \tag{4.4}$$

Starting from the definition of instantaneous phase function, the instantaneous frequency can be defined as

$$\omega(t) = \frac{d\theta(t)}{dt}. \tag{4.5}$$

The function that express the time-frequency dependence of the amplitude, or the energy, of the dataset is called Hilbert spectrum $H(\omega, t)$. The counterpart of the Fourier spectrum can be now computed by integrating the function $H(\omega, t)$ over the time domain $[0, T]$ where the dataset is defined. This time-integral is called Hilbert marginal spectrum

$$h(\omega) = \int_0^T H(\omega, t) dt. \tag{4.6}$$

and represents the total amplitude, or energy, contribution for each frequency value.

After performing the HHT, the original data can be expressed as the real part of the equation (4.3) as

$$x(t) = \Re \left\{ \sum_{j=1}^{n} a_j(t) \exp \left[i \int \omega_j(t) dt \right] \right\}. \tag{4.7}$$

Table 4.4. Mean oscillation periods of the intrinsic mode functions from the EMD analysis on the LPF GCR data with standard deviation.

mode #	mean period (days)	mode #	mean period (days)
1	0.1±0.1	6	7.0±2.8
2	0.2±0.1	7	13.2±2.8
3	0.4±0.2	8	27.9±3.7
4	1.0±0.4	9	90.3±21.5
5	2.3±0.8	10	112.5±18.8

This expression represents a generalization of the usual Fourier decomposition since it comes in the same form except for the time dependence of both amplitude and frequency. The residue r_n of the EMD is not included in this discussion because it is either a monotonic function, or a constant. Although the Hilbert transform can treat the monotonic trend as part of a longer oscillation, the energy involved in the residual trend represents a mean offset that can be overpowering. Considering the uncertainty of the longer trend and the interesting information contained in the other more clear and less energetic components, the residue should be left out.

4.2.2 Discussion of the HTT results

The LPF PD data have been decomposed through the EMD technique, described in Section 4.2.1, in ten intrinsic mode functions that are illustrated in Figure 4.5. It is worth noting that intrinsic mode functions are empirical and present a time dependence in both amplitude and frequency. Summing up all the intrinsic mode functions, along with the residue, the original time series can be retrieved. It is found that the difference between the original and the reconstructed signal is negligible (about 10^{-12} in amplitude), proving the property of completeness of the EMD algorithm.

In Table 4.4 it is reported the mean oscillation period of each mode present in the LPF GCR data. In particular, those of intrinsic mode functions 6-8 are close to periodicities of 27, 13.5 and 9 days, related to the Sun rotation and higher harmonics, which are possibly associated with the recurrence of one or more interplanetary disturbances. Mean periods have been computed using the autocorrelation function of each

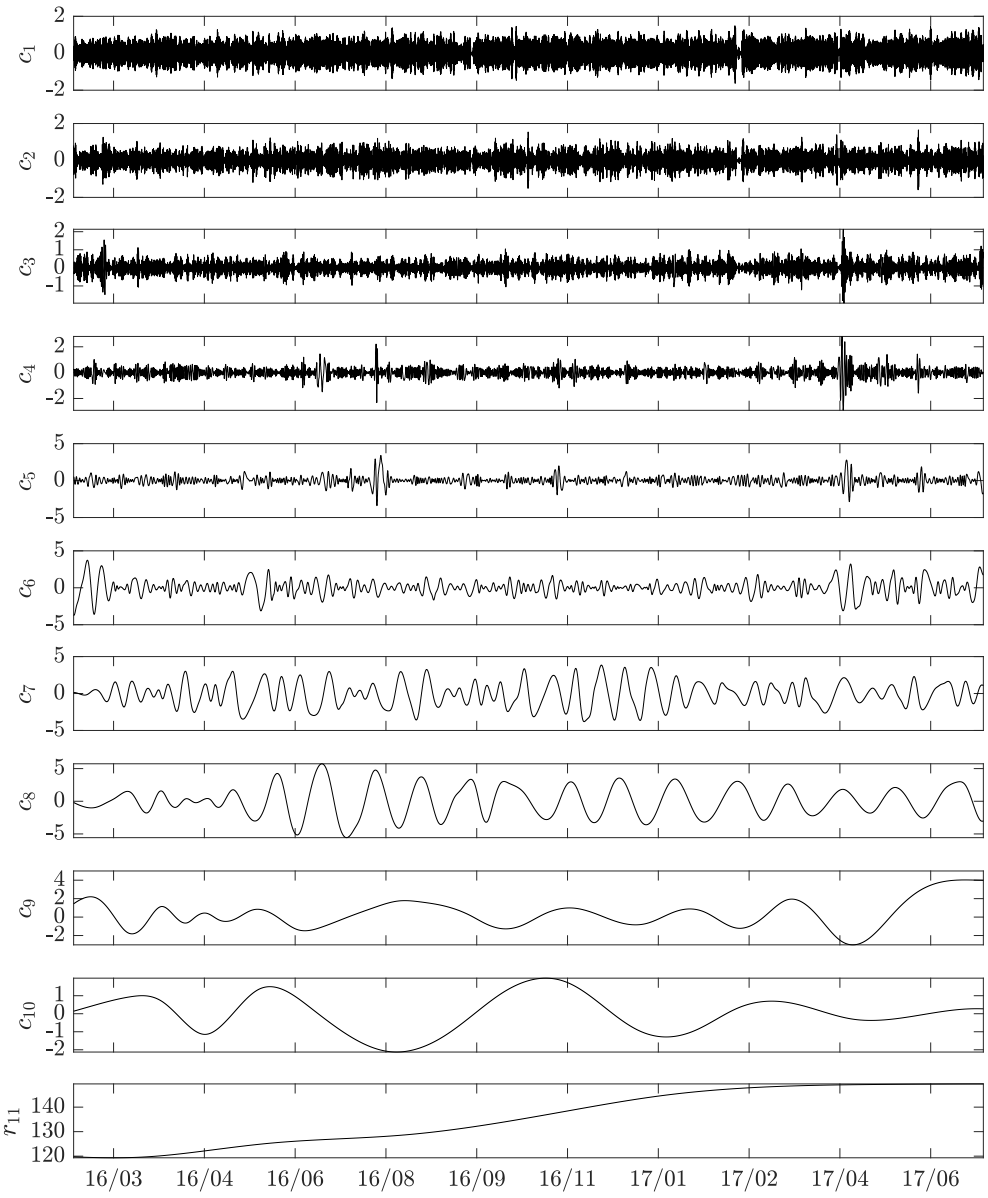

Figure 4.5 Intrinsic mode functions and residue from the EMD of the LPF PD dataset (time label format is yy/mm).

mode to find the location of the maxima and to obtain the average duration between them. The Wu and Huang (2004) method has been applied to quantify the statistical significance of intrinsic mode functions with respect to the Gaussian white noise. In Figure 4.6 (left panel) it can be clearly observed that only intrinsic mode functions 4-11 lie above the

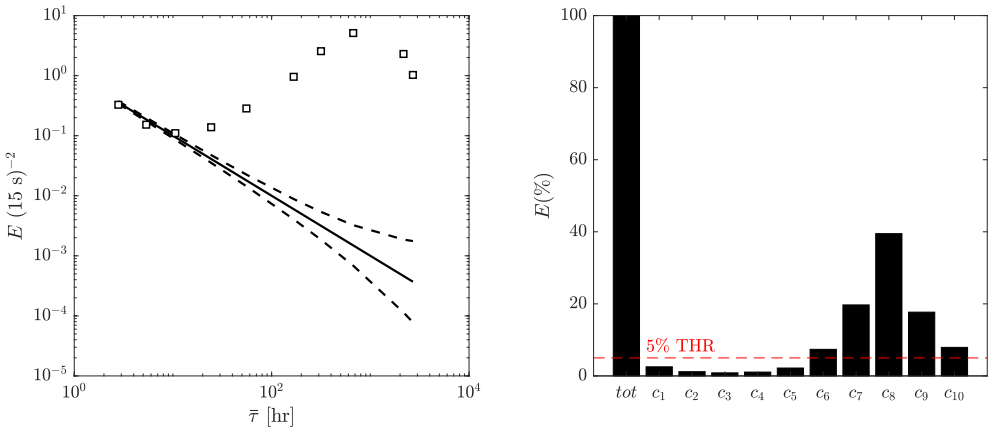

Figure 4.6 Left: Energy associated with the intrinsic mode functions as a function of their mean period. The solid line is the energy-period dependence for the Gaussian white noise and the dashed line are the first and 99th percentiles calculated from equation (4.1). Right: Percentage energy level of each intrinsic mode function with respect to the total energy of the signal (first column of the histogram). The red dashed line represent the 5% threshold.

99% white noise spread line computed from equation (4.1).

The energy associated with each intrinsic mode function has been calculated as

$$E_i = \frac{1}{T}\int_0^T |c_i(t)|^2 dt \tag{4.8}$$

in order to understand which modes give higher contribution to the original dataset. The obtained energies, normalized to the whole energy of the signal, are shown in Figure 4.6 (right panel). By choosing a threshold of 5% (the confidence level), those intrinsic mode functions whose energies exceed the threshold are considered to contain a physical information, whereas all the remaining ones are more likely to represent noise (Klionski et al., 2008). It is found that the energy budget of the intrinsic mode functions 6-10 that exceed the 5% threshold is more than the 90% of the whole dataset, hence these functions can be used to reconstruct a denoised signal. The reconstruction is shown in Figure 4.7 (black line) and compared with the GCR original time series (gray line). This figure shows that the EMD technique allows to accurately capture all the time variations without noise and high frequency fluctuations.

The residue of the decomposition, representing the long-term GCR trend, is reported in Figure 4.8 (black line), along with the 13-month

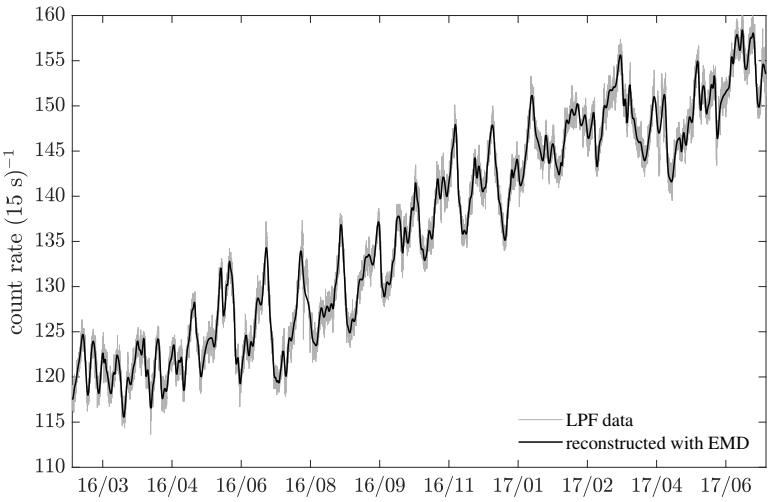

Figure 4.7 LPF GCR dataset (gray dashed line) compared to the denoised signal obtained by summing up intrinsic mode functions 6-11 (black solid line).

smoothed monthly total sunspot number[1] as a proxy of the solar activity. We recall that the LPF mission elapsed time extends over a part of the decreasing phase of the solar cycle 24. Since interplanetary disturbances, acting as barriers on the GCR propagation, are gradually reduced going towards the solar minimum as well as the global IMF intensity, the long-term trend of GCRs shows a gradual increase. This well-known anti-correlation is apparent in Figure 4.8 as expected.

In order to understand the physical phenomena underlying the observed GCR variations, the instantaneous amplitudes and frequencies of the intrinsic mode functions have been obtained with the HSA, as described in section 4.2.1. This procedure allows for investigating the complex time-frequency dependence of the amplitude (or the energy) associated with each intrinsic mode function. First, by studying the statistical properties of instantaneous frequencies (hereafter indicated with f) related to the intrinsic mode functions, it can be shown wheter or not the EMD properly separated different modes. Indeed, when the PDFs of different instantaneous frequencies show an important overlap, they may describe the same time scale. In such cases intrinsic mode functions

[1]Sunspot number data are taken from http://sidc.be/silso/datafiles

Table 4.5. Values of the overlap areas between subsequent instantaneous frequency PDFs.

PDFs	Area	PDFs	Area
$p(f_1) \cap p(f_2)$	0.38	$p(f_6) \cap p(f_7)$	0.30
$p(f_2) \cap p(f_3)$	0.35	$p(f_7) \cap p(f_8)$	0.30
$p(f_3) \cap p(f_4)$	0.36	$p(f_8) \cap p(f_9)$	0.16
$p(f_4) \cap p(f_5)$	0.37	$p(f_9) \cap p(f_{10})$	0.44
$p(f_5) \cap p(f_6)$	0.32		

should be summed up to produce a unique mode as they can be related to the same physical process. The PDFs of the instantaneous frequencies of modes 1-10 (blue area) are displayed in panel from top to bottom of Figure 4.9, respectively. Moreover, each plot depicts the instantaneous frequency PDF of the successive $i + 1$ intrinsic mode function (red line), to show the overlap with the i^{th} mode.

Values of the overlap areas between subsequent instantaneous frequency PDFs are reported in Table 4.5. As the 50% value is never exceeded, the modes have been considered to be independent, each one of them representing a different scale of variability contained in the original dataset.

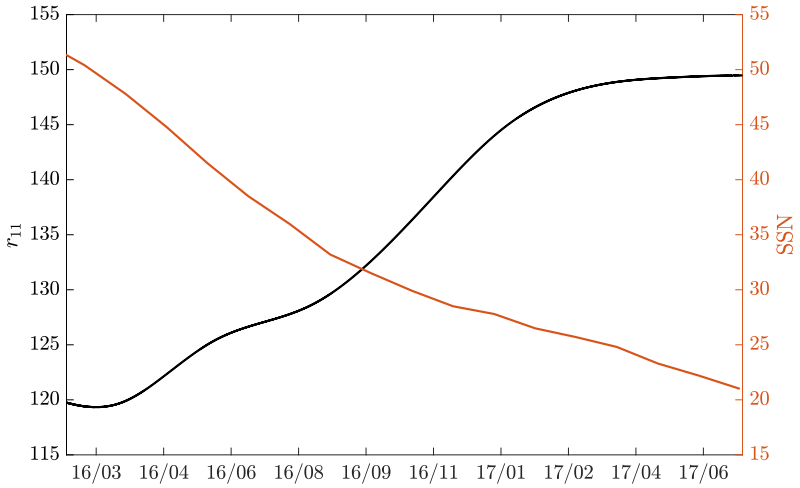

Figure 4.8 Comparison between the residue of the EMD and the 13-month smoothed monthly total sunspot number.

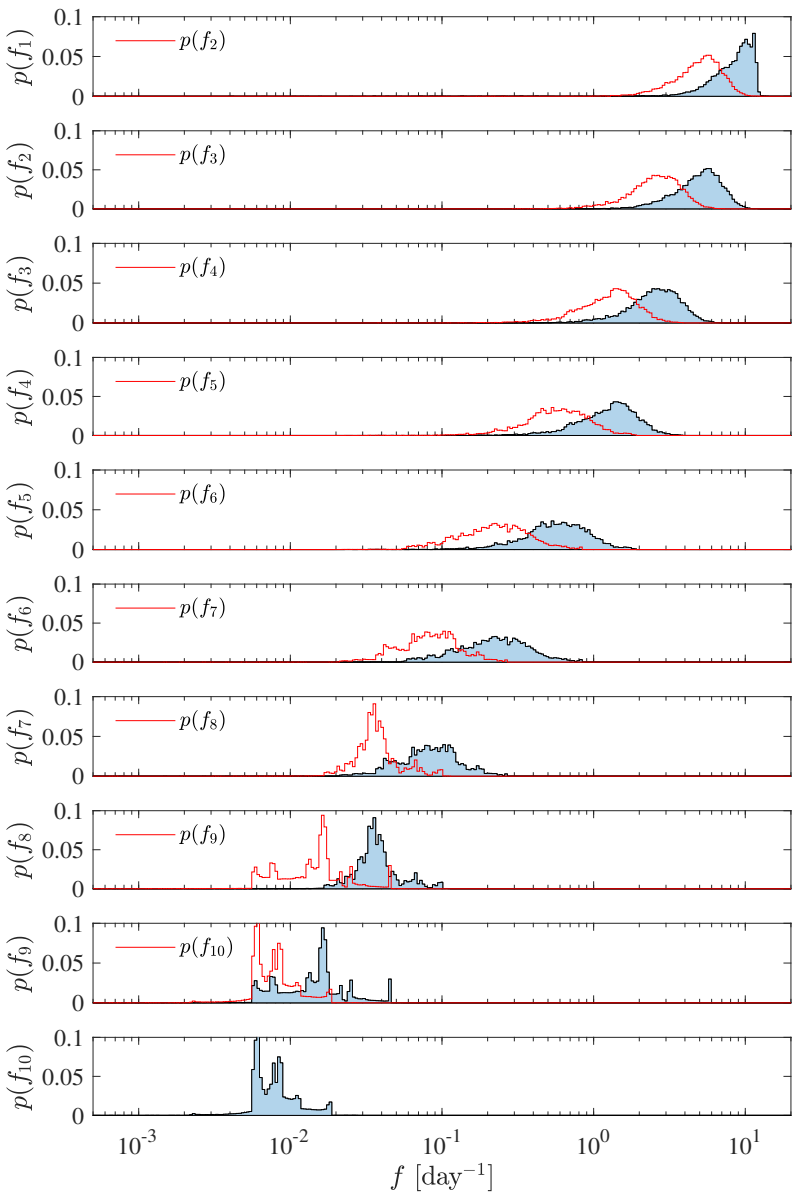

Figure 4.9 PDF $p(f)$ of the instantaneous frequencies of the LPF dataset.

The Hilbert spectrum computed on the LPD PD dataset is shown in Figure 4.10, where time is given in days and frequency in day^{-1}. The total LPF mission elapsed time is of 500 days and the time interval in the color map is divided in BRs by vertical dotted lines. BR number labels are reported in the top of the plot. The horizontal dashed lines correspond to frequencies associated with the about 27 day solar rotation and 13.5 and

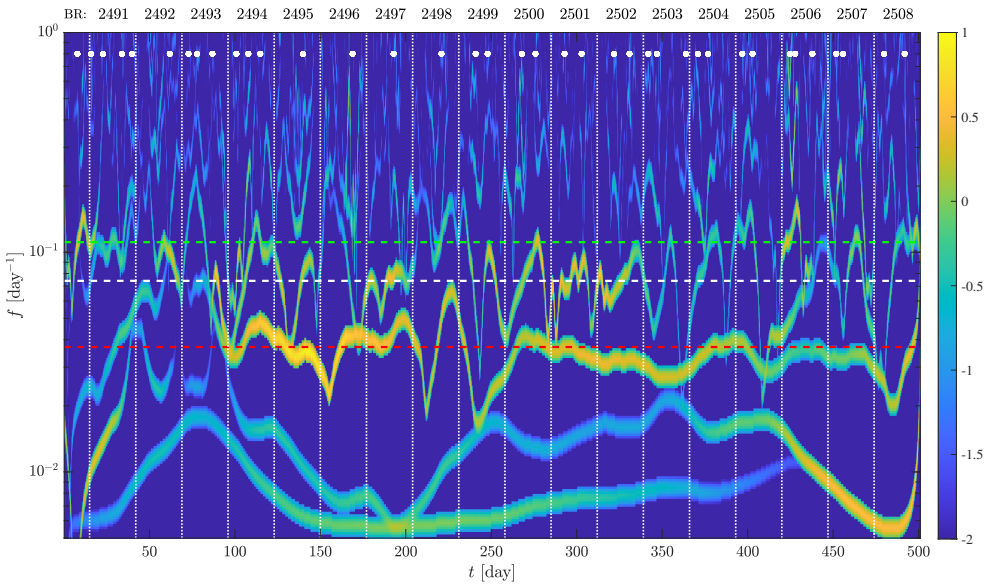

Figure 4.10 Time-frequency diagram of the Hilbert spectrum for the LPF dataset. Horizontal dashed lines represents the typical frequencies related to the solar rotation period: 27 days (red), 13.5 days (white) and 9 days (green). The white vertical dotted lines mark the edges of the BRs while dots indicate the passage of recurrent disturbances according to Table 4.3. The color map indicates the logarithm of the square amplitude of each intrinsic mode function as a function of frequency and time.

9 days higher harmonics. In fact, the region of the spectrum where the high energy is accumulated is close to these three frequencies (1/9 day^{-1} green line, 1/13.5 day^{-1} white line, 1/27 day^{-1} red line). In order to interpret the information provided by the HSA it is useful to observe the number of recurrent events observed during subsequent BRs (see Table 4.3). On the top of Figure 4.10 the white dots indicate the presence of an interplanetary perturbation producing a recurrent variation. The high energy part of the spectrum along the 27 day periodicity extends over the BRs 2495-2498, characterized by one short-term recurrent modulation per each BR. This is consistent with the passage of one perturbation corotating with the Sun producing a 27 day periodicity in GCR data for several BRs. During BRs 2499-2502 a high energy is observed also along the 13.5 day periodicity line. Indeed the number of corotating perturbations observed during this period of time is two for each BR. Other periods of time where more than two corotating perturbations are present (e.g., from BR 2491 to 2494, BR 2503 and BR 2506), a more

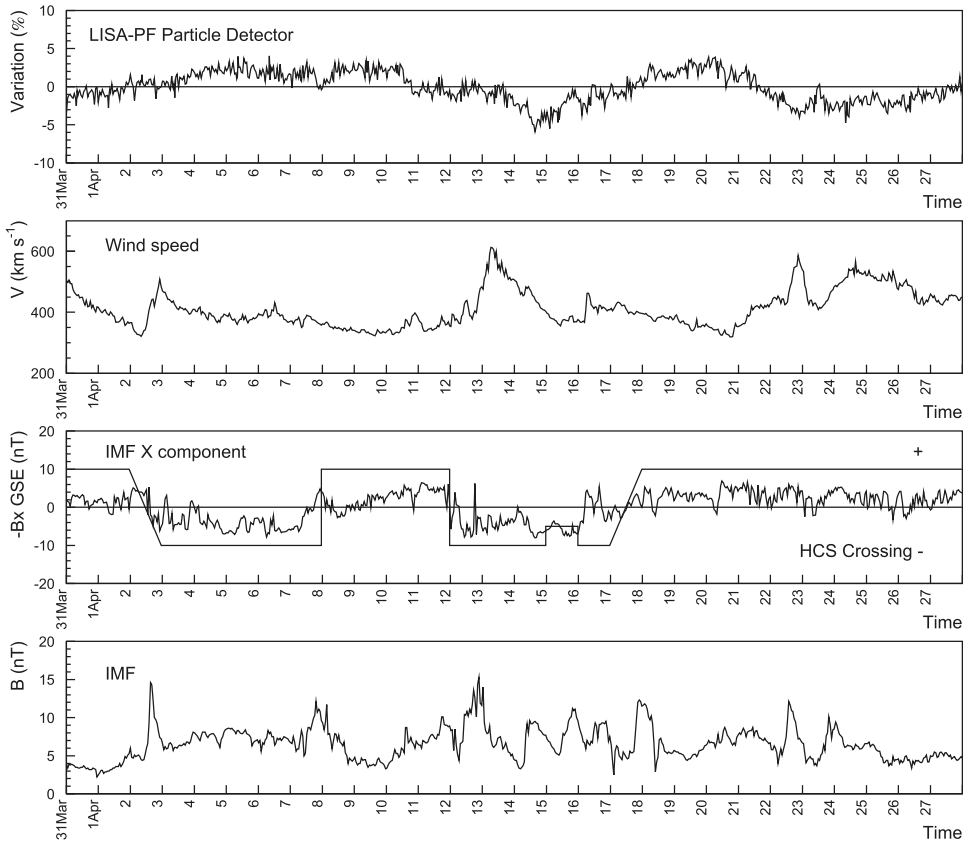

Figure 4.11 Same as Figure 4.3 for the BR 2492 (March 31-April 26, 2016; Armano et al., 2019).

complex pattern is observed with energy peaks also on the 1/9 day^{-1} frequency.

4.3 Transient GCR variations on LPF

Twenty-three non-recurrent GCR flux variations were identified, having duration < 2 day, of which six enhancements and seventeen depressions. As an example, data gathered during the BR 2492 are reported in Figure 4.11. During this BR, the GCR count rate presents a small depression between April 7-8, 2016 and two small peaks on April 15, 2016 and April 23, 2016. A comparison of the LPF data with those gathered with polar NMs during the same BR 2492 in Figure 4.12 shows that the small GCR flux enhancement dated April 15 was observed in the most of the polar

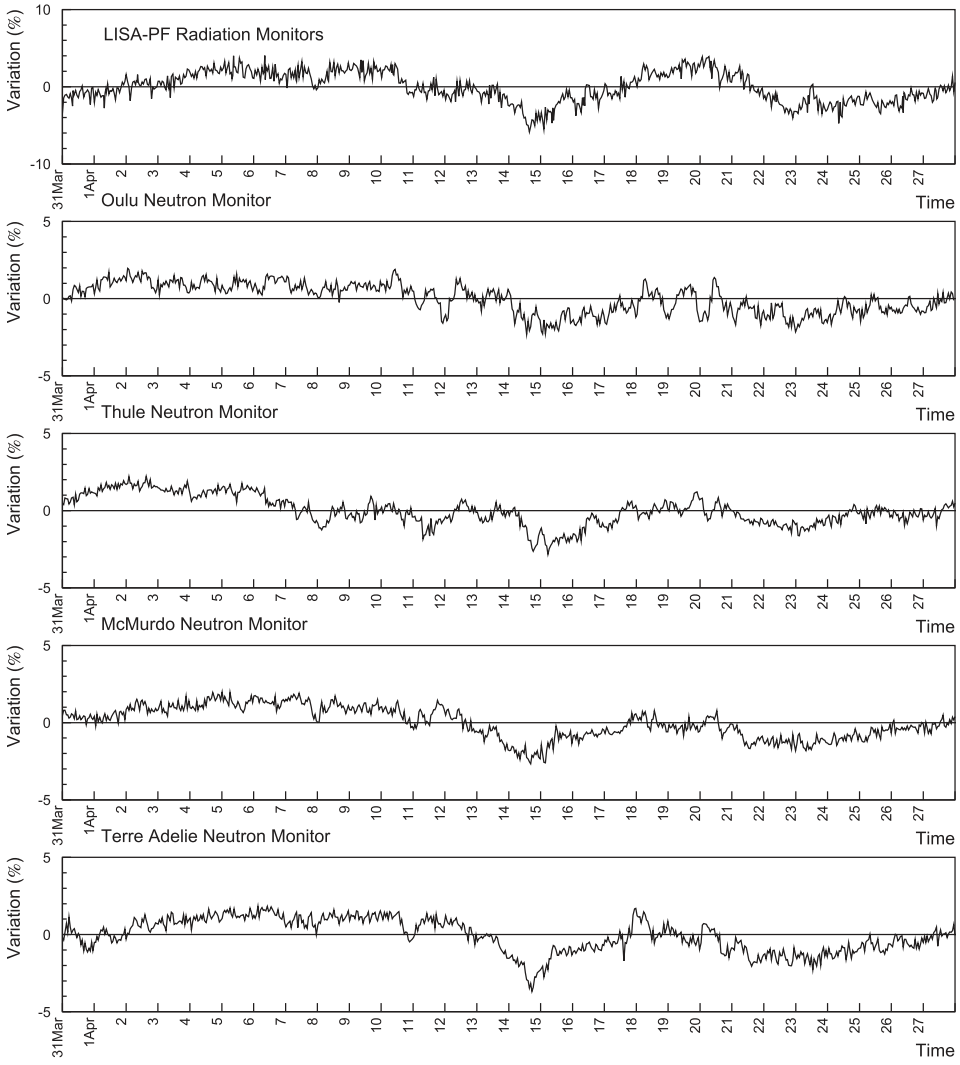

Figure 4.12 Same as Figure 4.4 for the BR 2492 (March 31-April 26, 2016; Armano et al., 2019).

NM measurements; similarly the depression dated April 7-8 is observed with Thule and McMurdo NMs (note that the LPF and the NM data are shown on different scales in this figure). Conversely, the April 23 enhancement is not observed in polar NMs. Interplanetary plasma (solar wind bulk speed, temperature, and proton density) and magnetic field parameters are studied to identify interplanetary structures associated with individual < 2 day GCR flux variations. In Table 4.6, as in Table 4.3, CHSSs observed during subsequent BRs and originating from

coronal holes are characterized by a solar wind speed > 400 km s^{-1}, low magnetic field and plasma density. CIRs are identified as regions of compressed plasma formed between the leading and trailing edges of CHSSs when they overtake slow solar wind. Magnetic barriers (MBs) indicate those regions close to high magnetic field enhancements observed between closely spaced CHSSs. Finally, enhancements of magnetic field in the slow solar wind are indicated with magnetic field enhancements (MFEs). It is found that the majority of small depressions in the GCR flux are caused by HCS crossings; only seldom their evolution was modulated by CHSSs and CIRs. These findings are different from those illustrated in Section 4.2 (see also Armano et al., 2018) for GCR flux depressions > 2 day generally associated with CIR and CHSS passages. Peaks with duration < 2 day appear to be associated with regions of compressed plasma between two CHSS (see, for instance, April 23-24, 2016 in Figure 4.11). Several processes may generate these small peaks in the GCR flux. The most plausible is that the lowest-energy GCRs (~ 70 MeV n^{-1}) are confined in region between two CHSSs, due to possible trapping and/or reflection from MBs. However, a change in the low-energy GCR spectrum slope between a flux recovery phase after a CHSS passage and a new GCR flux decrease due to the passage of a subsequent CHSS, may also resulting a peak feature in the integral flux. An increase of the > 70 MeV n^{-1} flux due to the acceleration at the shock of incoming CHSS does not appear plausible on the basis of the absence of small peak structures at the passage of isolated CHSS (e.g. see Figure 4.3). As a matter of fact, both models and observations indicate that the maximum energy of particles accelerated at CIR regions is about 20 MeV (McDonald et al., 1976; Tsurutani et al., 1987; Giacalone et al., 2002; Richardson, 2004; Laurenza et al., 2015).

4.4 Forbush decreases observed on board LPF

Three FDs were observed with LPF on July 20, 2016 (Figure 4.13), August 2, 2016 (Figure 4.14) and May 27, 2017 (Figure 4.15). The passage

Table 4.6. Occurrence and characteristics of the GCR flux variations < 2 day observed with LPF.

Date	Onset Time	Duration (days)	Dip/Peak	Amplitude %	IP structure
March 11, 2016	7.44 UT	0.97	DIP	3.1	CIR+HCS
March 16, 2016	1.38 UT	0.84	PEAK	3.0	MB
March 19, 2016	9.21 UT	1.16	DIP	2.5	CHSS
April 7, 2016	16.31 UT	0.89	DIP	3.4	HCS
April 15, 2016	7.44 UT	0.75	PEAK	4.4	MB
April 23, 2016	1.13 UT	1.16	PEAK	3.0	MB
June 16, 2016	0.15 UT	1.74	PEAK	2.5	MB
June 21, 2016	23.11 UT	1.68	DIP	2.5	HCS
June 23, 2016	2.12 UT	1.95	DIP	2.5	CIR
June 25, 2016	6.55 UT	1.79	DIP	2.5	CHSS
June 30, 2016	7.19 UT	1.79	DIP	2.8	HCS
July 2, 2016	3.15 UT	2.00	DIP	2.8	MFE
July 4, 2016	8.57 UT	1.74	DIP	2.5	CHSS+HCS
August, 2016 9	00.30 UT	0.75	PEAK	4.4	MB
August, 2016 16	6.06 UT	1.79	DIP	2.5	HCS
September, 2016 15	22.43 UT	0.84	DIP	3.1	MFE
October, 2016 11	13.25 UT	0.95	DIP	2.5	CHSS
October, 2016 23	21.09 UT	0.95	DIP	3.8	HCS+CHSS
November, 2016 10	17.29 UT	1.16	DIP	3.8	CIR+HCS
January, 2017 14	12.52 UT	0.75	DIP	3.1	HCS
March 22, 2017	22.21 UT	1.05	PEAK	2.1	MB
May 5, 2017	12.17 UT	1.46	DIP	2.3	MFE
May 29, 2017	21.07 UT	1.53	DIP	2.4	CIR

Note. — Interplanetary structures associated with each GCR flux $<$ 2-day variation are indicated (CIR: corotating interaction region; CHSS: corotating high-speed solar wind streams; ICME: interplanetary coronal mass ejection (http://www.srl.caltech.edu/ACE/ASC/DATA/level3/icmetable2.htm); S: shock; MC: magnetic cloud; HCS: crossing of the heliospheric current sheet; MFE: magnetic field enhancement in the slow solar wind; MB: magnetic barrier). IMF, solar wind plasma data and near-earth ICME passages were gathered from the websites https://cdaweb.sci.gsfc.nasa.gov/index.html and http://www.srl.caltech.edu/ACE/ASC/DATA/level3/icmetable2.htm. HCS crossings are reported in http://omniweb.sci.gsfc.nasa.gov./html/polarity/polarity_tab.html.

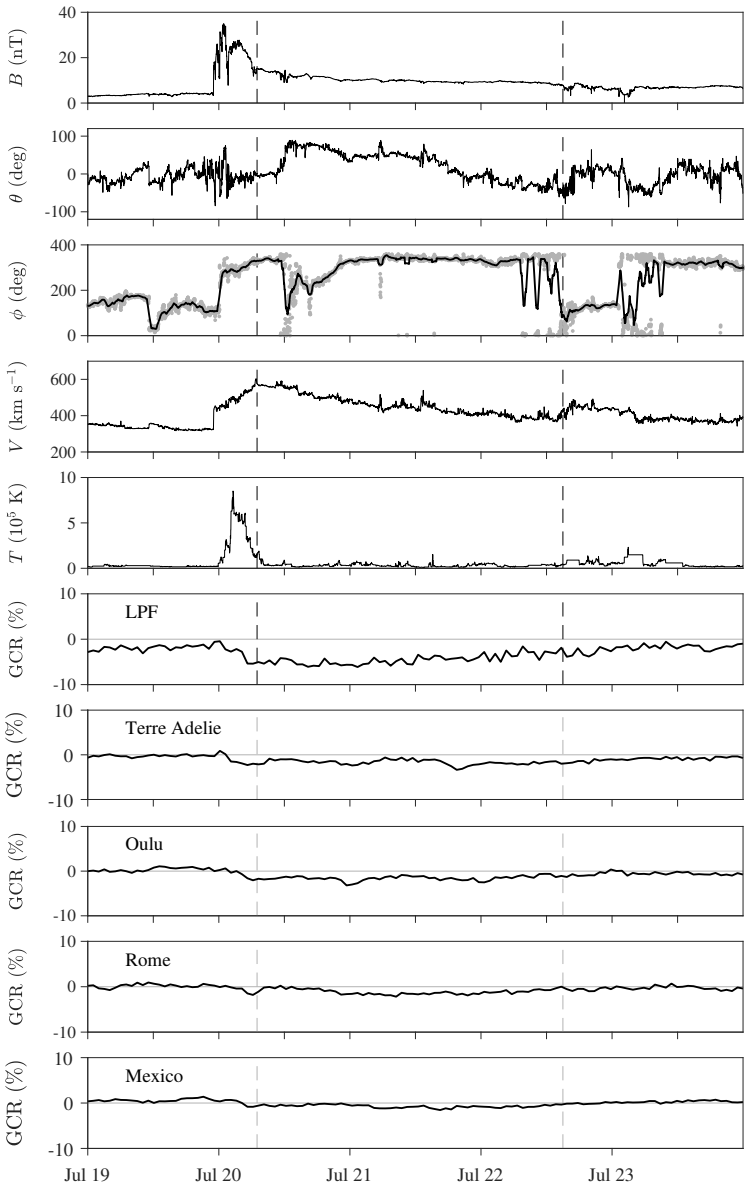

Figure 4.13 Magnetic field, solar wind and GCR data from July 19, 2016 through July 24, 2016. From top to bottom: IMF magnitude B, IMF GSE latitude θ, IMF GSE longitude ϕ, with a smoothed solid line overlaid, solar wind speed V, plasma temperature T, GCR percentage flux variations gathered by LPF compared to four NMs.

of three near-Earth ICMEs[2], associated with these FDs, is indicated by

[2]The ICME arrival and end times are taken from the catalog available at the web page http://www.srl.caltech.edu/ACE/ASC/DATA/level3/icmetable2.htm.

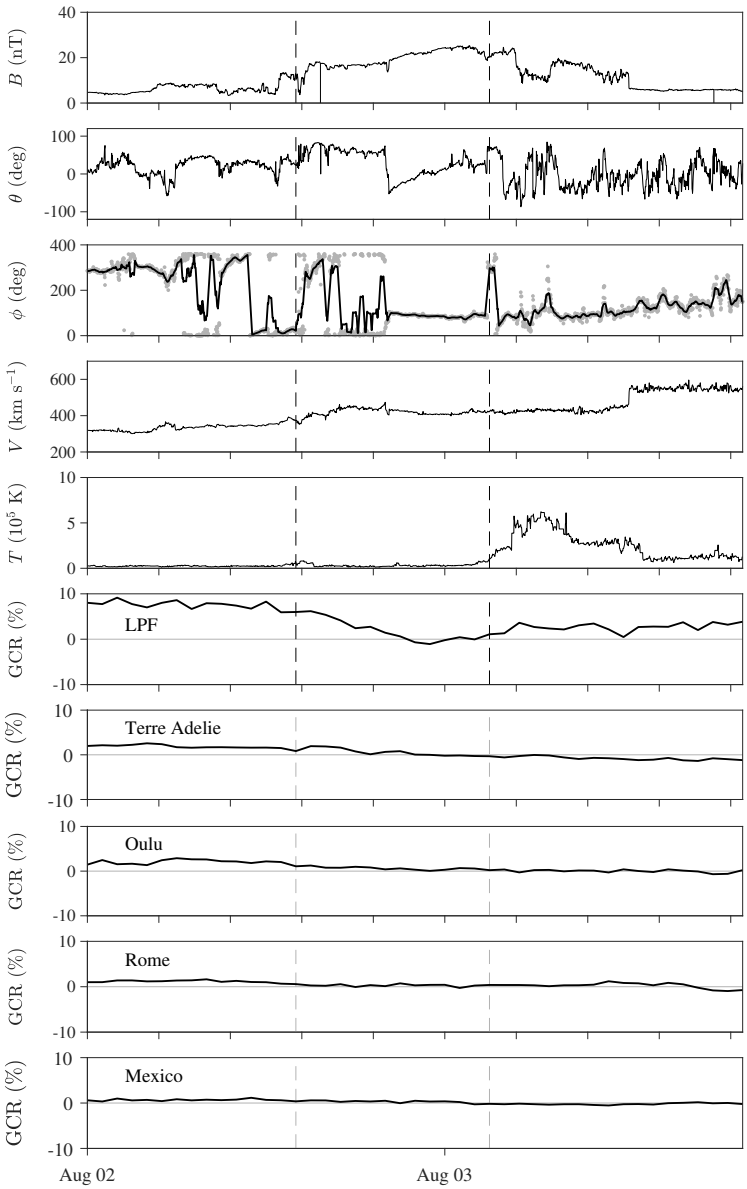

Figure 4.14 Same as Fig. 4.13 for the period August 2-4, 2016.

dashed vertical lines in the figures. In the same figures, GCR flux variations of both LPF and NMs are compared to the IMF magnitude B, IMF GSE latitude θ, IMF GSE longitude ϕ, solar wind speed V and temperature T gathered from the Wind experiment. First, as the minimum energy of GCR particles observed with the LPF PD is 70 MeV n^{-1}, it can be noted that the evolution of FDs, being strongly energy dependent, appears different in space and NM observations. The FD dated July 20,

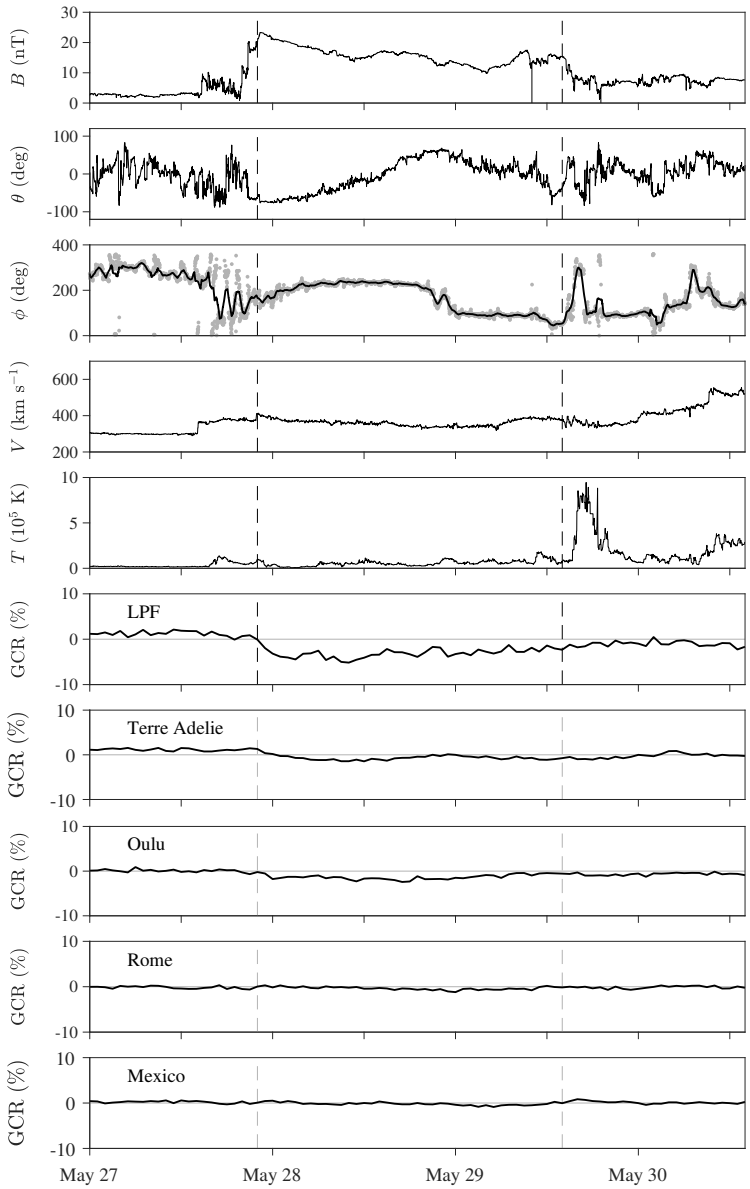

Figure 4.15 Same as Fig. 4.13 for the period May 27-30, 2017.

2016 is associated with both solar wind speed and IMF increases due to the ICME arrival. On August 2, 2016 and May 27, 2017 the GCR flux depressions are associated with slower ICMEs. In all three cases the IMF intensity presented maximum values of about 25 nT. In order to study the energy dependence of the three FDs observed with LPF, the percentage variation of the integral proton and helium fluxes measured with the LPF PD are compared to analogous hourly averaged variations gathered

with Terre Adelie, Oulu, Rome and Mexico NMs, located at different geographic latitudes. Table 4.7 shows the GCR flux variations of the GCR integral flux observed with LPF and with NMs listed above at the maximum amplitude of each FD. The time of the onset and the maximum amplitude of each FD on board LPF are also indicated. The onset was set as the first time bin after which the GCR flux presented a continuous decreasing trend, within statistical uncertainty, for at least six hours. The LPF proton-dominated integral flux maximum decreases above 70 MeV n^{-1} are observed to vary from about 5% to 9% for the three events. The different GCR flux decrease observed with LPF is most likely due to the passage of interplanetary disturbances that depressed the GCR flux before the transit of the ICMEs. During the August 2, 2016 event only, the pre-decrease GCR flux appeared at its maximum value during the BR 2496 before the passage of the ICME that generated the FD. NM count rate variations range between 1% and 3% for these three events. In particular, both GCR main and recovery phases are observed in all considered NM measurements during the July 20, 2016 FD. This is not the case for the other two events that can be clearly detected only in polar NMs. The passages of other three near-Earth ICMEs on March 5, 2016, April 14, 2016 and October 13, 2016 resulted in GCR flux decreases at the limit of the statistical significance (1%-2%) on board LPF, when the GCR flux was already depressed by the transit of previous interplanetary structures and HCS crossings.

Table 4.7. Energy dependence of GCR flux variations at the maximum of the three FDs observed on board LPF above 70 MeV n^{-1} and with NMs above effective energies: 11 GeV for polar stations; 12 GeV for Oulu NM; 17 GeV for Rome NM, and 20 GeV for Mexico NM.

LPF FD onset time	LPF FD maximum time	LPF PD	Polar NMs	Oulu NM	Rome NM	Mexico City NM
Jul 20, 2016 07.00 UT	Jul 21 01.00 UT	5.5%	2%	2%	2%	1%
Aug 2, 2016 12.00 UT	Aug 02 22.40 UT	9%	3%	2%	2%	1%
May 27, 2017 18.00 UT	May 28 10.45 UT	7%	3.5%	2.5%	1%	1%

Chapter 5

Grad-Shafranov reconstruction of the August 2, 2016 magnetic cloud

In order to evaluate the modulation effect of MCs on cosmic rays, a global knowledge of the magnetic field topology within the MC is necessary. In this chapter the GS reconstruction has been performed to retrieve the spatial configuration of the August 2, 2016 MC using *in situ* Wind data. This technique is based on the GS equation and consists mainly of three steps. The first step is the De Hoffmann-Teller (HT) analysis, that allows for the determination of the MC reference frame velocity. The second step is the search for the optimal invariant axis of the MC, thus the MC reference frame is fixed with respect to the GSE. The third and final step provides the GS reconstruction through a Taylor expansion of the vector potential on the reconstruction plane. Among the ICMEs associated with the three FDs observed on board LPF, only for the ICME associated with the August 2, 2016 event the GS reconstruction provided a successful result as discussed in the following.

5.1 The Grad-Shafranov reconstruction

The GS reconstruction was developed and applied for the first time by Sonnerup and Guo (1996) to retrieve 2-D structures at the magnetopause boundary. The application of the GS reconstruction in the space physics field was developed by Hau and Sonnerup (1999). The method consists of using the GS equation in order to obtain a 2-D vector potential map through a Taylor expansion.

The development of the GS reconstruction represents the focused effort of Prof. Sonnerup in contriving a useful data analysis technique that goes beyond the conventional one. Indeed, a proper interpretation of *in situ* S/C data is often challenging. This concept is illustrated in the cartoon of Figure 5.1 which was shown during the Prof. Sonnerup's Van Allen Lecture at the 2010 AGU Fall Meeting. All the steps of the GS reconstruction are described below.

5.1.1 The Grad-Shafranov equation

The GS equation derivation shown in this section is based on the magnetohydrodynamics (MHD) theory, even though could be also derived from

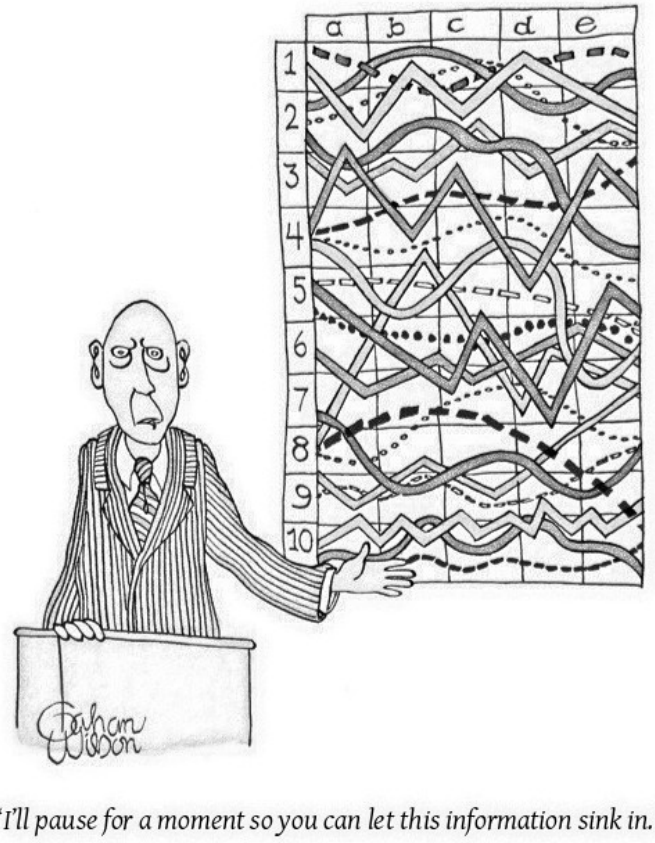

Figure 5.1 Cartoon presented in Prof. Sonnerup's Van Allen Lecture at the 2010 AGU Fall Meeting (New Yorker Magazine, available from http://www.newyorker.com/cartoons/a15439).

the Vlasov theory. From the ideal MHD equations, a two-dimensional magnetohydrostatic structure is described by the balance of pressure and magnetic forces:

$$\nabla p = \boldsymbol{j} \times \boldsymbol{B}, \tag{5.1}$$

where p is the plasma pressure and $\boldsymbol{j}$ is the electric current. Since ∇p is everywhere perpendicular to $\boldsymbol{B}$, the plasma pressure is constant along any field line thus representing the first field line invariant. By assuming the invariance along the z-axis of a cartesian coordinate system, equation (5.1) holds on the x-y plane that is the GS reconstruction plane. The x-y plane is oriented such that the x-axis represents the projection of the S/C path through the structure. The axis orientation is set on the basis the HT analysis (see Section 5.1.2 for details). In this reference frame, magnetic field and plasma pressure, measured along the S/C path while crossing the magnetic structure, are known along the x-axis. From the 2-D geometry assumption, the vector potential in the reconstruction plane is defined as $A(x, y)$ and the magnetic field vector can be expressed as follows

$$\boldsymbol{B} = \nabla \boldsymbol{A} \times \hat{\boldsymbol{z}} + \hat{\boldsymbol{z}} B_z,$$

where $\hat{\boldsymbol{z}}$ is the unit vector of the z-axis. In components

$$\boldsymbol{B} = \left(\frac{\partial A}{\partial y}, -\frac{\partial A}{\partial x}, B_z(x, y) \right). \tag{5.2}$$

The field lines are represented by contours $A(x, y) = const.$ Vectors projected in the x-y plane are assumed transverse to the invariant z-axis and are denoted with the subscript t. Since the z component in the left-hand side of equation (5.1) is identically zero, it follows that the z component of the magnetic force in the right-hand side of equation (5.1) also vanishes

$$\boldsymbol{j}_t \times \boldsymbol{B}_t = 0$$

and therefore the electric current $\boldsymbol{j}_t$ in the reconstruction plane is aligned with the transverse magnetic field $\boldsymbol{B}_t$. The Ampère's law allows to express $\boldsymbol{j}_t$ as follows

$$\boldsymbol{j}_t = \frac{1}{\mu_0} \nabla B_z \times \hat{\boldsymbol{z}}.$$

In order for the electric current to be parallel to $\boldsymbol{B}_t$, the vector ∇B_z must be perpendicular to $\boldsymbol{B}_t$ and therefore B_z is constant for any given field line and represents the second field line invariant. The force balance expressed by equation (5.1) allows for writing the following equation in

the reconstruction frame

$$\nabla p = j_z(\hat{\boldsymbol{z}} \times \boldsymbol{B}_t) + \boldsymbol{j}_t \times \hat{\boldsymbol{z}} B_z. \tag{5.3}$$

In equation (5.3) the axial current component can be written in terms of the vector potential as $j_z = -\nabla^2 A/\mu_0$. It can be shown that

$$\hat{\boldsymbol{z}} \times \boldsymbol{B}_t = \nabla A \qquad \text{and} \qquad \boldsymbol{j}_t \times \hat{\boldsymbol{z}} = -\frac{1}{\mu_0}\nabla B_z$$

and by substituting these expressions in equation (5.3) it is obtained

$$\nabla p = -\left[\left(\frac{1}{\mu_0}\right)\nabla^2 A\right]\nabla A - \left(\frac{1}{\mu_0}\right) B_z \nabla B_z. \tag{5.4}$$

Since both p and B_z are field line invariants, they are functions of A only and their gradients can be written as

$$\nabla p = \frac{dp}{dA}\nabla A, \quad \nabla B_z = \frac{dB_z}{dA}\nabla A.$$

Using these expressions in equation (5.4), each term is proportional to the vector potential A which can be simplified. The result reduces to the GS equation:

$$\nabla^2 A = \frac{\partial^2 A}{\partial x^2} + \frac{\partial^2 A}{\partial y^2} = -\mu_0 \frac{dP_t}{dA} = -\mu_0 j_z \tag{5.5}$$

where $P_t(A) = (p + B_z^2/2\mu_0)$ is the transverse pressure (Grad and Rubin, 1958; Shafranov, 1958). The GS equation is Poisson-like with a source term on the right-hand side that is a function of the dependent variable A only. This equation represents the basis of the GS reconstruction scheme.

5.1.2 The De Hoffmann-Teller analysis

The study of MCs is carried out in a special reference frame in which they appear stationary in time. A frame velocity is set so that physical quantities can be determined. The standard method to find the velocity of this reference frame from single S/C data relies on the HT method (De Hoffmann and Teller, 1950). In general, the term HT frame refers to a galilean frame of reference in which the electric field in the plasma vanishes. The existence of an HT frame indicates the presence of a coherent, quasi-stationary structure of magnetic field and plasma. In the

following, we refer to the HT analysis as the procedure of identifying an HT frame for a given data set. The aim is to find the frame velocity vector $\boldsymbol{V}_{HT}$ that shows the best agreement with measurements of magnetic field $\boldsymbol{B}$ and electric field $\boldsymbol{E}$. Sometimes, the convection electric field $\boldsymbol{E}_c$, computed starting from the plasma bulk velocity $\boldsymbol{v}$ as $-\boldsymbol{v} \times \boldsymbol{B}$, is used as a proxy for $\boldsymbol{E}$. Thus, the HT analysis is an attempt to characterize experimental data of solar wind velocity and IMF within a model at the basis of which there is one vector, i.e. $\boldsymbol{V}_{HT}$, as a parameter. If the electric field measured in the instrument frame is $\boldsymbol{E}$, the electric field in the HT frame $\boldsymbol{E}'$ vanishes as

$$\boldsymbol{E}' = \boldsymbol{E} + \boldsymbol{V}_{HT} \times \boldsymbol{B} = 0. \tag{5.6}$$

Equation (5.6) ensures that any magnetic field configuration is stationary when viewed in that frame by applying the Faraday's law

$$\nabla \times \boldsymbol{E}' = -\left(\frac{\partial \boldsymbol{B}}{\partial t}\right)' = 0. \tag{5.7}$$

In order to obtain an approximation for $\boldsymbol{V}_{HT}$ from a set of plasma bulk velocity $\boldsymbol{v}^{(m)}$ and magnetic field $\boldsymbol{B}^{(m)}$ measurements, where $m = 1, 2 \ldots M$ and M equal to the total number of collected data points, one may seek a reference frame in which the mean square of the electric field is minimized. This is accomplished by defining the functional $D(\boldsymbol{V})$ as

$$D(\boldsymbol{V}) = \frac{1}{M} \sum_{m=1}^{M} |\boldsymbol{E}'^{(m)}|^2 = \frac{1}{M} \sum_{m=1}^{M} |(\boldsymbol{v}^{(m)} - \boldsymbol{V}) \times \boldsymbol{B}^{(m)}|^2, \tag{5.8}$$

and assigning to the HT velocity $\boldsymbol{V}_{HT}$ the vector $\boldsymbol{V}$ that minimizes $D(\boldsymbol{V})$. Since the quantity $D(\boldsymbol{V})$ is a non-negative quadratic form, it must have a unique minimum. By writing the equation (5.8) in components we get

$$\frac{1}{M} \sum_{m=1}^{M} \{|\boldsymbol{B}^{(m)}|^2 [v_i^{(m)} - V_i]^2 - [B_i^{(m)} (v_i^{(m)} - V_i)]^2\}$$

where the vector identity $|\boldsymbol{A} \times \boldsymbol{B}|^2 = |\boldsymbol{A}|^2 |\boldsymbol{B}|^2 - (\boldsymbol{A} \cdot \boldsymbol{B})^2$ is applied. The minimization condition leads to the following equation written in components

$$\frac{\partial D}{\partial V_i} = \frac{2}{M} \sum_{m=1}^{M} \{-|\boldsymbol{B}^{(m)}|^2 [v_i^{(m)} - V_i] + [B_i^{(m)} B_j^{(m)} (v_j^{(m)} - V_j)]\} = 0. \tag{5.9}$$

The right-hand side of equation (5.9) can be rearranged as follows

$$V_j \sum_{m=1}^{M} [(B^{(m)})^2 \delta_{ij} - B_i^{(m)} B_j^{(m)}] = \sum_{m=1}^{M} v_j^{(m)} [(B^{(m)})^2 \delta_{ij} - B_i^{(m)} B_j^{(m)}].$$

By defining a matrix $K^{(m)}$ as the matrix of projection $P^{(m)}$ into a plane perpendicular to $\boldsymbol{B}^{(m)}$ multiplied by $(B^{(m)})^2$

$$K_{ij}^{(m)} = (B^{(m)})^2 \left(\delta_{ij} - \frac{B_i^{(m)} B_j^{(m)}}{(B^{(m)})^2} \right) = (B^{(m)})^2 P_{ij}^{(m)} \tag{5.10}$$

and $K_0 = \langle K^{(m)} \rangle$, where angle brackets indicate the average of an enclosed quantity over the set of M measurements, equation (5.9) may be written in the simple form

$$K_0 \boldsymbol{V}_{HT} = \left\langle K^{(m)} \boldsymbol{v}^{(m)} \right\rangle. \tag{5.11}$$

Finally, by assuming that K_0 is non-singular, the equation (5.11) admits the solution

$$\boldsymbol{V}_{HT} = K_0^{-1} \left\langle K^{(m)} \boldsymbol{v}^{(m)} \right\rangle. \tag{5.12}$$

Equation (5.12) expresses the HT frame velocity in terms of $\boldsymbol{v}^{(m)}$ and $\boldsymbol{B}^{(m)}$. In order to quantify the goodness of the computed HT frame, the correlation coefficient between the two electric fields $\boldsymbol{E}_c^{(m)} = -\boldsymbol{v}^{(m)} \times \boldsymbol{B}^{(m)}$ and $\boldsymbol{E}_{HT} = -\boldsymbol{V}_{HT} \times \boldsymbol{B}^{(m)}$ is estimated.

A natural extension of this procedure is to consider a constant acceleration of the HT frame as another parameter. Indeed, is possible to formally include a time-dependent velocity $\boldsymbol{V}(t)$ instead of $\boldsymbol{V}$ in the expression (5.8). Then a minimization of $D(\boldsymbol{V}(t))$ can be carried out in order to obtain the time-dependent HT velocity $\boldsymbol{V}_{HT}(t)$. In the linear approximation, the data fit is operated with a uniformly accelerating HT frame: $\boldsymbol{V}(t) = \boldsymbol{V}_0 + \boldsymbol{a}t$. The parameter values $\boldsymbol{V}_0 = \boldsymbol{V}_{HT}^{(0)}$ and $\boldsymbol{a} = \boldsymbol{a}_{HT}$ that minimize $D(\boldsymbol{V}(t))$ are determined from the following set of linear equations (Sonnerup et al., 1987)

$$K_0 \boldsymbol{V}_{HT}^{(0)} + K_1 \boldsymbol{a}_{HT} = \left\langle K^{(m)} \boldsymbol{v}^{(m)} \right\rangle$$

$$K_1 \boldsymbol{V}_{HT}^{(0)} + K_2 \boldsymbol{a}_{HT} = \left\langle K^{(m)} \boldsymbol{v}^{(m)} t^{(m)} \right\rangle.$$

The matrices K_q with $q = 0, 1, 2$, in the left-hand side of the above

equations are defined as

$$K_q = \left\langle K^{(m)}[t^{(m)}]^q \right\rangle$$

where $K^{(m)}$ is given in equation (5.10). The time $t^{(m)}$ is the time at which the m-th measurement is performed with $t^{(1)} = 0$. The explicit solutions for $\boldsymbol{V}_{HT}^{(0)}$ and $\boldsymbol{a}_{HT}$ are

$$\boldsymbol{a}_{HT} = \left(K_0^{-1}K_1 - K_1^{-1}K_2\right)^{-1}\left(K_0^{-1}\langle K^{(m)}\boldsymbol{v}^{(m)}\rangle - K_1^{-1}\langle K^{(m)}\boldsymbol{v}^{(m)}t^{(m)}\rangle\right)$$

$$\boldsymbol{V}_{HT}^{(0)} = K_0^{-1}\left(\langle K^{(m)}\boldsymbol{v}^{(m)}\rangle - K_1\boldsymbol{a}_{HT}\right).$$

After determining the HT velocity of the magnetic structure, the following step is to estimate the direction of the invariant axis and to set the best reference frame where the z-axis represents the axis of the MC.

5.1.3 The GS invariant axis orientation

The first technique proposed to estimate the invariant axis orientation is the minimum variance analysis. In general, the minimum variance analysis provides an estimation for the direction normal to a one-dimensional transition layer in plasma starting from single S/C data. In this context, the procedure that allows for the determination of the normal unit vector, $\hat{\boldsymbol{n}}$, with respect to the transition layer, is the minimum variance analysis of magnetic field vector (MVAB) data, acquired by a S/C during the layer crossing. The MVAB is based on the one-dimensional model of a generic layer in which $\partial/\partial x = 0$ and $\partial/\partial y = 0$. Only one of the z term remains in the cartesian expression for the divergence of $\boldsymbol{B}$

$$\nabla \cdot \boldsymbol{B} = \frac{\partial B_z}{\partial z} = 0, \tag{5.13}$$

i.e. B_z is independent of z. Here the triad (x, y, z) is a local coordinate system with z-axis pointing toward the vector normal to the layer $\hat{\boldsymbol{n}}$, that is unknown *a priori*. From the Faraday's law, the B_z component must be also time-independent, $\partial B_z/\partial t = 0$, thus in the ideal layer crossed by the S/C, the observed B_z value is constant. Only three magnetic vector measurements are needed to estimate the normal direction in this case, $\boldsymbol{B}^{(1)}$ and $\boldsymbol{B}^{(3)}$, measured on opposite sides of the layer, and $\boldsymbol{B}^{(2)}$,

measured approximately at the center of the layer. Since

$$\boldsymbol{B}^{(1)} \cdot \hat{\boldsymbol{n}} = \boldsymbol{B}^{(2)} \cdot \hat{\boldsymbol{n}} = \boldsymbol{B}^{(3)} \cdot \hat{\boldsymbol{n}},$$

vectors $(\boldsymbol{B}^{(1)} - \boldsymbol{B}^{(2)})$ and $(\boldsymbol{B}^{(2)} - \boldsymbol{B}^{(3)})$ are tangential with respect to the layer and their cross product lies along $\hat{\boldsymbol{n}}$. By assuming that their cross product is not zero, it follows that

$$\hat{\boldsymbol{n}} = \pm \frac{(\boldsymbol{B}^{(1)} - \boldsymbol{B}^{(2)}) \times (\boldsymbol{B}^{(2)} - \boldsymbol{B}^{(3)})}{|(\boldsymbol{B}^{(1)} - \boldsymbol{B}^{(2)}) \times (\boldsymbol{B}^{(2)} - \boldsymbol{B}^{(3)})|}.$$

Looking at real transition layers observed in space plasmas, pronounced deviations from this ideal one-dimensional description are always observed. Indeed, real layers have 2-D or 3-D internal structures evolving in time with temporal fluctuations also in the orientation of the normal direction. In general, the MVAB technique is designed to deal with the situation where some or all of the non-ideal effects listed above are present, except for the systematic temporal change in the normal direction. To estimate $\hat{\boldsymbol{n}}$, the method identifies the direction along which the field-component $\{\boldsymbol{B}^{(m)} \cdot \hat{\boldsymbol{n}}\}$ has minimum variance. In other words, $\hat{\boldsymbol{n}}$ is determined by minimization of

$$\sigma^2 = \frac{1}{M} \sum_{m=1}^{M} \left| (\boldsymbol{B}^{(m)} - \langle \boldsymbol{B} \rangle) \cdot \hat{\boldsymbol{n}} \right|^2$$

where $\langle \boldsymbol{B} \rangle = 1/M \sum_{m=1}^{M} \boldsymbol{B}^{(m)}$. The normalization constraint for this minimization procedure is $|\hat{\boldsymbol{n}}|^2 = 1$. Using the Lagrange multiplier, λ, to impose this condition, a set of three homogeneous linear equations is obtained

$$\frac{\partial}{\partial n_i}(\sigma^2 - \lambda(|\hat{\boldsymbol{n}}|^2 - 1)) = 0 \tag{5.14}$$

where $i = (X, Y, Z)$ is the coordinate system used in performing the $\{\boldsymbol{B}^{(m)}\}$ measurements (e.g. the GSE reference frame). After differentiating equation (5.14), the resulting set of three equations can be written a matrix form

$$\sum_{\nu=1}^{3} M^B_{\mu\nu} = \lambda n_\mu \tag{5.15}$$

where the subscripts $\mu, \nu = 1, 2, 3$ are cartesian components along the X, Y, Z coordinate system and

$$M^B_{\mu\nu} = \langle B_\mu B_\nu \rangle - \langle B_\mu \rangle \langle B_\nu \rangle$$

is the magnetic variance matrix. From equation (5.15), λ are the eigenvalues $\lambda_1, \lambda_2, \lambda_3$, given in order of decreasing magnitude, of the matrix $M^B_{\mu\nu}$. Since $M^B_{\mu\nu}$ is symmetric, the eigenvalues are real and the corresponding eigenvectors $\boldsymbol{x}_1$, $\boldsymbol{x}_2$ and $\boldsymbol{x}_3$ are orthogonal. The eigenvectors represent the maximum, intermediate, and minimum variance directions and the eigenvalues are the variances in the magnetic field components. The eigenvector $\boldsymbol{x}_3$, corresponding to the smallest eigenvalue λ_3, is used as the estimator of the vector normal to the layer. Eigenvectors $\boldsymbol{x}_1$ and $\boldsymbol{x}_2$, corresponding to maximum and intermediate variance, are then tangential to the transition layer and the set $\{\boldsymbol{x}_1, \boldsymbol{x}_2, \boldsymbol{x}_3\}$ provides the basis vectors for the local coordinates (x, y, z) introduced in equation (5.13). More generally, for any measured set of magnetic field vectors $\{\boldsymbol{B}^{(m)}\}$ the eigenvector set of the variance matrix $M^B_{\mu\nu}$ provides a natural coordinate system for the analysis of the data. It is worthwhile to notice that the matrix $M^B_{\mu\nu}$ does not depend on the temporal order of the measured vectors.

While the MVAB analysis was the first used in the literature to determine the orientation of the invariant axis for a given magnetic structure in plasma, here it is used only as a first guess. Indeed, a more reliable procedure of optimization/minimization to estimate the invariant axis was introduced by Hu and Sonnerup (2002). To this purpose the definition of the transverse pressure $P_t(A)$, given in equation (5.5), as a single-valued function of the potential vector A is used. The axis orientation of a cylindrical MC is determined by finding the direction for which the data plot of $P_t(x_i, 0)$ versus $A(x_i, 0)$ displays minimal scatter, where x_i are S/C coordinates while crossing the MC. Indeed, the transverse pressure P_t as a function of A shows an increase when the S/C enters the cylindrical MC structure toward the center and, consequently, decreases while approaching the end point of the structure. Dividing the transverse pressure into two branches, the curve associated with the first-half of the S/C path through the MC $P^{1st}_{t,i}(A)$ is expected to lie on the same curve that describes the second-half of the S/C path, $P^{2nd}_{t,i}(A)$. In other words, a well defined single-valued function $P_t(A)$ would be expected if the GS equation holds. Therefore, a separation between the $P^{1st}_{t,i}(A)$ and $P^{2nd}_{t,i}(A)$ curves is an indication that the z axis chosen for the analysis is not right. In the optimization procedure introduced by Hu and Sonnerup (2002), invariant direction seeking is numerically performed by a trial and error procedure. Algorithm steps are listed below.

1) The first step consists in making a first guess for the reconstruction frame, (x, y, z). For MCs, the first guess for the optimal z-axis is

done through the MVAB. The x-axis lies along the projection of the $-\boldsymbol{V}_{HT}$ vector onto the plane perpendicular to z. The positive x-axis is directed along the projected S/C path across the MC. Thus, the structure is invariant in the z direction, the S/C measurements are known along the x-axis and y completes the right-handed orthogonal triad.

2) In the second step values of $A(x,0)$ are computed from equation (5.2) by integrating the measured B_y component along the x-axis with $y = 0$

$$A(x,0) = \int_0^x \frac{\partial A}{\partial \xi} d\xi = \int_0^x -B_y(\xi,0) d\xi$$

where $y = 0$ is set along the S/C path coordinate in the reconstruction frame. Steps in the x direction are made using time steps and the constant HT frame velocity: $d\xi = -\boldsymbol{V}_{HT} \cdot \hat{\boldsymbol{x}} dt$. Data are resampled on a uniform grid along x and the scatter-plot between $P_t(x,0) = p(x,0) + B_z^2(x,0)/2\mu_0$ versus $A(x,0)$ is evaluated.

The trial and error procedure consists in repeating steps 1) and 2) for each trial axis. The orientation of the trial axis varies on a hemisphere that represents all possible directions in a 3-D space. The coordinate system of this 3-D space is chosen as follows: the maximum variance direction $\hat{\boldsymbol{x}}_1$ yields a first estimation for the y axis because the magnetic variance is likely to be largest along the y axis as B_y reverses sign during the MC crossing whereas the variations in the other two components are usually smaller, x is chosen to be along the $-\boldsymbol{V}_{HT}$ direction and z completes the orthogonal triad. The hemisphere is discretized in a grid in which each grid point represents a trial axis direction. The fitting residue for $P_t(A)$, associated with each trial axis is defined by

$$\mathcal{R}_f = \left[\sum_{i=1}^{M} \left(P_{t,i}^{1st} - P_{t,i}^{2nd} \right)^2 \right]^{\frac{1}{2}} / |\max(P_t) - \min(P_t)|. \tag{5.16}$$

Finally, the best invariant direction is that one along which the residue calculated from equation (5.16) has its absolute minimum.

5.1.4 The GS solver

The final step of the GS reconstruction algorithm consists in calculating the vector potential of the magnetic field $A(x,y)$ at y values distant from

the S/C path placed at $y = 0$. To achieve this task, the GS solver uses the following second-order Taylor expansion

$$A(x, y + \Delta y) \simeq A(x, y) + \frac{\partial A(x, y)}{\partial y}\Delta y + \frac{1}{2}\frac{\partial^2 A(x, y)}{\partial y^2}(\Delta y)^2 \qquad (5.17)$$

where $A(x, y)$ and $\partial A(x, y)/\partial y = B_x$ are assumed to be known functions of x at a given y. The second derivative in equation (5.17) is evaluated through the equation (5.5) as

$$\frac{\partial^2 A}{\partial y^2} = -\frac{\partial^2 A}{\partial x^2} - \mu_0 \frac{dP_t}{dA}, \qquad (5.18)$$

where $\partial^2 A/\partial x^2$ is known. The calculation starts at $y = 0$ where all the quantities are known and then continues in $\pm|\Delta y|$ steps. From equations (5.17) and (5.18) $A(x, y + \Delta y)$ is evaluated and then $\partial A(x, y + \Delta y)/\partial x = -B_y(x, y + \Delta y)$ and $\partial^2 A(x, y + \Delta y)/\partial y^2$ can be calculated. The new value of $B_x(x, y + \Delta y) = \partial A(x, y + \Delta y)/\partial y$ is obtained from the first-order Taylor expansion

$$B_x(x, y + \Delta y) \simeq B_x(x, y) + \frac{\partial^2 A(x, y)}{\partial y^2}\Delta y,$$

where $\partial^2 A(x, y)/\partial y^2$ is obtained from equation (5.18). The present GS solver is based on the rectangular box integration domain introduced by Hau and Sonnerup (1999) that follows the scheme

$$\left(\frac{\partial^2 A}{\partial x^2}\right)_i = \frac{2A_i - 5A_{i+1} + 4A_{i+2} - A_{i+3}}{(\Delta x)^2}$$

that is a third-order Taylor expansion in Δx around the end point. The reconstruction is performed within a rectangular box and the number of grid points along y are kept about one order of magnitude larger than the number of x grid points in order to limit numerical instabilities. A smoothing is performed for the solution of A at each integration step to eliminate spurious exponential solutions.

5.2 The August 2, 2016 magnetic cloud

In this section the GS reconstruction is applied to the August 2, 2016 MC event. The MC passage was inferred from solar wind plasma and magnetic field parameters and was set between August 2, 2016 at 20:11

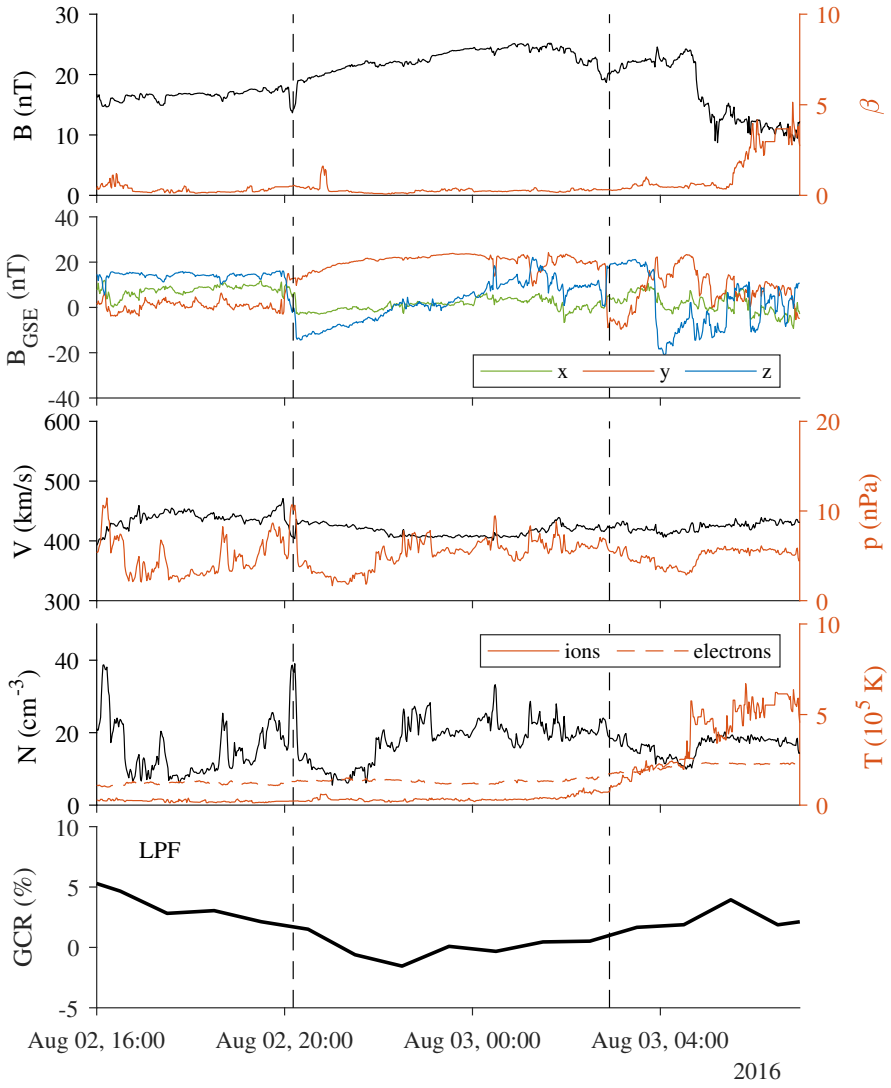

Figure 5.2 Data gathered in the Lagrange point L1 with the Wind satellite and the LPF PD on magnetic field, plasma (panels 1-4) and cosmic-ray (bottom panel) observations during August 2-3, 2016. The MC transit time is represented by vertical dashed lines.

UT and August 3, 2016 at 2:54 UT as shown in Figure 5.2. The same MC is also reported in the Hu et al. (2018) small-scale flux-rope database

based on the Wind S/C data[1]. Using plasma and magnetic field measurements from the Wind S/C, the HT analysis gives an excellent constant

[1]The small-scale flux-rope database is available at the web page http://fluxrope.info/index.html

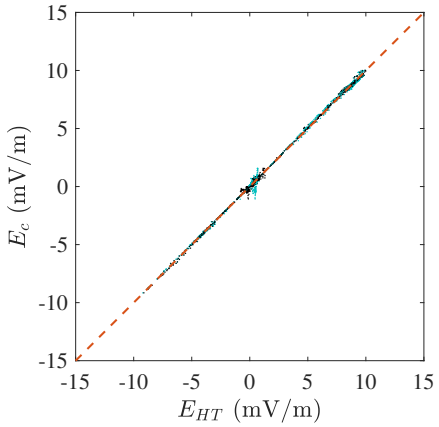

Figure 5.3 Scatter-plot of the convection electric field $\boldsymbol{E}_c = -\boldsymbol{v}^{(m)} \times \boldsymbol{B}^{(m)}$ versus the HT electric field $\boldsymbol{E}_{HT} = -\boldsymbol{V_{HT}} \times \boldsymbol{B}^{(m)}$ for constant HT velocity (cyan dots) and constant HT acceleration (black dots).

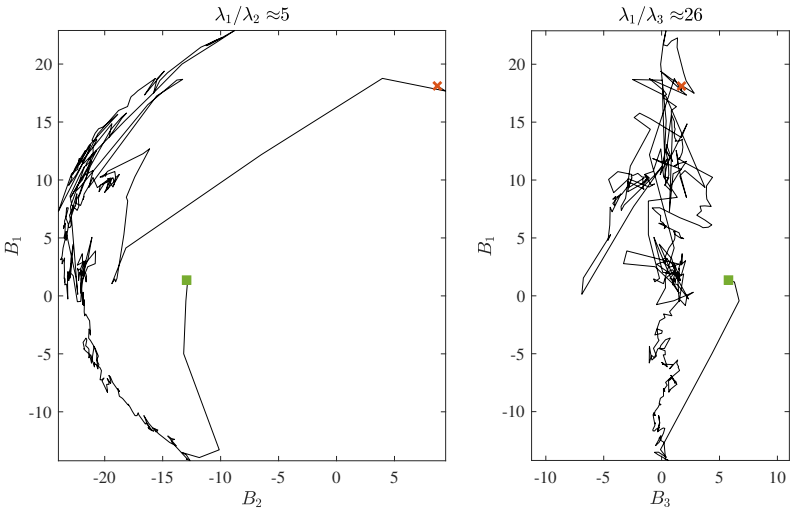

Figure 5.4 Magnetic hodograms for MC crossing by Wind on August 2, 2016, 20:11 UT - August 3, 2016, 02:54 UT. Axes units are in nT. Eigenvalue ratios are reported on top of the figure.

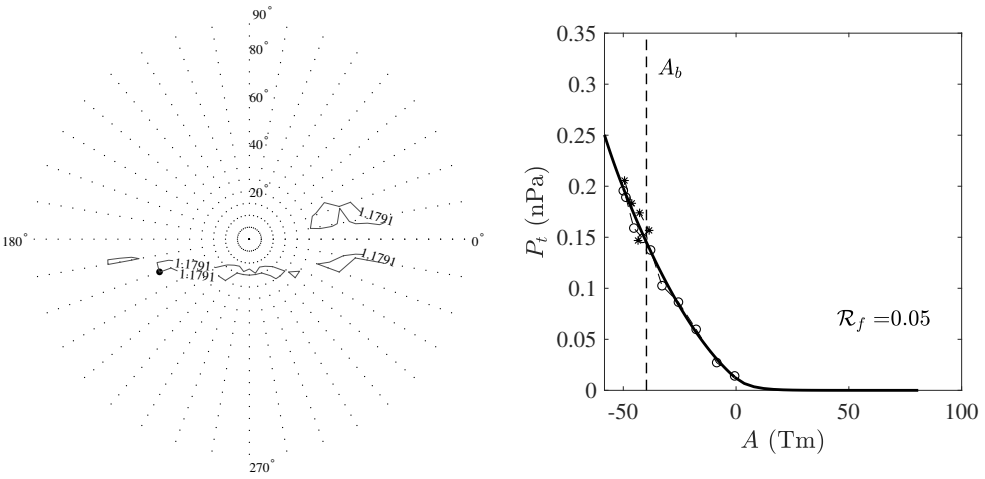

Figure 5.5 Left: Residue map. The black dot represents the minimum-residue direction. Right: Wind data and fitting curve of $P_t(A)$ for August 2, 2016 MC. Data points represent the S/C measurements for the first half (circles) and for the second half (stars) of the MC crossing. Solid curve represents the fitting function, $P_t(A)$. The fit residue is $\mathcal{R}_f = 0.05$ for this event and $A_b = -44.7$ Tm denotes the boundary value of the vector potential for the double folding of measured data.

$\boldsymbol{V}_{HT} = (-413.69, -27.94, 11.64)$ km s^{-1}, with a correlation coefficient among the measured electric field and $-\boldsymbol{V}_{HT} \times \boldsymbol{B} > 0.998$. The HT acceleration, computed according to the definition given in Section 5.1.2, is found equal to 5×10^{-3} km s^{-2}. Scatter plot of the convection electric field $\boldsymbol{E}_c$ and $\boldsymbol{E}_{HT} = -\boldsymbol{V}_{HT} \times \boldsymbol{B}$ is shown in Figure 5.3 both for constant HT velocity (cyan dots) and uniform HT acceleration (black dots). The output of the MVAB analysis is reported as hodograph. Magnetic hodographs consist of curves in space of vectors from the measured time series $\{\boldsymbol{B}^{(m)}\}$ connected by line segments that follow the time sequence in which they are measured. The most common way to display the hodographs is to organize them in two projections, called magnetic hodograms. The projection onto a plane tangential to the MC is the plot of the component $B_1 = \boldsymbol{B}^{(m)} \cdot \boldsymbol{x}_1$ versus $B_2 = \boldsymbol{B}^{(m)} \cdot \boldsymbol{x}_2$ and the side view projection is the plot of B_1 versus the normal field component $B_3 = \boldsymbol{B}^{(m)} \cdot \boldsymbol{x}_3$. Magnetic hodograms for the August 2, 2016 MC are shown in figure 5.4. The invariant axis orientation is determined by estimating the direction for which the plot of $P_t(x_i, 0)$ versus $A(x_i, 0)$ presents minimal scatter of the data. It is recalled here that x_i represent S/C positions along the MC crossing path. Starting from the reference frame fixed through the MVAB, the

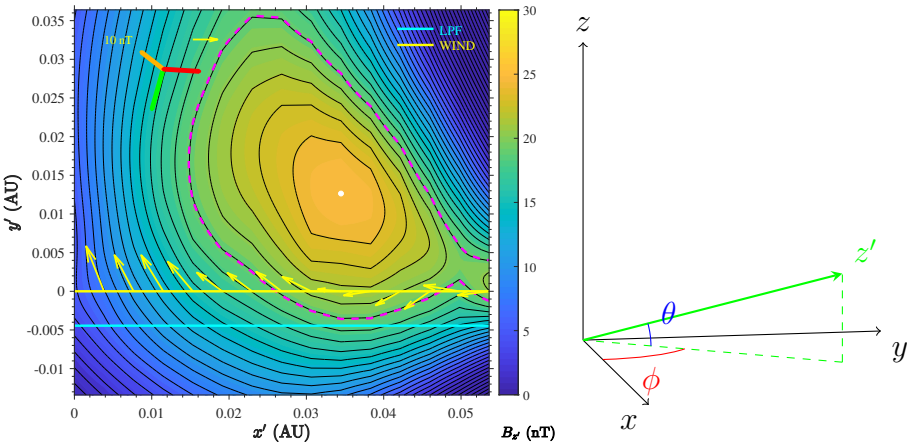

Figure 5.6 Left: GS reconstruction of the August 2, 2016 MC. Wind (yellow) and LPF (cyan) S/C paths across the MC are shown. The color plot represents the z' component of the magnetic field in the GS reconstruction frame of reference and the solid level curves represent the potential vector $A(x', y')$. A projection of the GSE frame of reference is reported in the upper-left corner (x in red, y in yellow and z in green). Right: Orientation of the MC axis z' with respect to the GSE reference frame (x, y, z) where $\theta = 17.3 \pm 1.7°$ and $\phi = 53.9 \pm 2.9°$.

trial and error procedure allows to calculate the residue associated with every possible orientation of the z-axis within an hemisphere according to equation (5.16). The residue map obtained through this procedure is shown in Figure 5.5 (left panel) where the minimum residue direction is marked with one black dot. For the best-fit a residue $\mathcal{R}_f = 0.05$ is found (Figure 5.5, right panel). The z-axis orientation corresponds to $\theta = 17.3 \pm 1.7°$ and $\phi = 53.9 \pm 2.9°$, where θ and ϕ are the latitude and longitude, respectively, in the GSE coordinate system.

The GS reconstruction of the MC dated August 2, 2016 is illustrated

Table 5.1. Characteristics of the August 2, 2016 MC.

MC properties	GS reconstruction values
Total axial magnetic flux, Φ_t	9.30×10^{21} Mx
Total poloidal magnetic flux per AU, Φ_p	5.55×10^{22} Mx
Maximum axial field strength, B_{z0}	25.3 nT
Maximum axial current density, j_{z0}	-7.5×10^{-12} A m^{-2}
Total axial current, I_{z0}	-2.4×10^{8} A

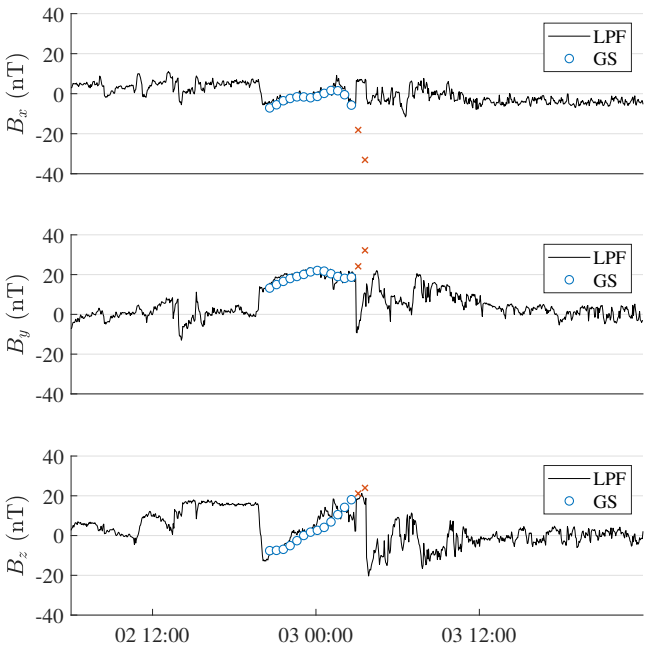

Figure 5.7 Comparison between the magnetic field GSE components measured by LPF (solid lines) and the August 2-3, 2016 magnetic field interpolated from the GS reconstruction (blue circles). A remarkable agreement is found on all three components with exception of latter two points (red crosses).

in Figure 5.6. The Wind S/C crossing path is set along the line $y' = 0$. In this reference frame the LPF S/C path lies along $y' = -4.4 \times 10^{-3}$ AU. In order to visualize the part of the magnetic map explored by LPF, the S/C path through the MC is reported in Figure 5.6 (cyan line). The time separation along x' between the two S/C is calculated assuming that the MC moves with mean constant velocity $\boldsymbol{V}_{HT}$. The space separation is $\delta x' = x'_L - x'_W$, where L and W indicate LPF and Wind respectively, and the corresponding time separation is $\delta t = \delta x'/(\boldsymbol{V}_{HT} \cdot \boldsymbol{x}') \sim -35.1$ min. In order to test the reliability of the GS reconstruction a multi-S/C approach is widely used in literature. To this purpose, LPF magnetic field measurements gathered by the four on board magnetometers described in Section 1.3 are available. The LPF magnetometers were not meant for scientific investigations, but were placed inside the S/C for diagnostics purposes. However, with a dedicated analysis it was possible to disentangle the magnetic field contribution generated by the S/C instrumentation from that associated with the background IMF (A. Cesarini, private communication). A comparison between magnetic field

data observed on board LPF binned at 1-minute and magnetic field interpolations obtained with the GS reconstruction along the LPF path is shown in Figure 5.7. There is a remarkable agreement between measurements and the GS reconstruction, with the exception of the latter two data points in the x and y components. This deviation arises from abrupt fluctuations in the magnetic field components after the MC passage due to incoming small-scale magnetic structures accompanied by an increasing trend of the plasma temperature. The sudden break of the smooth rotation in the measured magnetic field components reflects on the rapid variations of the magnetic field along the right boundary of the GS reconstruction. Finally, the assumption that this MC could be described as a magnetostatic structure in rigid coherent motion with constant HT velocity can be supported by evaluating the expansion velocity defined as

$$V_{exp} = \frac{(V_1 - V_2)}{2},$$

where $V_1 = 406.6$ km s^{-1} is the velocity at the front boundary of the MC and $V_2 = 421.5$ km s^{-1} the velocity at the back boundary. The HT velocity is $V_{HT} = 414.6$ km s^{-1} and the ratio $|V_{exp}|/|V_{HT}| = 0.018 \ll 1$ suggests that the MC expansion is not particularly significant in the time interval considered for this event (Möstl et al., 2009). All the main characteristics of this MC can be evaluated after the GS reconstruction and the total axial and poloidal magnetic fluxes, the total axial current and the maximum axial field strength and current density are reported in Table 5.1. Finally, a 3-D visualization of the MC is reported in Figure 5.8.

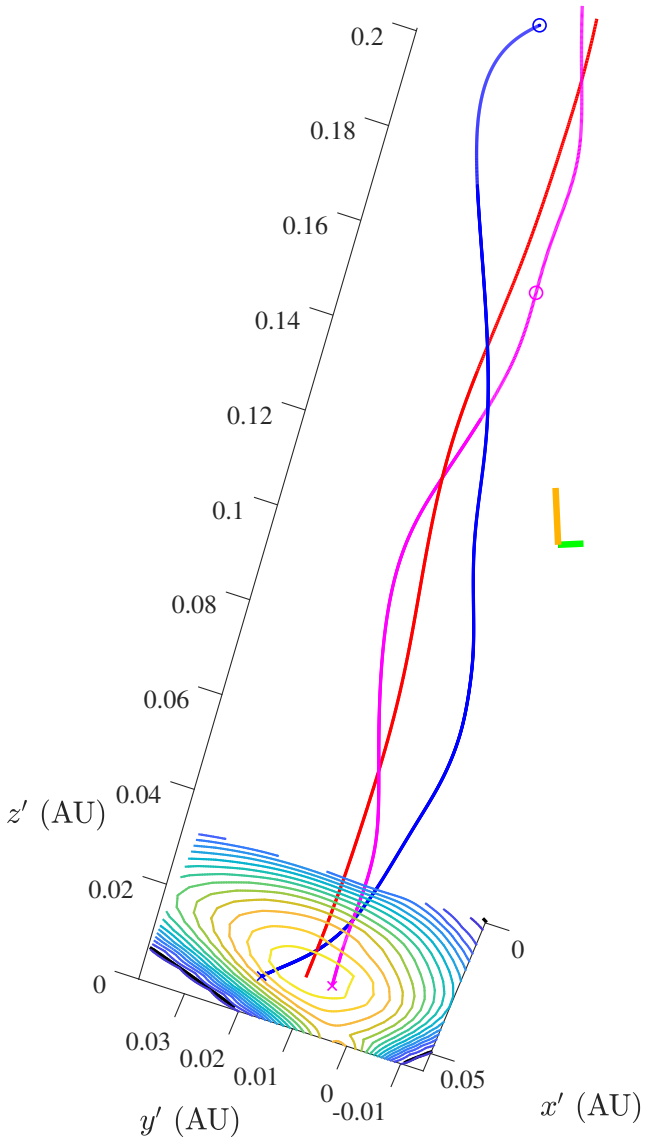

Figure 5.8 Three-dimensional representation of the GS reconstruction result for the August 2, 2016 MC. The reconstruction plane and the winding magnetic field lines are rotated with respect to the GSE coordinate system reported in the plot (y' in yellow, z' in green and x' orthogonal to the plane of the figure).

Chapter 6

Monte Carlo simulation of the August 2, 2016 Forbush decrease

In order to better understand the physical phenomena responsible for FDs, a novel approach is proposed in this chapter. A well suited Monte Carlo forward technique in the test-particle (TP) approximation is developed to describe the GCR propagation over the realistic MC configuration accurately retrieved through the GS reconstruction in Chapter 5. The Monte Carlo simulation has been carried out within the MC with full-particle-trajectory integration. The choice to adopt the full-trajectory integration, instead of the guiding-center approximation, is based on the dimension of the MC and the Larmor radii for the energies considered in the simulation. The simulation basics and the main results are presented in the following. To my knowledge, an attempt to study the GCR flux variation effect due to a realistic MC topology is carried out for the first time in this thesis work.

6.1 Algorithm description

Particle full-trajectories are estimated over the magnetostatic configuration provided by the GS reconstruction moving with constant HT velocity. Particles are subject to the Lorentz force where relativistic modifications are considered. Since in the model we deal with time-integrated particle trajectories, the physical quantity that we compute from the particle distribution function is the particle fluence through each volume element of the simulation space. The fluence variation profile across the

MC is computed with respect to the incident particle fluence. Main steps of the Monte Carlo TP simulation code are described below.

6.1.1 Particle initialization

As a first step, the initialization of position and velocity of the incident particles is carried out. According to the GS reconstruction output, where the magnetic field map is provided on a rectangular grid under the 2.5-D geometry assumption, the simulation space is thought as an infinite rectangular prism $[x_{\min}x_{\max}] \times [y_{\min}y_{\max}] \times L_z$, where L_z is the length along the symmetry axis and is kept arbitrary. The initial positions are randomly chosen along the rectangular boundaries of the simulation space at $L_z = 0$. The absolute value of initial velocities is randomly selected from a given relativistic proton kinetic energy spectrum. To guarantee an isotropic incidence for cosmic-ray particles entering the simulation space from planar surfaces, the Lambert cosine factor is used. The angle between the particle initial velocity and the direction normal to the surface crossed by the incoming particle is $\theta \in [0, \pi/2]$. The azimuthal angle ϕ is defined in the interval $[0, 2\pi)$, and it is selected from a uniform distribution within its domain of definition. After a kinetic energy E is selected from a proper proton energy spectrum, initial particle velocity components for particles entering from the plane that intersects the $x = x_{\min}$ side are

$$\begin{cases} v_y = v \sin\theta \cos\phi \\ v_z = v \sin\theta \sin\phi \\ v_x = v \cos\theta, \end{cases}$$

while for particles entering from the plane that intersects the $x = x_{\max}$ side

$$\begin{cases} v_y = v \sin\theta \cos\phi \\ v_z = v \sin\theta \sin\phi \\ v_x = -v \cos\theta \end{cases}$$

and for particles entering from the plane that intersects the $y = y_{\min}$ side

$$\begin{cases} v_z = v \sin\theta \cos\phi \\ v_x = v \sin\theta \sin\phi \\ v_y = v \cos\theta. \end{cases}$$

Finally, for particles entering from the plane that intersects the $y = y_{\max}$ side

$$\begin{cases} v_z = v \sin\theta \cos\phi \\ v_x = v \sin\theta \sin\phi \\ v_y = -v \cos\theta. \end{cases}$$

6.1.2 The Boris solver

As a second step particle trajectories are followed and collected in the simulation space. The particle motion is assumed to be collisionless and the magnetic configuration is kept stationary in time. In the TP approximation no currents associated with the particle propagation in the magnetic field are considered. Thus, the only force acting on the TPs is the Lorentz force. In general, the equation of motion of a charged particle through an electromagnetic field is given by

$$\frac{d\boldsymbol{p}}{dt} = q(\boldsymbol{E} + \boldsymbol{v} \times \boldsymbol{B})$$

where $\boldsymbol{v}$ is the particle velocity, $\boldsymbol{E}$ is the electric field, $\boldsymbol{B}$ is the magnetic field and $\boldsymbol{p}$ is the relativistic particle momentum. Since the particle integrator is a fundamental element of any charged-particle simulation (e.g. TPs or particle-in-cell) accuracy, stability, and computational cost must be considered during the implementation. The integrator used in this work is the well-known Boris solver, an energy-conserving trajectory integrator based on the Leapfrog scheme (Boris, 1970). The discrete equations of motion are written in the form:

$$\frac{\boldsymbol{x}_{n+\frac{1}{2}} - \boldsymbol{x}_{n-\frac{1}{2}}}{\Delta t} = \boldsymbol{v}_n$$

$$m\frac{\boldsymbol{u}_{n+\frac{1}{2}} - \boldsymbol{u}_n}{\Delta t} = q\big(\boldsymbol{E}_{n+\frac{1}{2}} + \bar{\boldsymbol{v}}_{n+\frac{1}{2}} \times \boldsymbol{B}_{n+\frac{1}{2}}\big) \tag{6.1}$$

where the subscripts $(n-1/2, n, n+1/2)$ are time step indices, Δt is the time step, $\boldsymbol{x}$ is the particle position, $\boldsymbol{u} = \gamma\boldsymbol{v}$ is the three-dimensional particle velocity, γ is the Lorentz factor and $\bar{\boldsymbol{v}}$ is an effective velocity. Other symbols have their standard meanings. The acceleration part of equation (6.1) is split into the Coulomb force for the first half time step (equation 6.2), the Lorentz force for the entire time step (equation 6.3),

and the Coulomb force for the second half (equation 6.4)

$$\boldsymbol{u}_- = \boldsymbol{u}_n + \boldsymbol{\epsilon}\Delta t \tag{6.2}$$

$$\frac{\boldsymbol{u}_+ - \boldsymbol{u}_-}{\Delta t} = \frac{q}{m}\left(\bar{\boldsymbol{v}}_{n+\frac{1}{2}} \times \boldsymbol{B}_{n+\frac{1}{2}}\right) \tag{6.3}$$

$$\boldsymbol{u}_{n+\frac{1}{2}} = \boldsymbol{u}_+ + \boldsymbol{\epsilon}\Delta t \tag{6.4}$$

where $\boldsymbol{\epsilon} = (q/2m)\boldsymbol{E}_{n+\frac{1}{2}}$, $\boldsymbol{u}_-$ and $\boldsymbol{u}_+$ are two intermediate states. Hereafter we denote the field quantity $\boldsymbol{B}_{n+\frac{1}{2}}$ at $n = n + 1/2$ as $\boldsymbol{B}$. Since equation (6.3) is an energy-conserving rotation in the momentum space, Figure 6.1, the Lorentz factor is set to be constant during the operation, $\gamma_- = \gamma_+$. The phase angle in the rotation part is

$$\theta = \frac{q\Delta t}{m\gamma_-}B. \tag{6.5}$$

The rotation is then solved as follows

$$\boldsymbol{t} = \tan\frac{\theta}{2}\boldsymbol{b}$$

where $\boldsymbol{b} = \boldsymbol{B}/|\boldsymbol{B}|$,

$$\boldsymbol{u}' = \boldsymbol{u}_- + \boldsymbol{u}_- \times \boldsymbol{t}$$

$$\boldsymbol{u}_+ = \boldsymbol{u}_- + \frac{2}{1+t^2}(\boldsymbol{u}' \times \boldsymbol{t}).$$

The only contribution to the Lorentz force taken into account in the following is the rigid rotation operated by the magnetic field $\boldsymbol{B}$ as the contribution of the electric field $\boldsymbol{E}$ is neglected according to the HT analysis, equation (5.7).

From a theoretical point of view, the Boris solver is stable because it preserves a volume in the phase space at each time step. This property can be examined by computing the norm of the Jacobian associated with the solver updating rule. Without loss of generality, the gyration motion of a particle moving inside a uniform magnetic field defined by $\boldsymbol{B} = (0, 0, B)$ is here considered as an example. The gyration motion is expressed by introducing the rotation matrix R, that updates the velocity

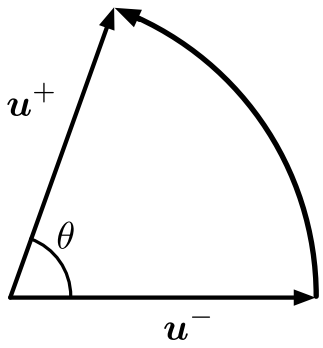

Figure 6.1 Schematic diagram for the Lorentz-force part of the Boris solver.

vector $\boldsymbol{u}$ to $\boldsymbol{u}'$:

$$\boldsymbol{u}' = R\boldsymbol{u} = \begin{pmatrix} \cos\theta & \sin\theta & 0 \\ -\sin\theta & \cos\theta & 0 \\ 0 & 0 & 1 \end{pmatrix} \begin{pmatrix} u_x \\ u_y \\ u_z \end{pmatrix}$$

where θ is defined in equation (6.5). The derivative of θ with respect to a generic velocity component u_α is

$$\frac{\partial\theta}{\partial u_\alpha} = \frac{qB\Delta t}{m}\frac{\partial}{\partial u_\alpha}\left(\frac{1}{1+(u/c)^2}\right)^{\frac{1}{2}} = -\frac{\theta}{(\gamma c)^2}u_\alpha := -\Theta u_\alpha.$$

Now, we can evaluate the Jacobian matrix for $\boldsymbol{u} \to \boldsymbol{u}'$

$$J_{\boldsymbol{u}'}(\boldsymbol{u}) = \begin{pmatrix} \cos\theta - \Theta f_1 u_x & \sin\theta - \Theta f_1 u_y & -\Theta f_1 u_z \\ -\sin\theta - \Theta f_2 u_x & \cos\theta - \Theta f_2 u_y & -\Theta f_2 u_z \\ 0 & 0 & 1 \end{pmatrix} \tag{6.6}$$

where

$$\begin{cases} f_1 = -u_x\sin\theta + u_y\cos\theta \\ f_2 = -u_x\cos\theta - u_y\sin\theta \end{cases} \tag{6.7}$$

By calculating the norm of the determinant from the Jacobian matrix defined in equation (6.6) and using equation (6.7) it is possible to prove that the Boris solver is a volume preserving algorithm as

$$|\det(J_{\boldsymbol{u}'}(\boldsymbol{u}))| = \cos^2\theta + \sin^2\theta = 1.$$

6.1.3 Particle counting

The aim of this work is to study the GCR fluence profile produced by a given magnetic field configuration. The GCR propagation through the MC implies to generate an isotropic incident particle flux. Since the simulation space is a rectangular prism, particles enter through its side faces of area A, therefore the geometrical factor of each face is $A\pi$. As mentioned in Section 2.1, the differential incident GCR flux is expressed by

$$J^{(in)}(E) = \frac{1}{\pi A}\frac{dN}{dt\,dE} \tag{6.8}$$

where dN is the number of particles with energy dE crossing the surface A in the time dt. The time integral of equation (6.8) gives the incident particle differential fluence

$$F^{(in)} = \int_0^\infty dt\, J^{(in)}(E) = \frac{1}{\pi A}\frac{dN}{dE}. \tag{6.9}$$

The particle distribution function $f(\boldsymbol{x}, \boldsymbol{p})$, defined as the number of particles in the position $\boldsymbol{x}$ with momentum $\boldsymbol{p}$ in the phase-space volume element $d^3x\, d^3p$, can be expressed in terms of the differential flux

$$f(\boldsymbol{x}, \boldsymbol{p}) = \frac{dN}{p^2\, d^3x\, d\Omega\, dp} = \frac{v\, dN}{p^2\, d^3x\, d\Omega\, dE} = \frac{J(E)}{p^2}.$$

For an incident particle isotropic distribution the differential flux is

$$J(E) = \frac{v}{4\pi}\frac{dN}{d^3x dE} \tag{6.10}$$

The omnidirectional particle differential fluence in the volume element d^3x as a function of energy is given by the time integral of equation (6.10)

$$F(E) = \int_0^\infty dt\, J(E) = \int_0^\infty dt\, \frac{v}{4\pi}\frac{dN}{d^3x\, dE}. \tag{6.11}$$

Starting from these definitions is possible to write down all the discrete quantities that are implemented in the TP simulation to compute the final fluence variation profile. If N_E particles with unit weight and energies $E \in [E, E + \Delta E]$ are injected into the simulation space through the surface $A = 2(x_{\max} - x_{\min})L_z + 2(y_{\max} - y_{\min})L_z$, where L_z is the length of the box in z direction, the total omnidirectional differential fluence at

the boundaries defined in equation (6.9) can be written as

$$F^{(in)} = \frac{N_E}{\pi A \Delta E}. \tag{6.12}$$

Regarding the volume differential fluence computed in each cell, equation (6.11) can be written as

$$F_{ij}(E) = \frac{\sum_{k=1}^{N_{ij,E}} n_{ij,k} v_k \Delta t}{4\pi \Delta x \Delta y L_z \Delta E} \tag{6.13}$$

where $n_{ij,k}$ is the number of points along the k-th particle trajectory with integration time step Δt multiplied by its own velocity v_k. $N_{ij,E}$ is the number of particles crossing the cell $(x, y) \in [x_i, x_i + \Delta x] \times [y_j, y_j + \Delta y]$ with energy $E \in [E, E + \Delta E]$. In order to compute correctly the total number of particle-trajectory points inside each cell, the time step must satisfy the condition $\Delta t < \min(\Delta x, \Delta y)/v$, that prevents particles from skipping the cell without being counted. In order to set the same time step for all particles, in the following we use this condition replacing v with the speed of light c, thus $\Delta t < \min(\Delta x, \Delta y)/c$. Finally, the proper differential fluence variation in the ij-th cell in percentage of the incident fluence is obtained by combining the equations (6.12) and (6.13) as follows

$$\Delta F_{ij}(E) = \frac{F_{ij}(E) - F^{(in)}(E)}{F^{(in)}(E)} = \frac{\sum_{k=1}^{N_{ij,E}} n_{ij,k} v_k (x_{\max} - x_{\min} + y_{\max} - y_{\min}) \Delta t}{2 N_E \Delta x \Delta y}. - 1 \tag{6.14}$$

In order to compute the energy-averaged value of $\Delta F_{ij}(E)$ is necessary to take into account the contribution of all particle energies

$$\Delta F_{ij} = \frac{F_{ij} - F^{(in)}}{F^{(in)}} = \frac{\sum_{k=1}^{N_{ij}} n_{ij,k} v_k (x_{\max} - x_{\min} + y_{\max} - y_{\min}) \Delta t}{2 N \Delta x \Delta y} - 1 \tag{6.15}$$

where N_{ij} is the total number of particles passing through the ij-th cell and N is the total number of simulated particles.

6.2 Scheme of the program

The main steps of the Monte Carlo simulation are summarized in this section:

1) the magnetic field map from the GS reconstruction program is imported;

2) the number of cells $n \times n$ in which the simulation space is divided is defined as

$$n = \lfloor (x_{\max} - x_{\min}) / \boldsymbol{V}_{HT} \cdot \boldsymbol{x}' / t_{sample} \rfloor, \tag{6.16}$$

where $\boldsymbol{x}'$ is the direction along which a S/C crosses the MC and t_{sample} is a sampling time in seconds;

3) cell dimensions Δx, Δy and time step $\Delta t = 0.05 \times \frac{\min(\Delta x, \Delta y)}{c}$ are initialized;

4) individual particles are injected at position $(x_0, y_0, 0)$ where the x_0 or the y_0 coordinate is selected on one of the rectangular box boundaries, with velocity (v_{x0}, v_{y0}, v_{z0}) correctly weighted with the Lambert factor;

5) in order to integrate particle trajectories the relativistic Boris solver is used. The stopping condition for a particle trajectory after m iterations is given by $x(m\Delta t) < x_{\min}$ or $x(m\Delta t) > x_{\max}$ or $y(m\Delta t) < y_{\min}$ or $y(m\Delta t) > y_{\max}$;

6) the set of particle trajectories is stored in a dedicated database;

7) the particle counting procedure defined by (6.15) for each cell and for all energies is carried out and results are stored in a matrix ΔF;

8) steps 4) and 5) are iterated for the total number of particles N and the fluence variation matrix ΔF is stored.

The procedure is repeated M times.

6.3 The August 2, 2016 Forbush decrease

As mentioned above, three FDs were observed on board LPF. The FD dated August 2, 2016 is presented here as a case study. The evolution

of the event is determined by the passage of an ICME. For this event it was possible to recognize the MC signature from IMF and plasma *in situ* observations and the GS reconstruction was applied (Chapter 5). In this section, the Monte Carlo simulation results for this event are presented.

The August 2, 2016 FD observed on board LPF (see Figure 6.2) is the result of the modulation due to two different magnetic regions within the ICME. The first, observed on August 2, 2016 from 14:00 UT through 20:10 UT, consists of an enhanced IMF fluctuating around constant value. The effect on GCRs is a sharp flux decrease of $6.4 \pm 1\%$ constituting the first step of the FD. The second magnetic region presents a smooth rotation in the IMF components lasting about seven hours, from August 2, 2016 at 20:10 UT through August 3, 2016 at about 3:00 UT, ascribable to the transit of the MC studied in Chapter 5. Correspondingly, the GCR flux shows a second decrease of amplitude $2.6 \pm 1\%$. Although the FD commencement appears correlated with the passage of the enhanced IMF region, we focused on the variation associated with the MC passage as its magnetic configuration can be reconstructed on a large scale. The frame of reference of the simulation space is defined according to the GS reconstruction frame, moving with the MC at a constant HT velocity towards the Earth. Particles involved in the simulation are only protons, given that they represent roughly the 90% of the particle composition of GCRs in the inner heliosphere. Particle energies are sampled from the differential proton flux estimated at the beginning of the August 2, 2016 MC passage. The parameterization of the energy spectrum is carried out using the function appearing in equation (3.5) in the energy interval 70 MeV-100 GeV. The coefficients are set at $A = 18000$, $b = 1.25$, $\alpha = 3.66$ and $\beta = 0.869$ as shown in Figure 6.3, on the basis of the AMS-02 experiment observations averaged over the BR 2496 (Aguilar et al., 2018). This choice is made since the dip of the FD was observed when the GCR proton flux assumed the average value observed during the BR, as it can be noticed in Figure 6.2, where dashed lines indicate the MC passage.

The August 2, 2016 MC has a dimension of $V_{HT}\Delta t \sim 0.07$ AU where $V_{HT} = 414.6$ km s^{-1} and $\Delta t \sim 7$ hr. For sake of comparison, in Table 6.1 are reported the Larmor radii of protons for typical GCR particle energies and magnetic field values observed at the passage of the MC. In this case, high-energy-particle Larmor radii are of the same order of the MC size and thus the guiding center approximation would be inadequate since we consider the whole proton spectrum in the energy range 70 MeV-100 GeV. The integration of the motion equation for an isotropic flux entering the MC, leads to a variety of trajectories. A selected sample of

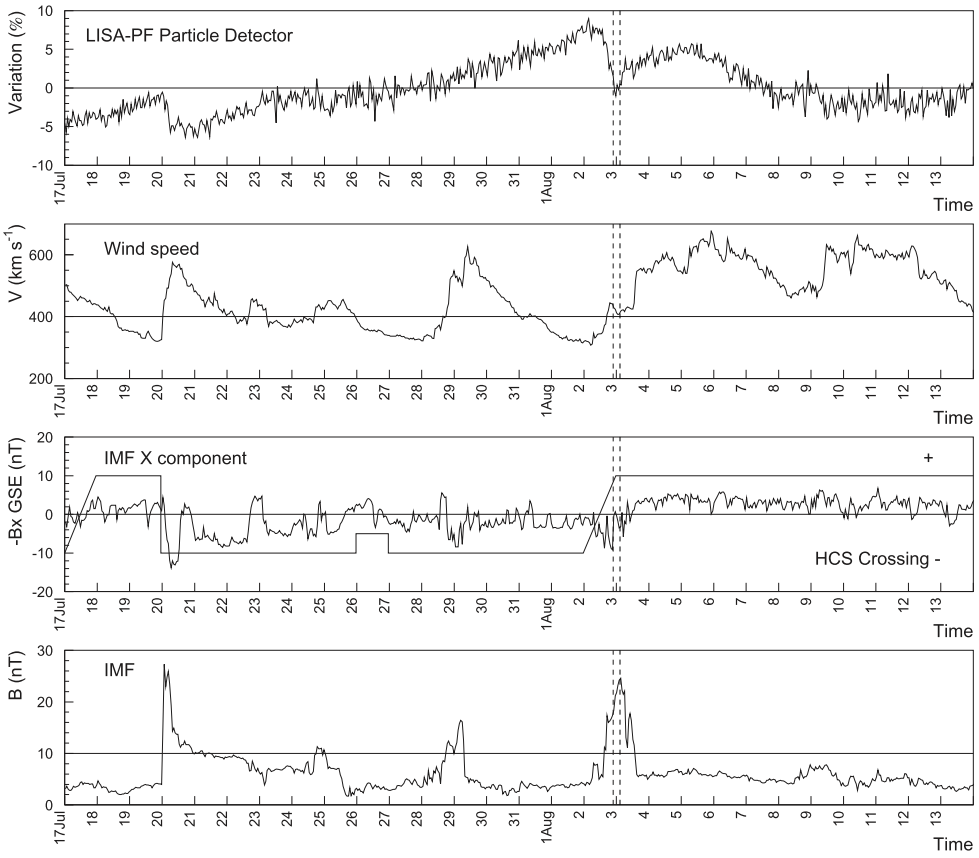

Figure 6.2 Same as Figure 4.3 for the BR 2496 (July 17-August 13, 2016). The MC transit is marked by vertical dashed lines.

trajectories covered by particles of different energies is displayed in Figure 6.4 ($\sim$ 100 MeV top left, $\sim$ 1 GeV top right, $\sim$10 GeV bottom left and $>$ 50 GeV bottom right). From the top-left panel of this figure, it can be observed that even particles with lowest energies (i.e. smallest Larmor radii) can reach the core region of the MC and can pass through it, or alternatively they can undergo mirroring due to the increasing magnetic field. On the other hand, if a low energy particle starts to follow an external magnetic field line, it would not be able to reach the inner MC region. In general lower energy particles can reach or not the inner region of the MC depending on the local structure of the magnetic field (gradient and curvature) and the velocity component perpendicular to the field lines. This process is at the origin of the particle drift velocity, causing the intensity decrease observed in the inner region of the MC. Indeed, the highest energetic particles (bottom-left and bottom-right panels in

Table 6.1. Larmor radii of protons for typical values of the GCR energy and of the magnetic field within the MC dated August 2, 2016.

E (GeV)	B (nT)	r_L (AU)	E (GeV)	B (nT)	r_L (AU)
0.1	5	0.002	10	5	0.049
	15	6.59×10^{-4}		15	0.016
	25	3.95×10^{-4}		25	0.010
1	5	0.0075	100	5	0.45
	15	0.0025		15	0.15
	25	0.0015		25	0.09

Figure 6.4) have Larmor radii that are comparable with respect to the size of the structure and can easily pass through the MC core.

In order to perform a comparison between Monte Carlo simulation outcomes and LPF observations, the simulation space is divided in a 7×7 grid, according to equation (6.16) with $t_{sample} = 3600$ s $= 1$ hr, in order to reconcile the simulated fluence with the time data binning used for LPF data. The resulting cell dimensions are: $\Delta x = 0.0077$ AU and $\Delta y = 0.0071$ AU. By using the trajectories obtained from the particle propagation, the fluence ΔF_{ij} defined in equation (6.15) is calculated in each cell and the result is shown in Figure 6.5 (left panel).

Since the fluence is computed on the basis of the simulated particle trajectories, its calculation is not statistically independent, especially when carried out on close cells. For instance, the motion of the same

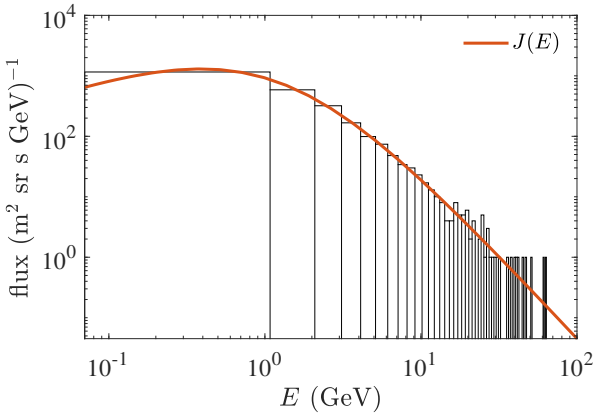

Figure 6.3 Energy spectrum used in the TP simulation. The red solid line is the $J(E)$ parametric function defined in equation 3.5.

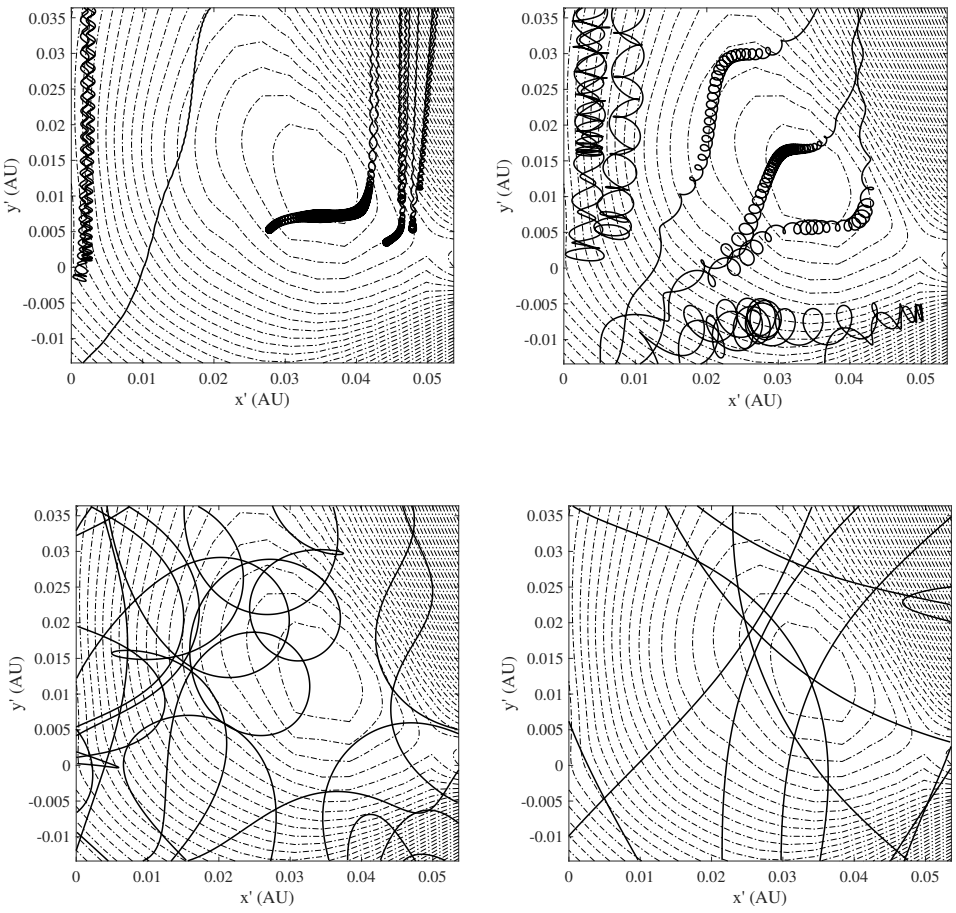

Figure 6.4 Example of TP trajectories across the MC. Trajectories are projected on the $x'y'$ plane for four different energy intervals: $\sim$ 100 MeV (top-left), $\sim$ 1 GeV (top-right), $\sim$ 10 GeV (bottom-left) and $\geqslant$ 50 GeV (bottom-right). The dashed lines are the level curves of the vector potential $A(x', y')$.

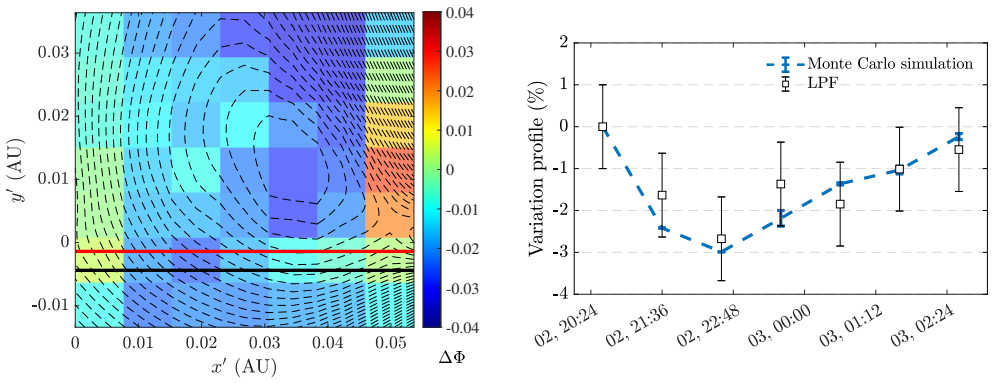

Figure 6.5 Left: fluence variation matrix for the August 2, 2016 MC. The dashed lines are the level curves of the vector potential $A(x', y')$. The straight black line represents the LPF S/C path through the MC at $y' = -4.4 \times 10^{-3}$ AU. The straight red line represents the Earth path through the MC at $y' = -1.4 \times 10^{-3}$ AU. Right: comparison between the LPF observations and the fluence variation profile from the TP simulations. The statistical error of LPF observations is 1% and those of TP simulation are evaluated according to the equation (6.17).

trapped particle can increase the counts of subsequent cells passing from one to the other several times. Hence, counts on different cells are often based on the same trajectory and the count is not statistically independent along with the grid. In order to deal with independent fluence samples, M independent executions of the program with different initial seeds of the Monte Carlo simulation were carried out to evaluate the average fluence variation in each cell. The fluence standard error on each cell was calculated as follows:

$$SE_{ij} = \frac{\sigma_{ij}}{\sqrt{M}} \tag{6.17}$$

where σ_{ij} indicates the standard deviation on the M different fluence values in the cell ij. The fluence computed over each cell is displayed in Figure 6.5 (left panel). The highest fluence values are reached at the MC boundaries where open field lines are present. On the other hand, the fluence reach its minimum at the center of the MC ($x' = 0.035$ AU, $y' = 0.013$ AU) where a variation of about 4% is observed. The LPF path across the MC is indicated in the left panel of Figure 6.5 by the black solid line. In the same figure it is reported the Earth path through the MC located at $y' = -1.4 \times 10^{-3}$ AU and indicated by the red solid line. The space bins explored by LPF and the Earth during the MC

crossing are the same. The GCR fluence variation profile generated by the August 2, 2016 MC along the LPF path is shown in Figure 6.5 (right panel) in comparison with GCR observations gathered with the PD on board LPF. An excellent agreement between model and measurements is observed within error bars. The observed FD amplitude at the MC passage is $2.6 \pm 1\%$ and the TP simulation returns an amplitude of 3%.

Since particle energies are known, it is possible to study the energy dependence of the simulated MC-driven FD using the definition of fluence appearing in equation (6.14). By defining the initial omnidirectional differential fluence $F_i(E)$ and the differential fluence in the cell associated with the dip of the FD along the LPF path $F_d(E)$, we evaluate the variation

$$\Delta F_{id}(E) = \frac{F_i(E) - F_d(E)}{F_i(E)}. \tag{6.18}$$

The fluence variation produced by the MC for different energies is reported in Figure 6.6. As expected, for increasing energies the modulation effect due to the MC passage decreases. Particles in the energy interval 3-10 GeV present a fluence variation below 1% and those with energies > 10 GeV do not show significant variations, thus the modulation due to the MC transit results to be uneffective at these energies. In order to compare the simulation results with ground-based observations, we consider the hourly pressure corrected count rates of several NMs (see Table

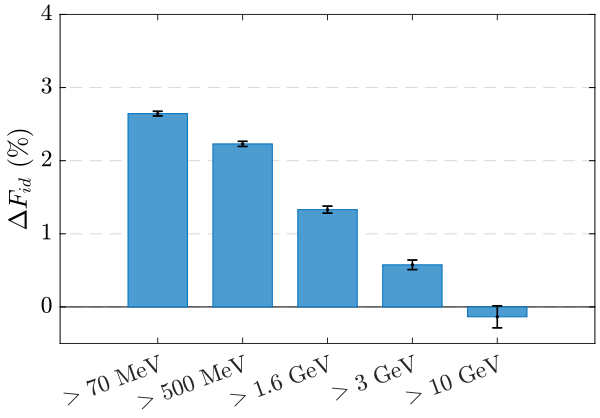

Figure 6.6 Simulated differential fluence variation of GCRs at the dip of the FD with respect to the incident fluence for different energy intervals. Percentage variations are computed as indicated in equation (6.18).

Table 6.2. Geographic coordinates, altitude and vertical cutoff rigidities of five NM stations. The total FD amplitude and the decrease amplitude associated with the MC are reported for the 2016 August 2 event.

Station	Geographic coordinates	Altitude (m)	Vertical cutoff rigidity (GV)	FD ampl. (%)	MC decrease ampl. (%)
DOMC	75.06° S, 123.2° E	3233	< 0.01	4	2
South Pole	90.0° S, N/A	2820	0.1	3.6	1.5
Newark	39.7° N, 75.8° W	50	2.4	2.1	< 1
Rome	41.9° N, 12.5° E	s.l.	6.27	1.4	< 1
Mexico City	19.3° N, 260.8° E	2274	8.2	1.1	< 1

6.2) obtained from the neutron monitor database[1]. They have been normalized with respect to the average value over the pre-decrease period from 07:00 UTC to 11:00 UTC on August 2, 2016. Data are shown in Figure 6.7. The FD was observed with few percents amplitudes by the DOMC, South Pole and Newark NMs, having low cutoff rigidity (energy) of 0.01 GV (53 keV), 0.1 GV (5 MeV) and 2.4 GV (1.6 GeV), respectively. On the other hand, no significant decrease was recorded by higher cutoff rigidity (energy) NMs, such as Rome, 6.27 GV (5.4 GeV) and Mexico City, 8.2 GV (7.3 GeV). The effect ascribable to the MC passage is a decrease of 2% at DOMC and 1.5% at South Pole, that are slightly lower than expected from the simulation at comparable energies. Indeed, despite their low cutoff rigidity, the lower energy that can be recorded by these stations at ground is the 500 MeV associated with the atmospheric cutoff. More equatorial stations such as Rome and Mexico City show a decrease $< 1\%$ as expected from the simulation. However, ground-based observations are affected by Earth rotation and geomagnetic effects in addition to the NM viewing directions that are not included in this analysis.

The numerical model proposed in this thesis allows to properly reproduce the time profile and the amplitude of the MC-driven part of a FD. Low energy particle observations carried out with the PD on board LPF are more affected being the decrease larger than those from ground-based

[1] www.nmdb.eu

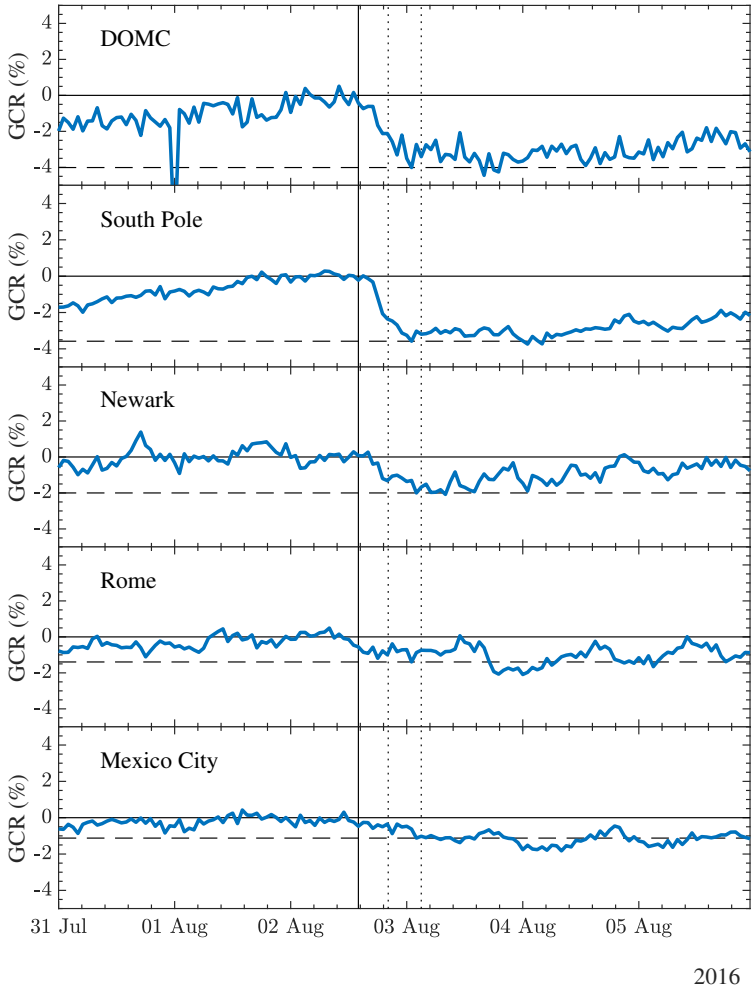

Figure 6.7 GCR intensity variations gathered by five NM stations for the 2016 August 2 event. The vertical solid line is the start time of the ICME transit in L1 and the vertical dotted lines are the MC boundaries. The horizontal solid line along zero represents the average pre-decrease count-rate level taken as a reference value to compute FD amplitudes (horizontal dashed lines).

observations. From the physical point of view, GCR FDs are usually interpreted in the framework of particle transport. As a matter of fact, the observation of a FD is due to a lower GCR density inside the MC, to which the particle excess is limited by its magnetic configuration. A cosmic ray from the MC edge can move into the magnetic structure changing its guiding center in response to magnetic field gradient and curvature and then drift away further inside crossing the field lines to head towards the inner MC region or drift outside following external field lines. The diffusion of particles perpendicularly to the mean magnetic field includes two processes: 1) field line crossings due to scattering or drift and 2) random walk along field lines (Jokipii, 1987; Kong et al., 2019). In the method proposed in this thesis the only term contributing to the particle propagation inside the closed MC structure are gradient and curvature drifts. Our result suggests that for the analyzed MC a fraction of low-energy particles do leak into the MC (see Figure 6.6), remaining trapped and/or pushed out by external closed field lines. Moreover, the low variance of the magnetic field inside the cloud, i.e. small magnetic fluctuations, does not favor a large-scale cross-field transport through diffusion process or random walk. Hence, we suggest that gradient and curvature drifts are mainly responsible for GCR FDs originated by large-scale closed MC structure.

Conclusions

A PD on board the ESA mission LPF allowed for the detection of GCR > 70 MeV n^{-1} during the descending phase of the solar cycle N. 24. The first part of the thesis focuses on the study of the GCR short-term flux variations observed with the PD on board LPF during the mission elapsed time. It is found that the average duration of the GCR flux depressions is 9.2 ± 5.0 day. Decrease, plateau, and recovery periods last in average 2.8 ± 2.0 day, 1.3 ± 1.2 day, and 5.1 ± 3.8 day respectively, while the average depression intensity is of $5.1 \pm 2.5\%$. Many of the identified depressions in the GCR flux, thirty-eight out of forty-five, are defined as recurrent variations and are associated with the interaction between GCRs and high-speed streams from coronal holes and/or CIRs. Coronal holes are corotating, long-living and quasi-stationary plasma structures in the atmosphere of the Sun where high-speed solar-wind streams are originated. The structure of an high-speed stream is generally characterized by a distinctive temporal behavior in the interplanetary parameters and when it interact with GCRs the isotropic particle intensity is depressed. The recurrence of the GCR flux depressions is obtained by analyzing the quasi-periodicities in the GCR count rate. In order to investigate the time-frequency modulation present in the GCR dataset the data analysis is carried out through the HHT. The first step of the HHT is to extract the signal components, which form a complete and nearly orthogonal basis for the original dataset, through the EMD. These components are called intrinsic mode functions and are characterized by a time dependence in both amplitude and frequency. For the LPF dataset ten intrinsic mode functions and a residue are found. From a statistical analysis, intrinsic mode functions 4-10 are significant with respect to the Gaussian white noise and more than 90% of the signal energy budget is contained in the modes 6-10. Intrinsic mode functions 6-8 have mean periods of 7.0 ± 2.8, 13.2 ± 2.8 and 27.9 ± 3.6 day, respectively, and appear to be associated with the 27-day solar-rotation period and higher harmonics. The residue of the EMD represents the increasing long-term

data trend observed during the LPF mission elapsed time that is anti-correlated with the decreasing solar activity, because of the reduced effect of the interplanetary disturbances acting as barriers on GCRs.

In order to better understand the relation of the quasi-periodicities with the interplanetary physical drivers, the HSA has been performed. It returns the time-frequency diagram where the frequency modulation as a function of time can be evaluated. The high energy part of the spectrum during BRs 2495-2498 is found to correspond to the 27 day periodicity, which is found to be linked to the passage of one CHSS or CIR corotating with the Sun during each BR. During BRs 2499-2502 a high energy is observed also along the 1/13.5 day^{-1} frequency line, consistent with the number of CHSSs or CIRs observed during this period of time, i.e. two disturbances for each BR. Thus, in this contest the HHT represents a powerful technique allowing for the investigation of instantaneous amplitudes and frequencies of the GCR modulation and to get a deeper insight into the physics of the interaction between GCRs and solar wind disturbances. A forthcoming application of the HHT to solar wind parameters and IMF is planned in order to investigate the characteristics of their interaction with GCRs at different time-scales.

A number of twenty-nine GCR variations associated with transient solar-wind disturbances are observed in the LPF data and their association with interplanetary processes is provided. In particular, transient GCR flux variations observed on board LPF were divided in two classes: the first included flux variations with duration < 2 day and intensities $> 2\%$.

Out of twenty-three transient variation of this first class, seventeen resulted to be depressions and six peaks. The majority of depressions are associated with HCS crossings while the peaks are observed at plasma compression regions between closely spaced CHSSs when MBs are present, suggesting that low energy cosmic rays ($\sim$ 70 MeV n^{-1}) are confined through particle trapping and/or reflection.

The second class of transient GCR flux variation is represented by FDs associated with ICMEs. ICMEs are the interplanetary counterparts of eruptive phenomena in the solar corona characterized by the ejection of billions of tons of plasma material carrying an embedded magnetic field generally stronger than the background solar wind IMF. ICMEs are generally preceded by a region of compressed plasma with turbulent magnetic fields called sheath. Fast ICMEs are also accompanied by interplanetary shocks. The ICME is a plasma structure magnetically connected to the Sun, characterized by low values of temperature and plasma-beta. When the magnetic field presents a smooth rotation, the

inner part of the ICME has a well-known topology and it is called MC. The overall effect on GCR particles of the enhanced magnetic field and the closed configuration of the field lines is a depression in the GCR intensity. A "classical" FD, measured when both the shock/sheath region and the MC region cross the observer, shows a two-step profile. The first step consists of a sudden GCR intensity decrease associated with the interplanetary shock and the subsequent turbulent sheath region, while the second step is ascribed to the MC passage. Although the association of FDs with ICME passage in L1 is known, the underlying physical mechanisms need to be better understood. Hence, we have studied the GCR flux energy-dependent response to the passage of these structures by comparing observations above 70 MeV n^{-1} gathered with LPF and NM data observed at different geographic latitudes.

Three FDs were observed on LPF with commencements observed on July 20, 2016, August 2, 2016 and May 27, 2017. The LPF proton-dominated integral flux maximum decreases above 70 MeV n^{-1} are observed to vary from about 5% to 9% for the three events. NM count-rate variations at higher energies range between 1% and 3% for these three events. In particular, The August 2, 2016 FD amplitude in the LPF hourly count rates at energies > 70 MeV n^{-1} was found to be of 9% with respect to a pre-decrease reference value. A $6.4 \pm 1\%$ variation was observed in concomitance with the passage of the enhanced magnetic field region of the ICME, whereas an additional $2.6 \pm 1\%$ was observed during the following MC transit. NMs recorded lower FD amplitudes of the order of few percents (from 4% at DOMC NM to about 1% at Rome and Mexico City NMs because of the higher cut-off rigidities of the latter), part of which can be attributed to the effect of the MC only for DOMC and South Pole NMs for an amount of 2% and 1.5 %, respectively. In order to investigate the effect of the interplanetary perturbations in modulating the GCR flux, a new approach has been developed. The method proposed in this thesis combines:

1. space- and ground-based GCR observations;
2. the magnetic field large-scale configuration reconstructed from *in situ* solar wind and IMF data of the MC observed at L1 from August 2, 2016 at 20:10 UT through August 3, 2016 at 03:00 UT;
3. the realization of a suited TP simulation over the obtained MC configuration to reproduce the August 2, 2016 FD.

To my knowledge, this work represents the first attempt to merge two numerical techniques: the GS reconstruction of a large-scale MC and

a Monte Carlo simulation aimed to investigate the resulting GCR flux modulation.

The GS reconstruction is an advanced data analysis technique that allows for retrieving a realistic MC topology from single S/C data. From the MHD theory, when the force balance between the pressure gradient and the magnetic force holds, the GS equation is valid and can be applied in order to estimate the MC configuration numerically. The August 2, 2016 MC is reconstructed by using Wind S/C 1-minute resolution data. The dimension of the reconstructed MC is approximately of 0.07 AU. The core of the structure is found to be around the point of coordinates $x' = 0.035$ AU and $y' = 0.013$ AU with respect to the reconstruction plane, where the axial magnetic field reaches its maximum, $B_z = 25.3$ nT. The z-axis orientation with respect to the GSE is of $\theta = 17.3 \pm 1.7°$ and $\phi = 53.9 \pm 2.9°$, where θ and ϕ are the latitude and longitude angles respectively.

The GS reconstruction plane and the direction along the invariant z-axis define the rectangular-prism geometry of the simulation space where the particle propagation is then performed. The initial proton energy spectrum adopted in the simulation is obtained with a parameterization extended to 70 MeV n^{-1} of the AMS-02 observations averaged during the BR 2496 (July 17, 2016-August 13, 2016). The Monte Carlo simulation is then performed in the TP approximation by integrating all the particle-motion equations in order to obtain the a complete set of full-trajectories. Then, the particle fluence variation at the MC passage is calculated along the LPF S/C path, found to lie along the $y = -4.4 \times 10^{-3}$ AU line on the reconstruction plane. The amplitude of the simulated FD is found to be 3%, fully consistent with the $2.6 \pm 1\%$ observed with LPF and the time profile returned by the simulation shows an excellent agreement with the LPF data trend within error bars. A study of the energy dependence of the GCR flux response to the MC passage reveals that the modulation due to the MC decreases at higher energies as confirmed by NM observations.

From the physical point of view, GCR FDs are usually interpreted in the framework of particle transport through the magnetic field and the presence of a FD is ascribed to the lower GCR density in the inner region of the MC. The study of the effect of ICME and MC passage on GCR flux is extensively carried out in the literature with theoretical and numerical models. The approach suggested here represents a step-forward with respect to analytical flux-rope models, especially because the GS reconstruction relies on a data-based algorithm and therefore, takes into account all the local features of the measured IMF. It

is worthwhile to point out that our results (amplitude and time profile of the August 2, 2016 FD) are obtained by integrating the TP motion through the static MC configuration without including any other physical process (e.g. random-walk-like diffusion and/or MC expansion). Indeed, the small magnetic field fluctuations observed in this MC do not favor the cross-field transport through random-walk-like diffusion with respect to particle drifts. The excellent agreement between simulation results and observations suggests that the closed configuration of MCs limits the GCR access, depending on their energy, causing gradient and curvature drifts that can either trap or push out low-energy particles. Thus, this represents the main physical process involved in the generation of the considered FD by a large-scale MC. A deeper investigation by using the method proposed in this thesis is still ongoing in order to study how ICMEs having different properties (e.g. velocity of propagation, size, MC configuration, etc.) affect the heliospheric propagation of GCRs.

Bibliography

Abbott, B. P., Abbott, R., Abbott, T., Abernathy, M., Acernese, F., Ackley, K., Adams, C., Adams, T., Addesso, P., Adhikari, R., et al. (2016). Observation of gravitational waves from a binary black hole merger. *Physical review letters*, 116(6):061102.

Adriani, O., Barbarino, G., Bazilevskaya, G., Bellotti, R., Boezio, M., Bogomolov, E., Bonechi, L., Bongi, M., Bonvicini, V., Borisov, S., et al. (2011). Observations of the 2006 december 13 and 14 solar particle events in the 80 mev n–1-3 gev n–1 range from space with the pamela detector. *The Astrophysical Journal*, 742(2):102.

Aguilar, M., Alcaraz, J., Allaby, J., Alpat, B., Ambrosi, G., Anderhub, H., Ao, L., Arefiev, A., Azzarello, P., Babucci, E., et al. (2002). The alpha magnetic spectrometer (ams) on the international space station: Part i–results from the test flight on the space shuttle. *Physics Reports*, 366(6):331–405.

Aguilar, M., Cavasonza, L. A., Alpat, B., Ambrosi, G., Arruda, L., Attig, N., Aupetit, S., Azzarello, P., Bachlechner, A., Barao, F., et al. (2018). Observation of fine time structures in the cosmic proton and helium fluxes with the alpha magnetic spectrometer on the international space station. *Physical review letters*, 121(5):051101.

Amaro-Seoane, P., Audley, H., Babak, S., Baker, J., Barausse, E., Bender, P., Berti, E., Binetruy, P., Born, M., Bortoluzzi, D., et al. (2017). Laser interferometer space antenna. *arXiv preprint arXiv:1702.00786*.

Armano, M., Audley, H., Auger, G., Baird, J., Bassan, M., Binetruy, P., Born, M., Bortoluzzi, D., Brandt, N., Caleno, M., et al. (2016). Sub-femto-g free fall for space-based gravitational wave observatories: Lisa pathfinder results. *Physical review letters*, 116(23):231101.

Armano, M., Audley, H., Auger, G., Baird, J., Binetruy, P., Born, M., Bortoluzzi, D., Brandt, N., Bursi, A., Caleno, M., et al. (2015). A

strategy to characterize the lisa-pathfinder cold gas thruster system. In *Journal of Physics: Conference Series*, volume 610, page 012026. IOP Publishing.

Armano, M., Audley, H., Auger, G., Baird, J., Binetruy, P., Born, M., Bortoluzzi, D., Brandt, N., Bursi, A., Caleno, M., et al. (2017). Charge-induced force noise on free-falling test masses: results from lisa pathfinder. *Physical review letters*, 118(17):171101.

Armano, M., Audley, H., Baird, J., Bassan, M., Benella, S., Binetruy, P., Born, M., Bortoluzzi, D., Cavalleri, A., Cesarini, A., et al. (2018). Characteristics and energy dependence of recurrent galactic cosmic-ray flux depressions and of a forbush decrease with lisa pathfinder. *The Astrophysical Journal*, 854(2):113.

Armano, M., Audley, H., Baird, J., Benella, S., Binetruy, P., Born, M., Bortoluzzi, D., Castelli, E., Cavalleri, A., Cesarini, A., et al. (2019). Forbush decreases and$<$ 2 day gcr flux non-recurrent variations studied with lisa pathfinder. *The Astrophysical Journal*, 874(2):167.

Arunbabu, K., Antia, H., Dugad, S., Gupta, S., Hayashi, Y., Kawakami, S., Mohanty, P., Nonaka, T., Oshima, A., and Subramanian, P. (2013). High-rigidity forbush decreases: due to cmes or shocks? *Astronomy & Astrophysics*, 555:A139.

Boella, G., Gervasi, M., Mariani, S., Rancoita, P., and Usoskin, I. (2001). Evidence for charge drift modulation at intermediate solar activity from the flux variation of protons and α particles. *Journal of Geophysical Research: Space Physics*, 106(A12):29355–29362.

Bogomolov, E., Lubyanaya, N., Romanov, V., Stepanov, S., and Shulakova, M. (1979). A stratospheric magnetic spectrometer investigation of the singly charged component spectra and composition of the primary and secondary cosmic radiation. In *International Cosmic Ray Conference*, volume 1, page 330.

Boris, J. P. (1970). Relativistic plasma simulation-optimization of a hybrid code. In *Proc. 4th Conf. Num. Sim. Plasmas*, pages 3–67.

Burlaga, L., Sittler, E., Mariani, F., and Schwenn, a. R. (1981). Magnetic loop behind an interplanetary shock: Voyager, helios, and imp 8 observations. *Journal of Geophysical Research: Space Physics*, 86(A8):6673–6684.

Caballero-Lopez, R. and Moraal, H. (2004). Limitations of the force field equation to describe cosmic ray modulation. *Journal of Geophysical Research: Space Physics*, 109(A1).

Cane, H. and Richardson, I. (2003). Interplanetary coronal mass ejections in the near-earth solar wind during 1996–2002. *Journal of Geophysical Research: Space Physics*, 108(A4).

Cane, H., Richardson, I., and Wibberenz, G. (1995). The response of energetic particles to the presence of ejecta material. In *International Cosmic Ray Conference*, volume 4, page 377.

Cane, H. V. (2000). Coronal mass ejections and forbush decreases. In *Cosmic Rays and Earth*, pages 55–77. Springer.

Castellina, A. (2019). Highlights from the pierre auger observatory and prospects for augerprime. In *36th International Cosmic Ray Conference (ICRC2019)*, volume 36.

Chapman, S. and Bartels, J. (1940). Geomagnetism. *Oxford University Press*.

De Hoffmann, F. and Teller, E. (1950). Magneto-hydrodynamic shocks. *Physical Review*, 80(4):692.

Diaz-Aguilo, M., Lobo, A., and García-Berro, E. (2011). Neural network interpolation of the magnetic field for the lisa pathfinder diagnostics subsystem. *Experimental Astronomy*, 30(1):1–21.

Dorman, L. and Yanke, V. (1981). The coupling functions of nm-64 neutron supermonitor. In *International Cosmic Ray Conference*, volume 4, page 326.

Dumbović, M., Heber, B., Vršnak, B., Temmer, M., and Kirin, A. (2018). An analytical diffusion–expansion model for forbush decreases caused by flux ropes. *The Astrophysical Journal*, 860(1):71.

Dunai, T. J. (2010). *Cosmogenic Nuclides: Principles, concepts and applications in the Earth surface sciences*. Cambridge University Press.

Ferreira, S. and Potgieter, M. (2004). Long-term cosmic-ray modulation in the heliosphere. *The Astrophysical Journal*, 603(2):744.

Forbush, S. E. (1937). On the effects in cosmic-ray intensity observed during the recent magnetic storm. *Physical Review*, 51(12):1108.

Giacalone, J., Jokipii, J. R., and Kóta, J. (2002). Particle acceleration in solar wind compression regions. *The Astrophysical Journal*, 573(2):845.

Gil, A. and Alania, M. V. (2016). Energy spectrum of the recurrent variation of galactic cosmic rays during the solar minimum of cycles 23/24. *Solar Physics*, 291(6):1877–1886.

Gil, A., Asvestari, E., Usoskin, I., and Kovaltsov, G. (2017). Heliospheric modulation of galactic cosmic rays: Effective energy of ground-based detectors. *PoS*, page 032.

Gleeson, L. and Axford, W. (1967). Cosmic rays in the interplanetary medium. *The Astrophysical Journal*, 149:L115.

Gleeson, L. and Axford, W. (1968). Solar modulation of galactic cosmic rays. *The Astrophysical Journal*, 154:1011.

Golden, R., Horan, S., Mauger, B., Badhwar, G., Lacy, J., Stephens, S., Daniel, R., and Zipse, J. (1979). Evidence for the existence of cosmic-ray antiprotons. *Physical Review Letters*, 43(16):1196.

Grad, H. and Rubin, H. (1958). Hydromagnetic equilibria and force-free fields. *Journal of Nuclear Energy (1954)*, 7(3-4):284–285.

Grimani, C. (2007a). Constraints on cosmic-ray positron excess and average pulsar parameters. *Astronomy & Astrophysics*, 474(2):339–343.

Grimani, C., Fabi, M., Finetti, N., Tombolato, D., Marconi, L., Stanga, R., Lobo, A., Chmeissani, M., and Puigdengoles, C. (2009). Heliospheric influences on lisa. *Classical and Quantum Gravity*, 26(9):094018.

Grimani, C., Fabi, M., Lobo, A., Mateos, I., and Telloni, D. (2015). Lisa pathfinder test-mass charging during galactic cosmic-ray flux short-term variations. *Classical and Quantum Gravity*, 32(3):035001.

Grimani, C. and Vocca, H. (2005). Solar physics with lisa. *Classical and Quantum Gravity*, 22(10):S333.

Grimani, C. G. (2007b). Parameterization of galactic cosmic-ray fluxes during opposite polarity solar cycles for future space missions.

Gurnett, D., Kurth, W., Burlaga, L., and Ness, N. (2013). In situ observations of interstellar plasma with voyager 1. *Science*, 341(6153):1489–1492.

Hathaway, D. H. (2015). The solar cycle. *Living reviews in solar physics*, 12(1):4.

Hau, L.-N. and Sonnerup, B. U. (1999). Two-dimensional coherent structures in the magnetopause: Recovery of static equilibria from single-spacecraft data. *Journal of Geophysical Research: Space Physics*, 104(A4):6899–6917.

Hess, V. F. (1912). Observations of the penetrating radiation on seven balloon flights. *Physik. Zeitschr*, 13:1084–1091.

Hess, V. F. and Demmelmair, A. (1937). World-wide effect in cosmic ray intensity, as observed during a recent magnetic storm. *Nature*, 140(3538):316.

Hu, Q. and Sonnerup, B. U. (2002). Reconstruction of magnetic clouds in the solar wind: Orientations and configurations. *Journal of Geophysical Research: Space Physics*, 107(A7):SSH–10.

Hu, Q., Zheng, J., Chen, Y., le Roux, J., and Zhao, L. (2018). Automated detection of small-scale magnetic flux ropes in the solar wind: First results from the wind spacecraft measurements. *The Astrophysical Journal Supplement Series*, 239(1):12.

Huang, N. E. (2014). *Hilbert-Huang transform and its applications*, volume 16. World Scientific.

Huang, N. E., Shen, Z., Long, S. R., Wu, M. C., Shih, H. H., Zheng, Q., Yen, N.-C., Tung, C. C., and Liu, H. H. (1998). The empirical mode decomposition and the hilbert spectrum for nonlinear and non-stationary time series analysis. *Proceedings of the Royal Society of London. Series A: Mathematical, Physical and Engineering Sciences*, 454(1971):903–995.

Jokipii, J. (1987). Rate of energy gain and maximum energy in diffusive shock acceleration. *The Astrophysical Journal*, 313:842–846.

Jokipii, J., Levy, E., and Hubbard, W. (1977). Effects of particle drift on cosmic-ray transport. i-general properties, application to solar modulation. *The Astrophysical Journal*, 213:861–868.

Jokipii, J. and Thomas, B. (1981). Effects of drift on the transport of cosmic rays. iv-modulation by a wavy interplanetary current sheet. *The Astrophysical Journal*, 243:1115–1122.

Kivelson, A. (1995). *Introduction to space physics*. Cambridge university press.

Klionski, D., Oreshko, N., Geppener, V., and Vasiljev, A. (2008). Applications of empirical mode decomposition for processing nonstationary signals. *Pattern recognition and image analysis*, 18(3):390.

Kong, X., Guo, F., Chen, Y., and Giacalone, J. (2019). The acceleration of energetic particles at coronal shocks and emergence of a double power-law feature in particle energy spectra. *The Astrophysical Journal*, 883(1):49.

Kota, J. and Jokipii, J. (1983). Effects of drift on the transport of cosmic rays. vi-a three-dimensional model including diffusion. *The Astrophysical Journal*, 265:573–581.

Krittinatham, W. and Ruffolo, D. (2009). Drift orbits of energetic particles in an interplanetary magnetic flux rope. *The Astrophysical Journal*, 704(1):831.

Kuwabara, T., Bieber, J., Evenson, P., Munakata, K., Yasue, S., Kato, C., Fushishita, A., Tokumaru, M., Duldig, M., Humble, J., et al. (2009). Determination of interplanetary coronal mass ejection geometry and orientation from ground-based observations of galactic cosmic rays. *Journal of Geophysical Research: Space Physics*, 114(A5).

Landgraf, M., Hechler, M., and Kemble, S. (2005). Mission design for lisa pathfinder. *Classical and Quantum Gravity*, 22(10):S487.

Laurenza, M., Consolini, G., Storini, M., and Damiani, A. (2015). The weibull functional form for sep event spectra. In *Journal of Physics: Conference Series*, volume 632, page 012066. IOP Publishing.

Laurenza, M., Vecchio, A., Storini, M., and Carbone, V. (2014). Drift effects on the galactic cosmic ray modulation. *The Astrophysical Journal*, 781(2):71.

Mateos, I., Diaz-Aguiló, M., Gibert, F., Grimani, C., Hollington, D., Lloro, I., Lobo, A., Nofrarias, M., and Ramos-Castro, J. (2012). Lisa pathfinder radiation monitor proton irradiation test results. In *Journal*

of Physics: Conference Series, volume 363, page 012050. IOP Publishing.

Mateos, I., Lobo, A., Ramos-Castro, J., Sanjuán, J., Diaz-Aguiló, M., Wass, P., and Grimani, C. (2010). Proton irradiation test on the flight model radiation monitor for lisa pathfinder. In *Journal of Physics: Conference Series*, volume 228, page 012039. IOP Publishing.

McDonald, F. B., Teegarden, B. J., Trainor, J. H., von Rosenvinge, T. T., and Webber, W. R. (1976). The interplanetary acceleration of energetic nucleons. *The Astrophysical Journal*, 203:L149–L154.

Millikan, R. A. and Cameron, G. H. (1926). High frequency rays of cosmic origin iii. measurements in snow-fed lakes at high altitudes. *Physical Review*, 28(5):851.

Möstl, C., Farrugia, C., Miklenic, C., Temmer, M., Galvin, A., Luhmann, J., Kilpua, E., Leitner, M., Nieves-Chinchilla, T., Veronig, A., et al. (2009). Multispacecraft recovery of a magnetic cloud and its origin from magnetic reconnection on the sun. *Journal of Geophysical Research: Space Physics*, 114(A4).

Munakata, K., Yasue, S., Kato, C., Kota, J., Tokumaru, M., Kojima, M., Darwish, A., Kuwabara, T., and Bieber, J. (2006). On the cross-field diffusion of galactic cosmic rays into an icme. In *Advances in Geosciences: Volume 2: Solar Terrestrial (ST)*, pages 115–124. World Scientific.

O'gallagher, J. and Simpson, J. (1967). The heliocentric intensity gradients of cosmic-ray protons and helium during minimum solar modulation. *The Astrophysical Journal*, 147:819.

Papini, P., Grimani, C., and Stephens, S. (1996). An estimate of the secondary-proton spectrum at small atmospheric depths. *Il Nuovo Cimento C*, 19(3):367–387.

Parker, E. N. (1958). Dynamics of the interplanetary gas and magnetic fields. *The Astrophysical Journal*, 128:664.

Parker, E. N. (1965). The passage of energetic charged particles through interplanetary space. *Planetary and Space Science*, 13(1):9–49.

Petukhova, A., Petukhov, I., and Petukhov, S. (2017). Theory of forbush decrease in a magnetic cloud. *PoS*, page 122.

Petukhova, A., Petukhov, I., and Petukhov, S. (2019). Image of forbush decrease in a magnetic cloud by three moments of cosmic ray distribution function. *Journal of Geophysical Research: Space Physics*, 124(1):19–31.

Potgieter, M. S. (2013). Solar modulation of cosmic rays. *Living Reviews in Solar Physics*, 10(1):3.

Raghav, A., Bhaskar, A., Lotekar, A., Vichare, G., and Yadav, V. (2014). Quantitative understanding of forbush decrease drivers based on shock-only and cme-only models using global signature of february 14, 1978 event. *Journal of Cosmology and Astroparticle Physics*, 2014(10):074.

Richardson, I. and Cane, H. (2011). Galactic cosmic ray intensity response to interplanetary coronal mass ejections/magnetic clouds in 1995–2009. *Solar Physics*, 270(2):609–627.

Richardson, I., Wibberenz, G., and Cane, H. (1996). The relationship between recurring cosmic ray depressions and corotating solar wind streams at$\leqslant$ 1 au: Imp 8 and helios 1 and 2 anticoincidence guard rate observations. *Journal of Geophysical Research: Space Physics*, 101(A6):13483–13496.

Richardson, I. G. (2004). Energetic particles and corotating interaction regions in the solar wind. *Space Science Reviews*, 111(3-4):267–376.

Richardson, J. D., Kasper, J. C., Wang, C., Belcher, J. W., and Lazarus, A. J. (2008). Cool heliosheath plasma and deceleration of the upstream solar wind at the termination shock. *Nature*, 454(7200):63.

Rilling, G., Flandrin, P., Goncalves, P., et al. (2003). On empirical mode decomposition and its algorithms. In *IEEE-EURASIP workshop on nonlinear signal and image processing*, volume 3, pages 8–11. NSIP-03, Grado (I).

Rossi, B. (1964). Cosmic rays. *McGraw-Hill*.

Shafranov, V. (1958). On magnetohydrodynamical equilibrium configurations. *Soviet Physics JETP*, 6(3):1013.

Shaul, D., Aplin, K., Araujo, H., Bingham, R., Blake, J., Branduardi-Raymont, G., Buchman, S., Fazakerley, A., Finn, L., Fletcher, L., et al. (2006). Solar and cosmic ray physics and the space environment: Studies for and with lisa. In *AIP Conference Proceedings*, volume 873, pages 172–178. AIP.

Shikaze, Y., Haino, S., Abe, K., Fuke, H., Hams, T., Kim, K.-C., Makida, Y., Matsuda, S., Mitchell, J., Moiseev, A., et al. (2007). Measurements of 0.2–20 gev/n cosmic-ray proton and helium spectra from 1997 through 2002 with the bess spectrometer. *Astroparticle Physics*, 28(1):154–167.

Simpson, J., Fonger, W., and Treiman, S. (1953). Cosmic radiation intensity-time variations and their origin. i. neutron intensity variation method and meteorological factors. *Physical Review*, 90(5):934.

Smart, D. and Shea, M. (2009). Fifty years of progress in geomagnetic cutoff rigidity determinations. *Advances in Space Research*, 44(10):1107–1123.

Sonnerup, B. Ö. and Guo, M. (1996). Magnetopause transects. *Geophysical research letters*, 23(25):3679–3682.

Sonnerup, B. Ö., Papamastorakis, I., Paschmann, G., and Lühr, H. (1987). Magnetopause properties from ampte/irm observations of the convection electric field: Method development. *Journal of Geophysical Research: Space Physics*, 92(A11):12137–12159.

Stoker, P. H. (2009). The igy and beyond: A brief history of ground-based cosmic-ray detectors. *Advances in Space Research*, 44(10):1081–1095.

Stone, E., Cummings, A., McDonald, F., Heikkila, B., Lal, N., and Webber, W. (2005). Voyager 1 explores the termination shock region and the heliosheath beyond. *Science*, 309(5743):2017–2020.

Stone, E., Cummings, A., McDonald, F., Heikkila, B., Lal, N., and Webber, W. (2013). Voyager 1 observes low-energy galactic cosmic rays in a region depleted of heliospheric ions. *Science*, 341(6142):150–153.

Stone, E. C., Frandsen, A., Mewaldt, R., Christian, E., Margolies, D., Ormes, J., and Snow, F. (1998). The advanced composition explorer. *Space Science Reviews*, 86(1-4):1–22.

Storini, M. (1990). Galactic cosmic-ray modulation and solar-terrestrial relationships. *Il Nuovo Cimento C*, 13(1):103–124.

Thakur, N., Abe, K., Fuke, H., Haino, S., Hams, T., Itazaki, A., Kim, K., Kumazawa, T., Lee, M., Makida, Y., et al. (2011). Transient variations in cosmic ray proton fluxes from bess-polar i. In *32nd International Cosmic Ray Conference, ICRC 2011*, pages 220–223. Institute of High Energy Physics.

Tsurutani, B. T., Burton, M. E., Smith, E. J., and Jones, D. E. (1987). Statistical properties of magnetic field fluctuations in the distant plasmasheet. *Planetary and space science*, 35(3):289–293.

Usoskin, I. G., Gil, A., Kovaltsov, G. A., Mishev, A. L., and Mikhailov, V. V. (2017). Heliospheric modulation of cosmic rays during the neutron monitor era: Calibration using pamela data for 2006–2010. *Journal of Geophysical Research: Space Physics*, 122(4):3875–3887.

Vitale, S. et al. (2005). Science requirements and top-level architecture definition for the lisa technology package (ltp) on board lisa pathfinder (smart-2). *ESA Ref: LTPA-UTN-ScRDIss3-Rev1*.

Walker, R. J. (1979). Quantitative modeling of planetary magnetospheric magnetic fields. *Quantitative modeling of magnetospheric processes*, 21:9–34.

Wass, P., Araújo, H., Shaul, D., and Sumner, T. (2005). Test-mass charging simulations for the lisa pathfinder mission. *Classical and Quantum Gravity*, 22(10):S311.

Webber, W. and Lockwood, J. (1988). Characteristics of the 22-year modulation of cosmic rays as seen by neutron monitors. *Journal of Geophysical Research: Space Physics*, 93(A8):8735–8740.

Wu, Z. and Huang, N. E. (2004). A study of the characteristics of white noise using the empirical mode decomposition method. *Proceedings of the Royal Society of London. Series A: Mathematical, Physical and Engineering Sciences*, 460(2046):1597–1611.